LBL--14200

DE83 003634

HYDROGEN AND DEUTERIUM NMR OF SOLIDS BY MAGIC-ANGLE SPINNING

by

Richard Raymond Eckman
(Ph.D. Thesis)

Lawrence Berkeley Laboratory
University of California
Berkeley, California 94720

This work was supported by the Assistant Secretary of Fossil Energy, Office of Coal Research, Liquefaction Division of the U.S. Department of Energy through the Pittsburgh Energy Center under contract number DE-AC03-76SF00098.

FOR NOADIAH AND NATHAN

HYDROGEN AND DEUTERIUM NMR OF SOLIDS BY MAGIC ANGLE SPINNING

Richard Raymond Eckman

ABSTRACT

The nuclear magnetic resonance of solids has long been characterized by very large spectral broadening which arises from internuclear dipole-dipole coupling or the nuclear electric quadrupole interaction. These couplings can obscure the smaller chemical shift interaction and make that information unavailable. Two important and difficult cases are that of hydrogen and deuterium. For example, the homonuclear dipolar broadening, H_D, for hydrogen is usually several tens of kilohertz. For deuterium, H_D is relatively small; however, the quadrupole interaction causes a broadening which can be hundreds of kilohertz in polycrystalline or amorphous solids. The development of cross polarization, heteronuclear radiofrequency decoupling, and coherent averaging of nuclear spin interactions has provided measurement of chemical shift tensors in solids. Recently, double quantum NMR and double quantum decoupling have led to measurement of deuterium and proton chemical shift tensors, respectively. A general problem of these experiments is the overlapping of the tensor powder pattern spectra of magnetically distinct sites which cannot be resolved. In this

work, high resolution NMR of hydrogen and deuterium in solids is demonstrated. For both nuclei, the resonances are narrowed to obtain liquid-like isotropic spectra by high frequency rotation of the sample about an axis inclined at the magic angle, β_m = $\text{Arccos}(3^{-1/2})$, with respect to the direction of the external magnetic field.

Two approaches have been developed for each nucleus. For deuterium, the powder spectra were narrowed by over three orders of magnitude by magic angle rotation with precise control of β. A second approach was the observation of deuterium double quantum transitions under magic angle rotation. For hydrogen, magic angle rotation alone could be applied to obtain the isotropic spectrum when H_D was small. This often occurs naturally when the nuclei are semi-dilute or involved in internal motion. In the general case of large H_D, isotropic spectra were obtained by dilution of ^1H with ^2H combined with magic angle rotation. The resolution obtained represents the practical limit for proton NMR of solids. Theoretical and technical aspects are described in the text with comments on the application of the principles to other nuclei of interest.

TABLE OF CONTENTS

		Page
I.	INTRODUCTION AND THEORY	1
	A. Introduction	1
	B. NMR Hamiltonian and Coherent Averaging Theory	1
	1. Nuclear Spin Hamiltonian	1
	a. External Hamiltonian	1
	b. Internal Hamiltonian	2
	c. Tensor Description and Rotations	6
	d. Relaxation Hamiltonian	13
	2. Coherent Averaging Theory	13
	a. Theory	13
	b. Rotations in Coordinate Space	16
	C. Recent Advances	20
	1. Proton-Enhanced Nuclear Induction Spectroscopy	20
	2. Magic Angle Sample Spinning	21
	3. Multiple Pulse Line Narrowing	23
	4. Double Quantum Fourier Transform NMR	23
	5. Deuterium Double Quantum Decoupling	25
	D. High Resolution NMR in Solids by Magic Angle Spinning	26
	1. High Resolution NMR	26
	2. Presence of Large Dipole-Dipole Couplings	26
	3. Presence of Quadrupole Couplings of Spins Coupled to the Observed Spins	29

Page

a. Spin 1/2 Dipolar Coupled to a Single Quadrupolar Nucleus 29

b. Dilution of Hydrogen: Appraoch to High Resolution Proton NMR of Solids 29

4. Observed Spins (S) with Electric Quadrupole Moments 31

1. Average Hamiltonian 33

2. Magic Angle Spinning 34

3. Residual Homonuclear Dipole-Dipole Coupling.. 36

4. Second Order Quadrupole Effects..... 36

5. Rotational Echoes and Removal of $H^{Q,sec}$..... 40

6. Large Quadrupole Couplings: ^{14}N..... 42

II. TECHNOLOGY 47

A. Spectrometers 47

1. Magnets 47

2. Pulse Programmer 47

3. Radio Frequency Generation 47

4. Receiving Section 48

5. Data Acquisition 48

B. Sample Probes 49

1. High Frequency Sample Turbines 49

a. Conical (Andrew) 49

b. Cylindrical 51

2. Probe Radiofrequency Circuit 59

Page

III. HIGH RESOLUTION DEUTERIUM NMR OF SOLIDS..... 62

A. Approach to High Resolution 62

B. Measurement of Quadrupole Anisotropy 65

C. Sensitivity Considerations 73

1. Strength of Irradiation Pulse 73

2. Synchronous Sampling 77

3. Sensitivity in Measurement of ω_Q 79

D. High Resolution Results 79

1. Sample Spinner Stability 79

2. Chemical and Quadrupole Shifts 85

a. Magnetic Field Dependence 85

b. Isotropic Chemical Shifts 87

3. Spectral Resolution 91

a. Contributions to the Linewidth 91

b. Results for p-dimethoxybenzene 95

c. Results for p-diethylterephthalate 99

d. Further Results 103

e. Resolution 106

E. Proton-Enhanced Deuterium NMR in Rotating Solids ... 111

1. Introduction..... 111

2. Theoretical 113

3. Experimental Results 118

4. Conclusion 126

Page

F. Double Quantum NMR with Magic Angle Spinning 128

1. Introduction 128

2. Double Quantum NMR in Rotating Solids 128

3. Results 131

G. Deuterium Spin Diffusion and Spin-Lattice Relaxation 133

1. Introduction..... 133

2. Relaxation Mechanism 134

3. Average Hamiltonian for Dipolar Coupled Spins I = 1 136

4. Experimental Results 138

IV. HIGH RESOLUTION PROTON NMR OF SOLIDS 147

A. Introduction 147

B. Partially Reduced H_{SS}^{D} for Hydrogen 147

C. Observation of Dilute Spins in Solids 154

1. Introduction 154

2. High Resolution Results 155

3. Resolution 162

4. Isotropic Chemical Shifts..... 163

5. Discussion 168

a. Comparison to High Resolution Methods 168

b. Conclusion 170

Page

APPENDICES

A. Average Hamiltonian for Quadrupole Nuclei Under Magic Angle Rotation 171

B. Magic Angle Probe Description 180

C. Pulse Programs 202

REFERENCES 208

X

Acknowledgements

It has been a great pleasure to work in the group of Professor Alex Pines. His encouragement and intuition never ceased to stimulate my thoughts and goals. I have shared and benefitted from his tremendous energy for new ideas. As a friend, I thank him for his indefatigable support.

Graduate study in Berkeley is a unique experience, both challenging and demanding. The advice and support of Professors Robert Connick and Thomas Budinger are greatly appreciated. I have been fortunate to work with outstanding postdocs and visitors whose many contributions are gratefully acknowledged; Jerry Ackerman, Madis Alla of Tallinn, Luciano Muller, and Chaohui Ye of Wuhan.

This work could not have been done without the expertise in synthetic chemistry of Sid Wolfe and I am also indebted to Herbert Zimmermann and Bob Goldberg for their work in sample preparation. The staff of the College of Chemistry has been remarkably helpful. Special credit go to Carl Gaskins for his craftsmanship, and Andy Anderson and Fred Wolf for fabricating some crazy ideas into reality. Don Wilkinson has been most generous and helpful in solving electronics problems. Special thanks go to Dione Carmichael for her care and patience in preparation of this thesis.

I deeply appreciate the many hours of discussion and assistance given me by Dave Wemmer, Steve Sinton, Dan Weitekamp, Gary Drobny, and Jim Murdoch who also brightened our days with his verse. I cannot

adequately thank them here or express my appreciation for the friendship I enjoyed with Joel Garbow, Yu-Sze Yen, Jau-Huei Tang, Warren Warren, Larry Sterna, Dave Zax, Rob Tycko, and Jean Baum. Special thanks go to John Millar for going many rounds with cantankerous spectrometers and spinners.

I would like to make special note of the encouragement and support I have received from my family. Their love has been my strength and I hope they share of my achievement.

I. INTRODUCTION AND THEORY

A. Introduction

In recent years a great deal of progress has been made in understanding the effects of pulsed radiofrequency irradiation of spin systems in matter. The cornerstone of the theoretical work in magnetic resonance which will be used to describe the experiments presented here was derived from a time dependent perturbation theory and is referred to as coherent averaging theory or average Hamiltonian theory. In this chapter the average Hamiltonian theory will be applied to the evolution of the density matrix describing the NMR spectrum of rapidly rotating solids. This provides the analysis of high resolution NMR in solids by magic angle sample rotation. To establish a perspective, a brief review of the NMR Hamiltonian and the average Hamiltonian theory is first presented. This is followed by a review of recent advances in NMR leading to measurement of the chemical shift in solids and other "high resolution" parameters.

B. NMR Hamiltonian and Coherent Averaging Theory

1. Nuclear Spin Hamiltonian

The Hamiltonian describing a collection of nuclear spins in a strong uniform external magnetic field subjected to radio frequency irradiation may be written (1,2)

$$\mathcal{H} = \mathcal{H}_{\text{external}} + \mathcal{H}_{\text{internal}} + \mathcal{H}_{\text{relaxation}} \,. \qquad \text{(I-1)}$$

a. External Hamiltonian

The Zeeman interaction of the nuclear magnetic moment with the external magnetic field is written

$$\mathcal{H}_Z = -\sum_i \gamma_i^n B_z I_{z,i} = -\sum_i \omega_{0,i} I_{z,i} \qquad \text{(I-2)}$$

where $I_{z,i}$ is the Hermitian operator for the z-component of spin angular momentum of the i^{th} spin and γ_i^n its gyromagnetic ratio in rad/(sec-Gauss). The direction of the magnetic field defines the z axis in the lab frame. The Larmor frequencies of some nuclei of interest on the spectrometers used in this work are listed in Table I.

In the high temperature approximation the reduced equilibrium density matrix is $\rho = 1 - \beta\mathcal{H}$ and the nuclear spin polarization is $\mathrm{Tr}(\rho I_z) = N\hbar_0\gamma_n^2\hbar^2 I(I+1)/3$ kT erg/Gauss where N is the number of spins.

Radio frequency irradiation gives a Zeeman type interaction

$$\mathcal{H}_{rf} = -\sum_i \gamma_i^n B_1 [I_{x,i}\cos(\omega t+\phi) + I_{y,i}\sin(\omega t+\phi)]. \qquad \text{(I-3)}$$

B_1 is typically three to five orders of magnitude smaller than B_0, but is oriented in the x-y plane and thus can be used to rotate the direction of nuclear polarization. Its effect is usually considered in an interaction representation which removes the explicit time dependence, i.e., the rotating frame defined by $H^{rot} = \exp(-i\omega I_z t)\mathcal{H}\exp(i\omega I_z t) = -(\omega_0-\omega)I_z - \omega_1 I_x$. B_0, B_1 and the phase, ϕ, are under the control of the experimenter.

b. Internal Hamiltonian

A wealth of chemical information is derived from measurement of the NMR spectrum due to the internal part of the Hamiltonian. Its main terms are the dipole-dipole couplings, nuclear electric quadrupole couplings, the chemical shift, and nuclear spin-spin couplings which are described briefly below. The relative magnitudes of these couplings vary widely among the nuclides and from sample to sample due to molecular and crystal structure.

TABLE I: Larmor frequencies of various nuclides (M Hertz)

NUCLIDE	EXTERNAL MAGNETIC FIELD 42.7 kGauss	84.7 kGauss
^{14}N	13.2	26.1
^{2}H	27.94	55.35
^{29}Si	36.2	71.6
^{27}Al	47.4	94.0
^{13}C	45.8	90.7
^{1}H	182.0	360.6

1) Dipole-Dipole Coupling

The dipole-dipole coupling between nuclear magnetic dipole moments is given by the expression

$$\mathcal{H}_D = \sum_{i<j} \hbar\gamma_i^n\gamma_j^n r_{ij}^{-3}[\underline{I}_i \cdot \underline{I}_j - 3r_{ij}^{-2}(\underline{I}_i \cdot \underline{r}_{ij})(\underline{I}_j \cdot \underline{r}_{ij})]$$

$$= \sum_{i<j} 2\hbar\gamma_i^n\gamma_j^n[\underline{I}_i \cdot \underline{\underline{D}}_{ij} \cdot \underline{I}_j] \qquad \text{(I-4)}$$

where $\underline{r}_{ij}$ is the vector between nuclei i and j, and $\underline{\underline{D}}_{ij}$ is a traceless and symmetric Cartesian tensor. It thus describes the interaction energy of each nuclear moment with a magnetic field produced by all other nuclear moments. This interaction is interesting since it depends on internuclear distances and orientations. In high magnetic field only the secular terms of $\mathcal{H}_D$ contribute to the energy in first order, which for identical spins are given by

$$H^{D,sec} = \sum_{i<j} -\hbar\gamma_n^2 r_{ij}^{-3}(\tfrac{1}{2})(3\cos^2\beta_{ij}-1)(3I_{z,i}I_{z,j} - \underline{I}_i \cdot \underline{I}_j)$$

$$= \sum_{i<j} -\hbar\gamma_n^2 r_{ij}^{-3}(\tfrac{1}{2})(3\cos^2\beta_{ij}-1)[2I_{z,i}I_{z,j} - (\tfrac{1}{2})(I_{+,i}I_{-,j} + I_{-,i}I_{+,j})] \qquad \text{(I-5)}$$

where β_{ij} is the Euler angle relating the principal axis or $\underline{\underline{D}}_{ij}$ to the lab z-axis and is identical to the polar angle, θ_{ij}, of the internuclear vector, $\underline{r}_{ij}$, in the lab frame. When the spins are unlike, $\gamma_i \neq \gamma_j$, the $I_+I_- + I_-I_+$ or flip-flop spin term in Equation I-5 is no longer secular.

2) Quadrupole Coupling

For nuclei of spin $I = 1$ or greater, the interaction of the nuclear electric quadrupole moment with internal electric field gradients at the nuclear site leads to the "quadrupole" coupling

$$\mathcal{H}_Q = \sum_i \frac{e^2(qQ)_i}{4I(2I-1)} [3I_{Z,i} - I(I+1) + (\tfrac{1}{2})\eta_i^Q(I_{+,i}^2 + I_{-,i}^2)] \qquad \text{(I-6)}$$

where e is the electronic charge, q is the "field gradient" related to local electronic structure, Q is the nuclear quadrupole moment, and η^Q is the asymmetry parameter to be defined in a later paragraph. This form is derived from the quadrupole term of the interaction energy between the nuclear and electronic charge distributions, which is due to the finite nuclear volume, and is written

$$\mathcal{H}_Q = \sum_i \underset{\sim}{I}_i \cdot \underset{\approx}{V}_i \cdot \underset{\sim}{I}_i \ . \qquad \text{(I-7)}$$

In bulk matter there is generally zero electronic orbital angular momentum and $\underset{\approx}{V}$ is a traceless Cartesian tensor which is the expectation value of its corresponding electron operators over the electronic wavefunction. Equation I-7 is written in the principal axis frame of $\underset{\approx}{V}$. Since the external nuclear spin Hamiltonian is conveniently described in the laboratory frame defined by B_z, a rotation of operators in $\mathcal{H}_Q$ is performed to describe $\mathcal{H}_Q$ in the lab frame. Taking $\eta = 0$ for simplicity then $I_Z = I_z\cos\beta + I_x\sin\beta$ and the result is

$$\mathcal{H}_Q = \sum_i \frac{e^2(qQ)_i}{4I(2I-1)} \left\{ \begin{array}{l} (1/2)(3\cos^2\beta - 1)[3I_{z,i}^2 - I(I+1)] \\ +(3/2)\sin\beta\cos\beta[I_{z,i}(I_{+,i} + I_{-,i}) + (I_{+,i} + I_{-,i})I_{z,i}] \\ +(3/4)\sin^2\beta(I_{+,i}^2 + I_{-,i}^2) \end{array} \right\} \qquad \text{(I-8)}$$

where the first term in large brackets is the secular term. Transformation properties of the tensor operators under rotation is reviewed below. $\mathcal{H}_Q$ contains spin operators of only the i^{th} nuclear spin.

3) Chemical Shift

The chemical shift arises from small magnetic fields at the nuclear site due to induced diamagnetism and paramagnetism of the surrounding electrons. It provides the chemist with a powerful tool for determination of molecular structure and is written

$$\mathcal{H}_\sigma = \sum_i \hbar\gamma_i^n [\underset{\sim}{I}_i \cdot \underset{\approx}{\sigma}_i \cdot \underset{\sim}{B}]. \tag{I-9}$$

The secular term is

$$H^{\sigma,sec} = \sum_i \omega_{0,i} I_{z,i} \sigma_{zz,i} \tag{I-10}$$

and again this Hamiltonian contains spin operators of only the i^{th} spin.

4) Spin-Spin Coupling

The indirect nuclear spin-spin or "J" coupling adds detailed fine structure to the NMR spectrum and is written

$$\mathcal{H}_J = \sum_{i<j} \underset{\sim}{I}_i \cdot \underset{\approx}{J}_{ij} \cdot \underset{\sim}{I}_j \ . \tag{I-11}$$

For like spins i,j with large differences in their chemical shifts or for unlike spins i,j the truncated secular J coupling is

$$H^{J,sec} = \sum_{i<j} J_{ij} I_{z,i} I_{z,j}. \tag{I-12}$$

c. Tensor Description and Rotations

The terms of the internal Hamiltonian written above in Cartesian tensor formalism all have the common form (3)

$$\mathcal{H} = C \sum_{a,b=1}^{3} R_{ab} T_{ba} \ . \tag{I-13}$$

T contains dyadic products of the coupled vectors, either two nuclear spin vectors or one spin vector and a vector magnetic field. The R are rank two tensors derived from the nature of the coupling. The spectroscopically observable terms of R are its isotropic and traceless symmetric components; $R^{(0)} = 1/3\ \mathrm{Tr}(\underset{\approx}{R})$ and $R^{(2)}$ respectively. In its principal axis frame (PAS), which is in general fixed in the molecule or crystal, R is diagonal with principal elements R_{xx}, R_{yy}, R_{zz} defined such that $|R_{zz} - R^{(0)}| \geq |R_{xx} - R^{(0)}| \geq |R_{yy} - R^{(0)}|$. The latter are the principal elements of $R^{(2)}$. It is convenient to define the anisotropy parameter, $\delta = R_{zz} - R^{(0)}$, and asymmetry parameter, $\eta = (R_{yy} - R_{xx})/\delta$, which gives in the PAS

$$\underset{\approx}{R} = R^{(0)}\underset{\approx}{1} + \delta\begin{pmatrix} -\frac{1}{2}(1-\eta) & 0 & 0 \\ 0 & -\frac{1}{2}(1+\eta) & 0 \\ 0 & 0 & 1 \end{pmatrix}. \qquad \text{(I-14)}$$

The asymmetry is $1 \geq \eta \geq 0$ and when the tensor has axial symmetry, $\eta = 0$, then $R_{zz} = R_{\parallel}$ and $R_{xx} = R_{yy} = R_{\perp}$.

In studying the behavior of the spin system under rotation, it is convenient to write the internal Hamiltonian in irreducible spherical tensor form and Equation I-13 becomes

$$\mathcal{H} = C \sum_{\ell} \sum_{m=-\ell}^{\ell} (-1)^m R_{\ell,-m} T_{\ell,m} \qquad \text{(I-15)}$$

The couplings R are then readily transformed from PAS to LAB by use of the Wigner rotation matrices with the expression

$$R^{(\mathrm{LAB})}_{\ell,m} = \sum_{m'} D^{\ell}_{m',m}(\alpha,\beta,\gamma) R^{(\mathrm{PAS})}_{\ell,m'} \qquad \text{(I-16)}$$

where α, β, γ are the Euler angles. The connection between the $R_{\ell,m}$ and the R_{ab} above the PAS is

$$R_{0,0} = R^{(0)}$$

$$R_{2,0} = (3/2)^{\frac{1}{2}}\delta$$

$$R_{2,2} = -(1/2)\eta\delta \qquad \text{(I-17)}$$

Since the R_{ab} are symmetric and second rank, then ℓ in Equation I-16 is restricted to $\ell = 0,2$ and for $R_{\ell,m}$(PAS) the non-vanishing elements have $m = 0, \pm 2$.

The products T in Equation I-13 may be written once and for all in the irreducible spherical basis set of their rotation group, O(3), and the set is denoted $T_{\ell,m}$. For instance, $T_{2,0}(\mathcal{H}_Q) = 6^{-\frac{1}{2}}(3I_0^2 - I \cdot I)$, where the spin operators are defined

$$I_{\pm} = I_x \pm iI_y$$

$$I_0 = I_z$$

$$I_{\pm 1} = \mp 2^{-\frac{1}{2}}I_{\pm} \qquad \text{(I-18)}$$

The standard basis set $T_{\ell,m}$ and the useful Wigner rotation matrix D^2 are given concisely in Reference 3. The use of irreducible tensor methods is described in many texts (4,5).

By substitution of the appropriate trigonometric expressions, Equations I-5, I-6, and I-10 become

$$H_{LAB}^{D,sec} = \sum_{i<j} -(\tfrac{1}{2})\gamma_n^2\hbar r_{ij}^{-3}(3\cos^2\beta_{ij}-1)(3I_{o,i}I_{o,j} - I_i \cdot I_j) \qquad \text{(I-19)}$$

$$H_{LAB}^{Q,sec} = \sum_i \frac{e^2(qQ)_i}{4I(2I-1)} [(\tfrac{1}{2})(3\cos^2\beta_Q - 1) + (\tfrac{1}{2})\eta_i^Q \sin^2\beta_Q \cos 2\gamma_Q](3I_{o,i}^2 - I_i^2) \qquad \text{(I-20)}$$

$$H_{LAB}^{\sigma,sec} = \sum_i \omega_{o,i}\{\sigma_i + (\tfrac{1}{2})\delta_i^\sigma[(3\cos^2\beta_\sigma - 1) + \eta_i^\sigma \sin^2\beta_\sigma \cos 2\gamma_\sigma]\}I_{o,i} \qquad \text{(I-21)}$$

where σ_i is the isotropic chemical shift normally observed in fluids. Since $[H_{ij}^{D,sec}, H_{ik}^{D,sec}] \neq 0$ the dipolar coupling for more than a few spins results in a homogeneous resonance with a shape close to Gaussian and no singular features. In this case the moments of the resonance may be measured and related to $H^{D,sec}$ by the Van Vleck method of moments (1). In a powder or amorphous sample all orientations $(\alpha,\beta,\gamma)_i$ are equally probable and a continuous distribution or inhomogeneous "powder pattern" of the resonance is observed for $H^{Q,sec}$ and $H^{\sigma,sec}$. The resonance lineshape for $H^{\sigma,sec}$ is illustrated in Figure 1. Figure 1a depicts the lineshape for axial symmetry and Figure 1b shows the case $\eta \neq 0$. For a quadrupolar nucleus I = 1 in high magnetic field the lineshape, $I(\omega)$, due to $H^{Q,sec}$ for $\eta = 0$ is shown in Figure 2. It is composed of overlapping right and left handed patterns as shown in Figure 1a which are due to the two single quantum ($\Delta m = 1$) transitions in the three level system ($I = 1$, $m = -1,0,+1$). The angle $\theta(=\beta_Q$ in Eq. I-20) is the polar angle of the principal axis, V_{zz}, of the coupling tensor $\underset{\approx}{V}$ in LAB.

In writing Hamiltonians hereafter, the summation over all spins will be dropped for convenience unless specifically needed. It is also convenient to define parameters which are related to the magnitude or "strength' of a given term of the Hamiltonian. These are illustrated in Table II.

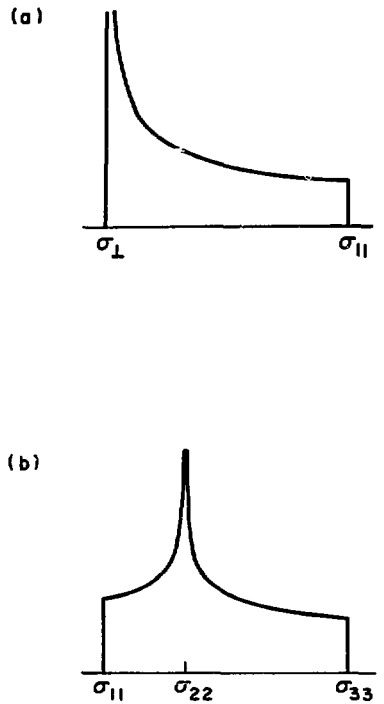

XBL 763-713

Figure 1

Powder pattern lineshapes for anisotropic NMR chemical shifts in high magnetic field. (a) Lineshape for axially symmetric chemical shift tensor. (b) Lineshape for asymmetric tensor.

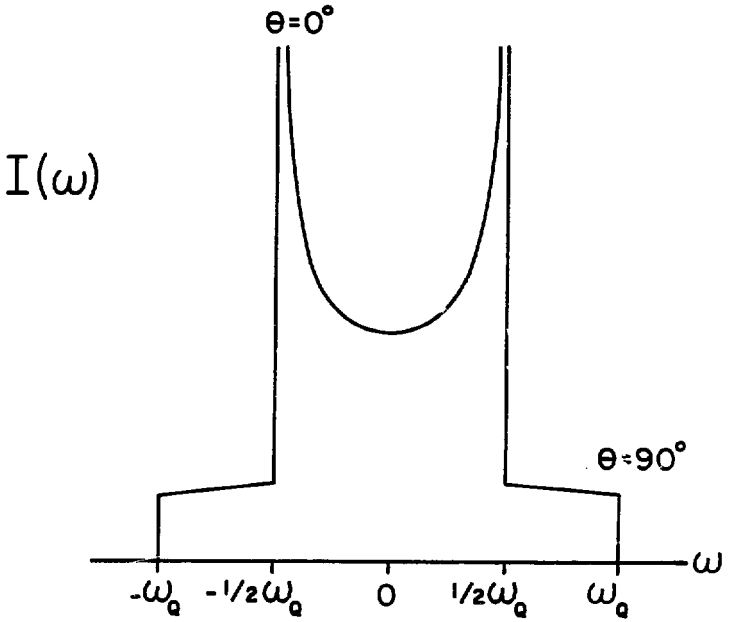

XBL 8111-12667

Figure 2

Theoretical powder pattern lineshape, $I(\omega)$, for axially symmetric spin I = 1 quadrupole interaction in high magnetic field. The quadrupole coupling is $\omega_Q = (3/4)e^2qQ$ and θ is the angle between the principle axis of the quadrupole tensor and the direction of the external magnetic field.

TABLE II: Magnitudes of terms in nuclear spin Hamiltonian in high magnetic field

Magnitude	Definition	Name
ω_0	$\gamma_n B_0$	Larmor frequency
ω_1	$\frac{1}{2}\gamma_n B_1$	strength of r.f. irradiation
$(\Delta\omega^2)_D^{1/2}$	$\propto M_2^{1/2}$ (second moment)*	full width at half maximum of dipolar broadened resonance
ω_D	$-\frac{1}{2}\gamma_n^2 h r_{ij}^{-3}(3\cos^2\beta_{ij} - 1)$	dipolar coupling for spin pair i,j
Ω_Q	$\frac{3e^2qQ}{4I(2I-1)}\ \frac{1}{2}(3\cos^2\beta_Q - 1)$ $+ \frac{1}{2}\eta_Q \sin^2\beta_Q \cos 2\gamma_Q$	quadrupole coupling
ω_Q	$3e^2qQ/4I(2I-1)$	quadrupole coupling

*Precise definition depends on lineshape function, usually Gaussian (see Ref. 1).

d. Relaxation Hamiltonian

Interactions of the nuclear spins which cause spin lattice relaxation are grouped into $\mathcal{H}_R$. In the typical case, e.g., an organic molecular solid where there are no unpaired electrons, the internal Hamiltonian has a time dependence due to relative motion of the nuclei in the solid and can be rewritten as $H = H_0 + H_1(t)$ where H_0 contains the terms which remain time dependent. $H_1(t)$ couples the spin system to the lattice and causes the return to thermal equilibrium. Spin diffusion, a mutual flip-flop transition of spin pairs induced by the $I_+^i I_-^j + I_-^i I_+^j$ term of the dipole coupling, tends to maintain a uniform spin temperature in the system in its approach to equilibrium. When the system can be divided into subsystems of spins with non-equidistant energy level spacings, e.g., spins with different γ_n or spins with identical γ_n and largely different quadrupole couplings, the flip-flop transition may be quenched since it is not energy conserving. Cross relaxation may be induced between subsystems when the energy spacing may be controlled by the experimenter to produce a level crossing (6). A particular case of quadrupolar deuterium ($I = 1$) nuclei is considered in Chapter III.

2. Coherent Averaging Theory

a. Theory

The advent of magic angle sample spinning and the use of multiple rf pulse sequences in NMR has led to a variety of new experiments in recent years designed to remove the effect of certain terms of the internal Hamiltonian while preserving others. In these experiments a time dependence is introduced into $\mathcal{H}_{internal}$ and a time averaged

$\bar{\mathcal{H}}_{internal}$ is observed. Development of new methods has been guided by the coherent averaging theory which is briefly reviewed here (3).

The total Hamiltonian of the spin system is subdivided into an explicitly time dependent part and an internal part

$$\mathcal{H} = \mathcal{H}_1(t) + \mathcal{H}_{int}. \tag{I-22}$$

In a classical sense, the effect of $\mathcal{H}_1(t)$ is to cause a precession of the nuclear magnetizations about the direction of $\mathcal{H}_1(t)$. The internal Hamiltonian is usually the chemically interesting term and contains the terms of the internal Hamiltonian described in the previous section. Transforming to an interaction representation, the periodicity of $\mathcal{H}_1(t)$ is transferred to $\mathcal{H}_{int}$

$$\mathcal{H}_{int}(t) = U_1^{-1}(t)\, \mathcal{H}_{int} U_1(t) \tag{I-23}$$

where

$$U_1(t) = T \exp[-i \int_0^t \mathcal{H}_1(t')dt'] \tag{I-24}$$

and T is the Dyson time-ordering operator. The time evolution of the spin density matrix is found by solution of the equation of motion, $d\rho/dt = -i[\mathcal{H},\rho]$ and the result is given by

$$\rho(t) = U(t)\, \rho(t=0) U^{-1}(t) \tag{I-25}$$

where $U(t) = U_1(t)U_{int}(t)$ and

$$U_{int}(t) = T \exp[-i \int_0^t \mathcal{H}_{int}(t')dt'] \tag{I-26}$$

When the time dependence caused by $\mathcal{H}_1(t)$ is cyclic then $\mathcal{H}_1(t+\tau) = \mathcal{H}_1(t)$ and $U_1(t+t_c) = U_1(t)$, where t_c is the cycle time and τ may be finite or infinitely short. Under these conditions the evolution of $\rho(t)$ may be observed at multiples of t_c where $U_1(Nt_c) = 1$ and $U_{int}(Nt_c) = [U_{int}(t_c)]^N$. Thus the time average of $\mathcal{H}_{int}(t)$ over one cycle may be used to describe the long time evolution of $\rho(t)$. Since there may be many time dependences in Equation I-26, the Magnus expansion has been used to express $U_{int}(t_c)$ more conveniently according to

$$U_{int}(t_c) = T \exp[-i \int_0^t \mathcal{H}_{int}(t')dt']$$

$$= \exp[-i(\bar{\mathcal{H}}^0 + \bar{\mathcal{H}}^1 + \bar{\mathcal{H}}^2 + \ldots)t_c] \qquad \text{(I-27)}$$

where

$$\bar{\mathcal{H}}^0 = (1/t_c) \int_0^{t_c} \mathcal{H}_{int}(t)dt$$

$$\bar{\mathcal{H}}^1 = (-i/2t_c) \int_0^{t_c} dt_2 \int_0^{t_2} dt_1 [\mathcal{H}_{int}(t_2), \mathcal{H}_{int}(t_1)]$$

$$\bar{\mathcal{H}}^2 = (-1/6t_c) \int_0^{t_c} dt_3 \int_0^{t_3} dt_2 \int_0^{t_2} dt_1$$

$$\{[\mathcal{H}_{int}(t_3), [\mathcal{H}_{int}(t_2), \mathcal{H}_{int}(t_1)]]$$

$$+ [\mathcal{H}_{int}(t_1), [\mathcal{H}_{int}(t_2), \mathcal{H}_{int}(t_3)]]\}. \qquad \text{(I-28)}$$

Notable features of the average Hamiltonian $\bar{\mathcal{H}} = \bar{\mathcal{H}}^0 + \bar{\mathcal{H}}^1 + \bar{\mathcal{H}}^2 + \ldots$ are that it is now time independent and that the series may be truncated at any term to leave an Hermitian operator.

The well-known "truncation" of NMR Hamiltonians in high magnetic field due to time independent perturbation theory is readily described

in the coherent averaging formalism. The time dependence is due to the Zeeman coupling to the field, $\mathcal{H}_1(t) = -\omega_0 I_z$ and $U_1(t) = \exp(i\omega_0 I_z t)$, wherein $t_c = 2\pi/\omega_0$. Thus terms which do not commute with I_z average to zero in $\bar{\mathcal{H}}^0$; they are "truncated". In general, $\bar{\mathcal{H}}^0$ corresponds to the first order time independent result (wherein $\mathcal{H}_{int}$ perturbs $\mathcal{H}_1$ and the latter determines the t_c) and when $\lambda \sim \|\mathcal{H}_{int}\|/\|\mathcal{H}_1\|$ is small (where double lines indicate magnitude) then $\bar{\mathcal{H}}^{n+1} << \bar{\mathcal{H}}^n$ and the $\bar{\mathcal{H}}^1$ approximates the second order time independent result. The general criterion for rapid convergence of the expansion is that $t_c\|\mathcal{H}_{int}\| << 1$; thus in the case of sample rotation ω_r must exceed the breadth in frequency of the homogeneous part of the resonance linewidth.

Since the total Hamiltonian is the sum of terms which do not all commute with each other, one can define multiple time dependences, $\mathcal{H}_1(t)$, and calculate averages over averages, $\bar{\bar{\mathcal{H}}}$. This is a typical case when $\|\mathcal{H}_Q\| >> \|\mathcal{H}_D\|$ or a particular part of $\mathcal{H}_D$, e.g., the coupling between spins i and j, is much larger than the coupling between all other spins $i \neq j$. It also occurs when the sample is rotated which introduces a time dependence in the spatial variables of $\mathcal{H}_{int}$. When the cycle times of the various interactions are very different, the theory reviewed above may be applied repeatedly, beginning with the interaction for which t_c is the smallest.

b. *Rotations in Coordinate Space*

In NMR studies of solids the spatial variables of the Hamiltonian, i.e., the $(\alpha,\beta,\gamma)_i$, are often time-dependent due to molecular motions or rotation of the sample. In this case coherent averaging theory may be applied and since the explicit time dependence is in $\mathcal{H}_{int}$ no further interaction representation is necessary. It is useful at this

point to consider the example of rotation of the sample about a single axis or a molecular motion in the solid which is viewed as a continuous rotation about a single axis.

Using spherical tensor form, Equation I-16 may be applied twice to transform the coupling tensor $R_{\ell,m}(D,V,\sigma,J)$ from PAS to a reference frame fixed in the rotor (sample rotor or molecular rotor), which is usually labeled CRS, and then from CRS to LAB. The general result for the second rank ($\ell = 2$) terms is

$$R_{2,0}^{(LAB)} = \sum_{m'} D^{2}_{m',0}(\alpha'',\beta'',\gamma'') \sum_{m''} D^{2}_{m'',m'}(\alpha',\beta',\gamma')R_{2,m''}^{(PAS)} \qquad (I-29)$$

where $m'' = 0, \pm 2$ (see Eq. I-16 and discussion) and $m = 0$ when only secular terms are included. The Euler angle set (α',β',γ') is constant for each particular nucleus i or pair i,j and brings $R_{\ell,m}$ into CRS. The transformation to LAB is illustrated in Figure 3. CRS is chosen fixed in the rotor with its z axis parallel to the rotor axis. For example, in the top of Figure 3 is shown the orientation of the principal axis of an axially symmetric ($\eta = 0$) coupling tensor, $R_{\|}$, in the rotor fixed frame. The Euler angles, β',α' are equivalent to the polar angles θ,ϕ respectively of $R_{\|}$. The transformation from CRS to LAB is made by the Euler rotation $(\alpha'',\beta'',\gamma'')$ which is illustrated in the middle and bottom of Figure 3. Rotation by γ'' about the z axis of CRS brings the coupling into an intermediate tilted LAB frame and since this z axis is the axis of the rotor, $\gamma'' = \omega_r t$. Rotation by β'' about x'(tilted LAB) = X(LAB) brings the coupling tensor into the LAB frame. The Euler angle α'' represents a rotation about the Z LAB axis under which the NMR Hamiltonian is invariant, thus $\alpha'' = 0$. In summary, the Euler set which brings CRS to LAB is $(0,\beta'',\omega_r t)$ and is time-dependent due to the sample or molecular rotation.

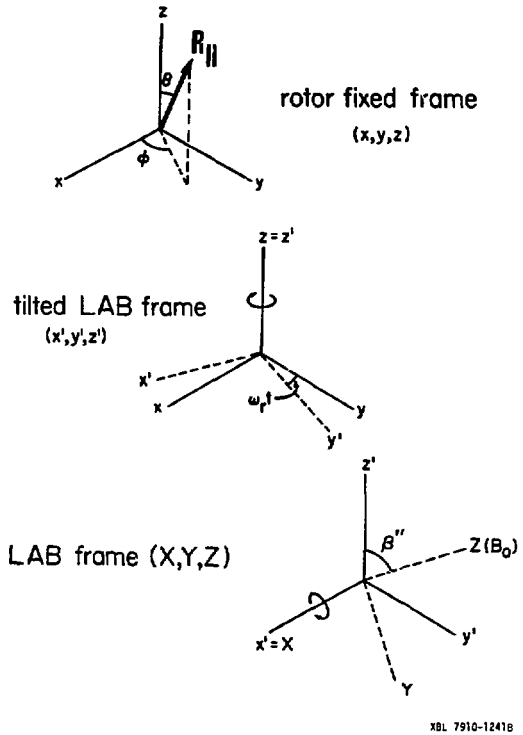

Figure 3

Euler angles for the transformation of nuclear interaction tensors from the molecular or crystal frame of reference in a rotating sample to the laboratory frame defined by the external magnetic field. $R_{\parallel}$ is the principle axis of an axially symmetric tensor coupling and ω_r is the frequency of sample rotation.

An important point of the coherent averaging theory as expressed in Equation I-28 is that when $\mathcal{H}_{int}$ commutes with itself at all times all the higher order terms $\bar{\mathcal{H}}^1 + \bar{\mathcal{H}}^2 + \ldots$ vanish identically. When this is the case, $\mathcal{H}_{int}$ is termed inhomogeneous. $H^{Q,sec}$ and $H^{\sigma,sec}$ are inhomogeneous. However, since in Equation I-20 $[I_{\underline{0}},I_{\underline{1}}] \neq 0$, the dipolar coupling between pairs i,j and i,k do not commute at all times and the dipolar coupling is in general homogeneous. The ramifications of this fact will be discussed in the next section. In the present case it is assumed that the sample or molecular rotation is much faster in frequency than the magnitude of $\mathcal{H}_{int}$ in frequency, $\omega_r >> (\Delta\omega^2)^{\frac{1}{2}}_{int}$.

In calculating the average Hamiltonian for the rotation, all terms of $D^2_{m',0}$ in Equation I-29 with $m' \neq 0$ contain the angular factor $\exp(im'\gamma'') = \exp(im'\omega_r t)$. Since $\int_0^{2\pi/\omega_r} \exp(in\omega_r t)dt = 0$, only the term with $m' = 0$ survives. Thus $R^{(LAB)}_{2,0}$ is proportional to $D^2_{0,0}(\beta'') = \frac{1}{2}(3\cos^2\beta'' - 1)$. By insertion of the trigonometric functions and using the definitions of Equation I-17, Equation I-29 becomes

$$R^{(LAB)}_{2,0} = \tfrac{1}{2}(3\cos^2\beta''-1)(3/2)^{\frac{1}{2}}\delta\{\tfrac{1}{2}(3\cos^2\beta'-1) - (\tfrac{1}{2})\eta\sin^2\beta'\cos2\gamma'\}. \qquad \text{(I-30)}$$

Since the quadrupole and dipole-dipole coupling, V and D, are traceless the $R_{0,0}(\ell = 0)$ terms which remain in the average Hamiltonian are σ and J, the isotropic chemical shift and spin-spin couplings.

In the case of uniaxial molecular rotation, CRS is fixed in the molecular rotor and the Euler set (α',β',γ') has a fixed value for the nuclei in the rotor. Thus the factor in curly brackets in Equation I-30 is a number. For a powder sample there exists an isotropic distribution of

angles β'' and Equation I-30 thus describes an axially symmetric powder pattern as depicted in Figure 1a. Thus even if $\eta \neq 0$, the molecular rotation eliminates the asymmetry.

For the case of sample rotation, CRS is fixed in the sample rotor and for a powder there exists an isotropic distribution of Euler angles (α',β',γ'). The angle between the axis of the sample rotor and the direction of B_0, β'', is adjusted by the experimenter. When the spinner axis is adjusted to the "magic" setting, $\beta'' = \text{Arccos}(3^{-\frac{1}{2}}) = 54.7° = \frac{1}{2}(109.5°) = \beta_m$(magic angle or MA) and $D^2_{0,0}$ vanishes. Thus the second rank terms of all the secular interactions of $\mathcal{H}_{int}$ vanish in the zeroth order average Hamiltonian even for an isotropic distribution of (α',β',γ'). A useful fact, as pointed out by Pines and discussed by Stejskal et al. (7), is that an offset from the magic angle represents a scaling of the anisotropic lineshape by $D^2_{0,0} \neq 0$. Comparing Equation I-30 to Equations I-20 and I-21 it is clear that sample rotation preserves and scales the original anisotropic/asymmetric coupling.

C. Recent Advances

In this section a brief overview of recent advances in NMR which lead to the measurement of the chemical shift in solids is presented.

1. Proton-Enhanced Nuclear Induction Spectroscopy

In solids the chemical shift is usually completely obscured by a larger homonuclear dipole-dipole coupling, H^D_{SS}. Broad Gaussian lineshapes usually result from which little can be gained. While the homonuclear dipole coupling, can be reduced or removed by isotopic dilution of the observed spins, S, the resulting loss of sensitivity is

a problem. These two basic difficulties were solved by the introduction of Proton-Enhanced Nuclear Induction Spectroscopy (8). Here, the observation of dilute spins, S, in a sample with abundant spins, I, which are usually protons has made measurement of chemical shift tensors of the S spins in solids available. H_{SS}^{D} is removed by dilution, which for the case of ^{13}C is natural since they are only 1% abundant. Sensitivity is enhanced by transferring polarization from I to S by a Hartmann-Hahn matching of their Zeeman energies in the rotating frame. The polarization in the S spins can be enhanced by γ_n^I/γ_n^S, which is four for $^{13}C - {}^1H$ and 6.5 for $^2H - {}^1H$. The S system is "cross polarized" from the I system via energy conserving flip-flop transitions induced by their heteronuclear dipole-dipole coupling, H_{IS}^{D}. Thus the S system may be repolarized after T_1 of the I system, which leads to a large savings in time when $T_1^I << T_1^S$.

2. Magic Angle Sample Spinning

In high field NMR, the secular terms of the internal Hamiltonian are described by a second rank tensor which is proportional to $P_2(\cos\beta) = \frac{1}{2}(3\cos^2\beta-1)$ where β is the angle between the principal axis of the tensor in PAS to the Z direction of the external magnetic field. This fact was exploited early in the development of NMR when it was noticed that the isotropic average of the internal Hamiltonian would be observed when $\beta = \beta_m$ where $P_2(\cos\beta)$ vanishes. Since $H^{D,sec}$, $H^{Q,sec}$ are traceless and the trace of $H^{\sigma,sec}$, $H^{J,sec}$ are the isotropic values observed in a fluid, the broadening of spectra of solids could be removed by rotation of the sample about the magic angle. When the fast spinning criterion is not met for an homogeneous interaction, e.g., for $H^{D,sec}$, the correction terms $\bar{\mathcal{H}}^1 + \bar{\mathcal{H}}^2 + \ldots$ in Equation I-28 are substantial and

only a slight to partial narrowing is observed. Thus the drawback appeared to be that in order to observe the isotropic couplings, one would have to rotate the sample faster in frequency than the magnitude of the broadening, $\omega_r > (\Delta\omega^2)_D^{\frac{1}{2}}$, which is clearly impossible in the general case.

Andrew et al. (9) and Lowe (10) first developed high speed turbines to rotate solid samples at speeds of several kiloHertz and observed that dipolar broadened lines can be substantially narrowed in cases where $\mathcal{H}_D$ is small. Chemical shifts and scalar coupled multiplets were observed and the second moment of the resonance was shown to be conserved under magic angle spinning.

Recently it was found that sample rotation has a dramatic effect on an inhomogeneously broadened resonance, even when the frequency of rotation, ω_r, is much less than the inhomogeneous linewidth. Stejskal et al. (7), and Lippmaa et al. (11) demonstrated that ω_r must only exceed the homogeneous width, δ_0, of the spin packets which comprise the inhomogeneous resonance and that sharp sideband spectra are obtained with "slow" spinning. When the broadening is largely inhomogeneous, the correction terms in Equation I-28 are small and $\bar{\mathcal{H}}^0$ suffices to describe the evolution of the spin system at multiples of the spinner cycle. An elegant treatment of NMR in rotating solids has been given by Maricq and Waugh (12). Thus when H_{SS}^D of the observed S spins is small, the inhomogeneous broadening due to the chemical shift anisotropy may easily be removed. This is the natural case for ^{13}C, ^{31}P in solids and Proton-Enhanced magic angle spinning ^{13}C NMR has quickly become the chemist's standard tool. Isotropic chemical shifts have also been measured by Lippmaa et al. (13) for a

variety of NMR nuclei for which H_{SS}^{D} is naturally small including ^{29}Si, ^{119}Sn.

3. Multiple Pulse Line Narrowing

The combination of the application of many rf pulses with suitable time delays to build cyclic propagators, U, for the spin density matrix has produced the ability to remove the homogeneous dipolar broadening of NMR spectra of solids (3). This technique, labeled multiple pulse line narrowing, has further been combined with magic angle sample spinning in order to obtain isotropic liquid-like spectra even of protons where the dipolar broadening can be 50-100 kHz (14,15). Recent advances have included pulse sequences to eliminate higher order correction terms in $\bar{\mathcal{H}}$ and reduce the effects of imperfect and weak rf pulses (16).

4. Double Quantum Fourier Transform NMR

The "forbidden" double quantum ($\Delta m = 2$) transitions in the three level system of a nucleus with $I = 1$ can be induced with a weak rf irradiation, $\omega_1 < \omega_Q$. Vega and Pines (17) have developed a fictitious spin ½ operator formalism to describe the preparation and detection of multiple quantum coherence, i.e., the coherent superposition of the nuclear spin eigenstates represented by off-diagonal elements of the spin density matrix. Observation of deuterium double quantum transitions was developed for pulsed Fourier transform NMR with heteronuclear double resonance decoupling (18-21). Since the high field, secular quadrupole coupling, is proportional to $\langle I_z^2 - \frac{1}{3} I^2 \rangle = m^2 - \frac{1}{3} I(I-1)$, the $\pm m$ nuclear eigenstates are shifted equally as shown in Figure 4. The deuterium double quantum transition with $\Delta m = 2$ for spin 1, remains unaffected

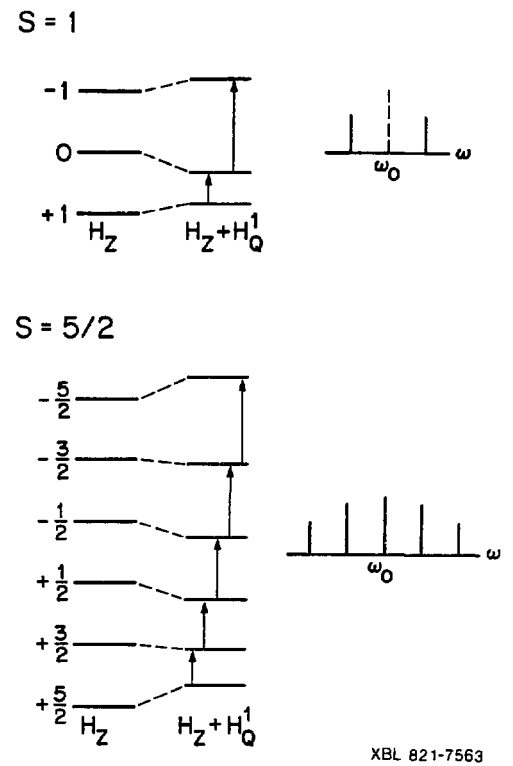

Figure 4

Energy level diagram showing transitions with $\Delta m = 1$ for nuclei with $S = 1, 5/2$ in high magnetic field. H_Q^1 is the first order perturbation theory correction to the Zeeman energy, H_Z, and ω_0 is the Larmor frequency.

by $H^{Q,sec}$. Observation of the double quantum spectrum of deuterium in solids effectively removes the large broadening due to $H^{Q,sec}$ allowing the much smaller chemical shift tensor to be measured and providing a novel approach to high resolution NMR in solids.

5. Deuterium Double Quantum Decoupling

An additional approach to high resolution proton NMR in solids, developed by Pines, Vega, and Mehring (22), is the observation of spectra of isotopically dilute protons, S, in a deuterated solid. Dilution of the protons reduces their homonuclear dipole coupling, H^D_{SS}, to a very small value. Rf decoupling is then used to remove the broadening of the proton spectrum due to the heteronuclear dipole coupling, H^D_{IS}, with the surrounding deuterons, I. The homonuclear dipole coupling of the deuterons, H^D_{II}, is small and can be neglected.

For rf decoupling of spins ½, the heteronuclear spins, I, are irradiated near their Larmor frequency with an effective decoupling field $\omega_e = (\Delta\omega^2 + \omega_{1I}^2)^{\frac{1}{2}}$ where $\Delta\omega = \omega_{0I} - \omega$ and $\theta = \text{Arctan}(\omega_{1I}/\Delta\omega)$ is the angle between the direction of the effective field and the LAB Z axis (23). Decoupling requires approximately that $\omega_{1I} > \Delta\omega, \omega^D_{IS}$, i.e., the decoupling strength must "cover" the larger of the resonance offset or dipolar broadening. To observe the dilute protons, the dipolar coupling to spin 1 deuterium must be decoupled. The quadrupolar broadened resonance of the deuterons, shown in Figure 2, may be as large as 260 kHz or more in breadth. The unavoidable large offsets would appear to make decoupling extremely difficult when usually ω_{1I} may be a few tens of kiloHertz. However, by inducing rapid double quantum transitions of the deuterons, efficient decoupling was achieved with substantially reduced rf field strength requirements. Using the fictitious spin ½ formalism, it can be

shown that in the fictitious double quantum frame the effective decoupling field is $\omega_e = [(2\Delta\omega)^2 + \omega_{1I}^4/\Omega_Q^2]^{\frac{1}{2}}$ with $\theta = \text{Arctan}(\omega_{1I}^2/2\Delta\omega\Omega_Q)$ in analogy with the single quantum case described above. The important point is that $\Delta\omega = \omega_{OI} - \omega$ *does not depend on* Ω_Q and can be made small so that the reduced requirements for decoupling are $\omega_{1I}^2 > 2\Delta\omega\Omega_Q, \omega_{IS}^D\Omega_Q$ which are easily satisfied with current technology. Thus the complete high field proton chemical shift tensor could be measured in the solid.

D. High Resolution NMR in Solids by Magic Angle Spinning

1. High Resolution NMR

The basic goal of the experiments to be described here is the removal of linebroadening in solids due to dipole-dipole couplings and anisotropic terms of the internal Hamiltonian. When this is done the isotropic chemical shift may be observed and liquid-like spectra obtained. At the same time, it is desirable to retrieve the values of the anisotropies whenever possible, since they provide additional information about chemical and physical structure. One of the most important chemical nuclei is that of hydrogen and the bulk of the work described here is the use of magic angle spinning to observe high resolution spectra of hydrogen and deuterium in solids. In this section, the coherent averaging theory is applied to the case of sample rotation. The NMR Hamiltonian was reviewed in Chapter IB and in the following paragraphs several cases with various magnitudes of $\mathcal{H}_D$, $\mathcal{H}_\sigma$, and $\mathcal{H}_Q$ are considered.

2. Presence of Large Dipole-Dipole Couplings

When the homonuclear dipole-dipole coupling dominates the internal Hamiltonian of the observed spins, i.e., when $(\Delta\omega^2)_D^{\frac{1}{2}}$ is much greater than the spread of chemical shifts, and $\mathcal{H}_Q = 0$ then broad,

featureless resonances are usually the rule. This is the typical case for hydrogen in solids where Gaussian lines of 50–100 kHz breadth are often observed. When the sample is rotated, $\mathcal{H}_D$ is rendered time dependent. Since the time dependence induced in the internal Hamiltonian by the Zeeman coupling is many orders of magnitude larger, $\omega_0 >> \omega_r$, we may first average over the faster time scale (truncation to secular terms) and then average over the sample rotation. As noted previously, $\mathcal{H}_D$ is removed by magic angle rotation in general only for fast spinning and isotropic spectra obtained only when $(\Delta\omega^2)_D^{\frac{1}{2}}$ is less than attainable spinning frequencies which are some several kiloHertz.

In many instances, e.g., spins with low γ_n and solids in which there is rapid molecular reorientation, the broadening $(\Delta\omega^2)_D^{\frac{1}{2}}$ happens to be small enough to be effectively spun away. On the other hand it is often necessary to dilute the observed spins to reduce $(\Delta\omega^2)_D^{\frac{1}{2}}$. This may occur naturally if the spins are relatively far apart in their bonding arrangement or if the observed nuclide has a low natural abundance. In the case of hydrogen, dilution by isotopic substitution with deuterium is usually necessary.

In most cases there will be a substantial heteronuclear dipole-dipole coupling, $H_{IS}^{D,sec}$, of the observed spins, S, with the unlike spin system, I. There is typically a large difference in the Larmor frequencies ω_{0I} and ω_{0S} and the flip-flop term $(S_+I_- + S_-I_+)$ of Equation I-5 is no longer secular. $H_{IS}^{D,sec}$ is then given by

$$H_{IS}^{D,sec} = \sum_{i<j} -\hbar\gamma_I^n\gamma_S^n r_{ij}^{-3}(3\cos^2\beta_{ij}-1)S_{z,i}I_{z,j}. \qquad \text{(I-31)}$$

The dipolar Hamiltonian of the combined system (I + S) is then

$$H^D = H_{SS}^{D,sec} + H_{IS}^{D,sec} + H_{II}^D. \qquad (I-32)$$

The size of $H_{SS}^{D,sec}$ can be controlled by dilution, which may also affect the size of $H_{IS}^{D,sec}$ if isotopic substitution of S with I is used, and to simplify the discussion it is assumed that $H_{SS}^{D,sec} = 0$. Since $[H_{IS}^{D,sec}, H_{II}^D] \neq 0$ then under sample rotation H^D does not commute with itself at all times and remains an homogeneous interaction. The fast spinning criterion, $\omega_r > (\Delta\omega^2)_{IS}^{\frac{1}{2}}$, $(\Delta\omega^2)_{II}^{\frac{1}{2}}$, must again be met. Also, if the heteronuclear dipole coupling is removed by rf decoupling, then the strength of decoupling, ω_{1I}, must be greater than the larger of $(\Delta\omega^2)_{IS}^{\frac{1}{2}}$ or $(\Delta\omega^2)_{II}^{\frac{1}{2}}$.

When H_{II}^D is small or can be removed selectively, then $H^D = H_{IS}^{D,sec}$ which commutes with itself at all times and is thus an inhomogeneous interaction. It can therefore be removed by "slow" magic angle sample rotation where $\omega_r << (\Delta\omega^2)_{IS}^{\frac{1}{2}}$, as will be discussed in detail in the next section. The arguments above must be modified when either I,S have a large quadrupole interaction and this is the subject of the next section.

In conclusion, the dipolar broadening can be removed in general by dilution of the observed spins together with magic angle spinning and heteronuclear rf decoupling. The chemical shift transforms as S_z and remains inhomogeneous, thus the isotropic value, σ, can be measured even when the spinning frequency is small compared to the chemical shift anisotropy. Even in the highest magnetic fields, ω_r should approach or exceed typical proton chemical shift anisotropies. Measurement of the scalar or J isotropic couplings strongly depends on the method of dilution and residual broadening of the resonances and will be discussed with the experimental results.

3. Presence of Quadrupole Couplings of Spins Coupled to the Observed Spins

In this section the effects of nuclear electric quadrupole coupling on spectra obtained from rotating solids will be considered. The nucleus with spin $I > \frac{1}{2}$ with an electric quadrupole moment may be the observed spin or it may be coupled to the observed spin via H_{IS}^{D}. Quadrupole couplings can be as large as tens of megaHertz in some cases.

a. Spin ½ Dipolar Coupled to a Single Quadrupolar Nucleus

When the observed nuclear spins, S, are dipolar coupled to an unlike nucleus, $I > \frac{1}{2}$, then the quadrupole coupling of the I spins mixes the I Zeeman states and causes new secular terms to appear in H_{IS}^{D} which do not transform as $\frac{1}{2}(3\cos^2\beta-1)$ and do not vanish under "magic" angle spinning. Linebroadening and some multiplet structure due to this effect have been observed in ^{13}C resonances in solids in which there are $^{13}C - ^{14}N$ and $^{13}C - ^{35}Cl$ bonded pairs. The unusual powder lineshapes which result have been studied in detail theoretically (24), however, residual linebroadening due to other sources makes them difficult to observe.

b. Dilution of Hydrogen: Approach to High Resolution Proton NMR in Solids

The approach of Pines, Vega, and Mehring to observe dilute protons in deuterated solids with double quantum decoupling has been used to observe the high field chemical shift powder lineshape (see Fig. 1). It is a general problem in measurement of the interactions of the internal Hamiltonian in polycrystalline or amorphous solids that the spectra from inequivalent chemical or crystallographic positions overlap. Even for a small number of inequivalent positions the complexity of the

total spectrum makes it difficult or impossible to resolve and identify each component.

Multiple pulse line narrowing studies on single crystals have produced measurement of proton chemical shift tensors in several solids where resonances can be resolved. In the general case there are many inequivalent protons and such studies have been limited in resolution and by the need for single crystals. In this section an approach to high resolution proton NMR by dilution of protons in a deuterated solid combined with magic angle rotation of the sample is described. This approach allows precise measurement of isotropic chemical shifts with high resolution for powder or amorphous samples and can be combined with known methods for retrieving the chemical shift anisotropy.

The relevant internal Hamiltonian for this situation is given by

$$H = H_S^{\sigma,J} + H_{SS}^D + H_{IS}^D + H_{II}^D + H_I^Q. \qquad \text{(I-33)}$$

where $S = {}^1H$, $I = {}^2H$, and all terms are secular with respect to $\mathcal{H}_z = \mathcal{H}_z^S + \mathcal{H}_z^I$. Dilution of the protons removes H_{SS}^D to a very small value. Neglecting H_I^Q for the moment, the problem is then similar to that described above for spin ½; the dipolar coupling $H^D = H_{IS}^D + H_{II}^D$ is homogeneous and the fast spinning criterion must be met. In the typical case $(\Delta\omega^2)_{IS}^{\frac{1}{2}} > \omega_r > (\Delta\omega^2)_{II}^{\frac{1}{2}}$, and fast spinning is not achieved. However, the effect of H_I^Q on H_{II}^D is to cause the deuterons to be semi-like, i.e., H_{II}^D is truncated to the $I_{z,i}I_{z,j}$ term when there is a large difference in the quadrupole couplings of spins i and j. Thus H^D is again inhomogeneous and should be effectively spun away by "slow" spinning. A detailed calculation of the residual $H_{II}^D \neq 0$ under magic angle spinning is postponed until the following section, but it is noted here that it prevents the

complete removal of H_{IS}^{D} and thus adds to the width of the isotropic or narrowed proton resonance.

Thus magic angle sample rotation can remove the dipolar and chemical shift anisotropy broadening of dilute protons giving the liquid-like spectrum. Sharp resonances of inequivalent positions can then be resolved. Experimental results on proton NMR in solids from samples at natural abundance to high dilution are presented in Chapter IV. A discussion of residual linewidth, the use of deuterium double quantum decoupling, and comparison with other high resolution methods is also presented.

4. Observed Spins (S) with Electric Quadrupole Moments

When the observed spins, $S > \frac{1}{2}$, have an electric quadrupole moment the broadening of spectra of polycrystalline or amorphous solids can be enormous, masking all other terms of the internal Hamiltonian. In experiments to be described here, magic angle sample rotation has been applied to remove the inhomogeneous quadrupole broadening and general theoretical considerations are presented here. When $\|\mathcal{H}_Q\| > \|\mathcal{H}_z\|$, the eigenenergies of the nuclear spin states are dominated by the internal Hamiltonian and rotation of the sample then modulates the Zeeman energy which is of little practical interest. Thus only the high field case where $\|\mathcal{H}_z\| > \|\mathcal{H}_Q\|$ or $\|\mathcal{H}_z\| >> \|\mathcal{H}_Q\|$ will be considered. Taking $\mathcal{H}_Q$ as a time-independent perturbation on $\mathcal{H}_z$, the $2S+1$ Zeeman eigenstates are all shifted in first order giving a multiplet of $2S$ transitions symmetrically displaced about the center Larmor frequency. This first order result is shown diagrammatically in Figure 4. The symmetry of $\mathcal{H}_Q$ is such that the $\pm m$ levels are shifted identically in first order. Thus when S

is half-integer, the $+\frac{1}{2} \rightarrow -\frac{1}{2}$ transition remains relatively narrow and when S is integer there is no "central transition". Observation of the central transition for a variety of half-integer spin nuclides has been made for many years in high field NMR. The lineshape is a complex convolution of dipolar, chemical shift anisotropy, and second order quadrupole broadening, the magnitudes of which vary widely among the nuclides and from material to material. Recently, multiple pulse line narrowing and magic angle rotation have been used to further narrow the central transition. Some details and calculations of this effect are given in Appendix A. In the following paragraphs the discussion pertains to integer spin nuclei, e.g., ^{2}H, $^{14}N(I=1)$, for which there is no central transition.

In order to observe the isotropic spectrum the large quadrupolar broadening of powder or amorphous samples must be nearly completely removed. For instance, in the case of deuterium the full powder linewidth (see Fig. 2) may be as large as 260 kHz and a narrowing of over three orders of magnitude is required. The reduction of $H^{Q,sec}$ under magic angle spinning is approximately $f = \frac{1}{2}(3\cos^2\beta-1)$ and if $f \approx 10^{-3}$ is required then the spinner axis must be adjusted within some millidegrees of the magic value. Clearly, the stability and adjustment of the spinner axis must be very precise. Design and application of sample turbines to meet these requirements are described in Chapter II.

Experiments described in Chapter III provide an additional approach to high resolution NMR in solids by observation of deuterium isotopically substituted for hydrogen combined with magic angle spinning. The deuteron quadrupole broadening is nearly completely removed. In the following paragraphs coherent averaging theory is applied to this system.

The results obtained are also applicable to ^{14}N in solids for which the natural abundance is 100%.

1. Average Hamiltonian

Taking the full spin Hamiltonian as in Chapter IB1 without the rf and relaxation terms and performing the average with respect to the Zeeman interaction as in Equations I-28 with $\mathcal{H}_1(t) = \mathcal{H}_z$ gives the expression

$$\begin{aligned}\bar{\mathcal{H}} &= \{\bar{\mathcal{H}}^0\} + \{\bar{\mathcal{H}}^1\} \\ &= \{H^{Q,sec} + H_{SS}^{D,sec} + H^{\sigma,sec} + H^{J,sec}\} \\ &\quad + \{O\omega_Q^2/\omega_0\}\end{aligned} \tag{I-34}$$

where the observed spins are $S = {}^2H$ and "O" = "order of". Since $H^{Q,sec}$ is usually the largest term by far, the spectrum of Figure 2 should result for a powder from Equation I-34 and in that case the effect of the remaining terms are unobservable. Dipolar couplings of S to other nuclei are assumed absent to removed by rf decoupling. As stated previously, the quadrupole coupling makes the deuterium system that of semi-like spins. In the average Hamiltonian formalism a second averaging is performed where $\mathcal{H}_1(t) = H^{Q,sec}$, $U_1(t) = \exp(iH^{Q,sec}t)$. The important consequence of this is that the dipolar coupling is "truncated" and is given by

$$\begin{aligned}\bar{H}_D &= \{\bar{H}_D^0\} + \{\bar{H}_D^1\} \\ &= \{H_{SS}' + \delta(\Omega_{Q,i},\Omega_{Q,j})H_{SS}''\} + \{O\omega_{SS}^2/\omega_Q\}\end{aligned} \tag{I-35}$$

where δ is the delta function and i,j are the usual labels for the spins.

In Equation I-34 the correction terms of $\bar{\mathcal{H}}^1$ are smaller than the corresponding terms of $\bar{\mathcal{H}}^0$ by ω_Q/ω_0 which is usually less than 0.2 for ^{14}N and 0.01 for ^{2}H. Thus $\bar{\mathcal{H}}^1$ can usually be neglected to calculate the resonance linewidth. In Equation I-35 the important term in $\bar{\mathcal{H}}^1$ is reduced by ω_{SS}/ω_Q from the corresponding term in $\bar{\mathcal{H}}^0$. This ratio is usually much less than 0.01 for ^{14}N and on the order of 0.01 for ^{2}H in a perdeuterated solid. Thus $\bar{\mathcal{H}}^1$ is also neglected with respect to $\bar{\mathcal{H}}^0$. In Equation I-35 the $H_{SS}^{D,sec}$ is subdivided into a term $H_{SS}^{'} \propto I_{z,i}I_{z,j}$ and $H_{SS}^{''}$ which contains flip-flop type terms. $H_{SS}^{''}$ is neglected when $\Omega_{Q,i} \neq \Omega_{Q,j}$ and this is the case of semi-like spins mentioned previously. The importance of the higher order terms will become clear in the following paragraphs.

2. Magic Angle Spinning

When the sample is rotated during the NMR experiment the spatial variables, $(\alpha,\beta,\gamma)_i$ of the Hamiltonian are made time dependent. Since the spinning, frequency, ω_r, is in general orders of magnitude less than either ω_0, ω_Q the coherent averaging theory may be applied a third time with respect to the spinning. Since the time dependence is in the spatial coordinates an additional interaction representation is unnecessary and the time dependent $\mathcal{H}_{int}$ is

$$\mathcal{H}_{int}^{rot}(t) = H^{Q,sec}(t) + H_{SS}^{'}(t) + \delta(\Omega_{Q,i},\Omega_{Q,j})H_{SS}^{''}(t) + H^{\sigma,sec}(t) + H^{J,sec}(t) + O(\omega_Q^2/\omega_0)(t) + O(\omega_{SS}^2/\omega_Q)(t) \qquad \text{(I-36)}$$

This equation may be integrated directly over the cycle $t_c = 2\pi/\omega_r$ as

per Equation I-28. The result may be taken to zeroth order, $\mathcal{H}_{int}^{rot(0)}$, since $H^{Q,sec}(t)$ commutes with itself at all times and correction terms $\mathcal{H}_{int}^{rot(1)}$ and higher should be negligible (as well as involving extremely cumbersome eighth rank tensors).

From the discussion in Chapter IB2 it is clear why these small terms must be investigated; $H^{Q,sec}$ will vanish under exact magic angle spinning and they will determine the limiting shape and width of the resonances (12). The zeroth order average of Equation I-36 is

$$\mathcal{H}_{int}^{rot(0)} = H^{\sigma,iso} + H^{J,iso} + H_{SS}''' + \overline{O\omega_Q^2/\omega_0} + \overline{O\omega_{SS}^2/\omega_Q} \qquad (I-37)$$

where

$$H_{SS}''' = \overline{\sum_{i<j} H_{SS}' + \delta(\Omega_{Q,i},\Omega_{Q,j})H_{SS}''} \qquad (I-38)$$

and iso = isotropic. Thus the quadrupolar broadening in solids can be removed by precise magic angle sample rotation and isotropic liquid-like spectra obtained depending on the magnitudes of H_{SS}''' and the residual higher order terms. Since $\omega_{SS} << \omega_Q$, the last term containing ω_{SS} in Equation I-37 gives a negligible contribution to the resonance linewidth. However, it may contribute to relaxation in the quadrupolar spin system and this is discussed in Chapter III. Many cross and higher order terms have been neglected in the above calculation, especially a term of order $\omega_Q\omega_{SS}/\omega_0$ which may also be important in relaxation. Explicit expressions for the terms of Equations I-37 and I-38 are given in Appendix A. In the following paragraphs, the exact removal of $H_{Q,sec}$ and the effects of H_{SS}''' and $O(\omega_q^2/\omega_0)$ are discussed.

3. Residual Homonuclear Dipole-Dipole Coupling

In order to calculate $H_{SS}^{'''}$ the modulation of the quadrupole splitting, Ω_Q, during the rotation cycle due to the time dependence $\gamma'' = \omega_r t$ must be known to evaluate the delta function, δ, at each instant. The quadrupole splitting for an axially symmetric coupling ($\eta = 0$) is illustrated in Figure 5 for a spin pair i,j with $I = 1$. In Figure 5a $\delta = 0$ and in Figure 5b $\delta = 1$. The splitting, $\Omega_Q = \frac{1}{2}(3\cos^2\beta'-1)\omega_Q$ is illustrated in Figure 5c. The modulation of Ω_Q over one rotor cycle, $0 \leq \omega_r t \leq 2\pi$, is shown in Figure 6 for the magic angle case, $\beta'' = \beta_m$, for a spin pair, i,j with different orientations of their principal quadrupole axis in CRS. At various points during the rotation cycle the quadrupole splittings cross, then $\Omega_{Q,i} = \Omega_{Q,j}$ and $\delta = 1$. The width of the crossing region depends on the magnitude of the full homonuclear dipole coupling, $(\Delta\omega^2)_{SS}^{\frac{1}{2}}$, and the steepness with which the quadrupole splittings cross. Since $\omega_{SS} << \omega_Q$ the crossing regions are a small fraction of the rotor cycle and $H_{SS}^{'''}$ should be reduced to a small fraction of $H_{SS}^{D,sec}$. Exact calculation of $H_{SS}^{'''}$ in Equation I-38 requires knowledge of crystal and/or molecular structure as well as a summation over all orientations $(\alpha',\beta',\gamma')_{ij}$, i.e., a "powder average". Due to this limitation an empirical approach is taken. Dipolar broadening of the resonances is extracted from other contributions to the width and correlated qualitatively to the structure in Chapter III.

4. Second Order Quadrupole Effects

Since the full quadrupole Hamiltonian, $\mathcal{H}_Q$, does not commute with itself at all times there appeared in $\bar{\mathcal{H}}^1$ with respect to the Zeeman interaction representation in Equation I-34 a residual term of order ω_Q^2/ω_0 which can be written

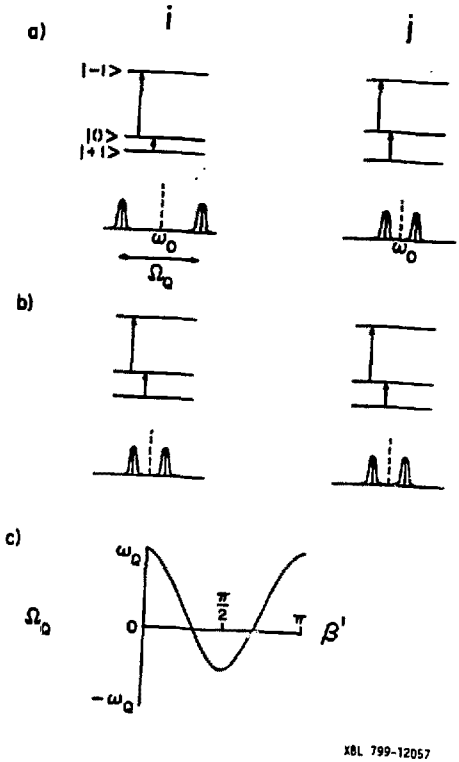

Figure 5

Eigenstates and quadrupole splitting of spin I = 1 deuterium in an axially symmetric field gradient in high magnetic field. (a) Left and right hand sides indicate spins i and j with unequal values of their quadrupole splitting, Ω_Q. Mutual spin flips between deuterons with unequal Ω_Q are quenched in first order. (b) When $\Omega_{Q,i} = \Omega_{Q,j}$, mutual spin flips via the dipolar coupling $I_+^i I_-^j + I_-^i I_+^j$ can occur. (c) The quadrupole splitting varies as the angle, β', between the unique quadrupole axis and the direction of the external magnetic field.

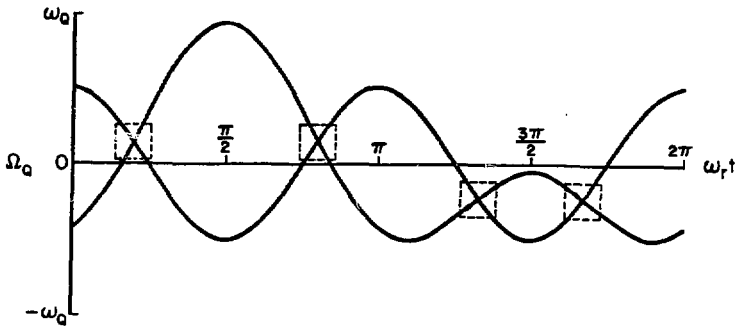

XBL 799-12056

Figure 6

Modulation of the quadrupole splitting, Ω_Q, of two deuterons in a rotating sample over one rotation cycle; $0 \leq \omega_r t \leq 2\pi$. The two spin $I = 1$ nuclei have different orientations of their unique quadrupole axis with respect to the axis of sample rotation. *Dashed boxes* enclose regions where mutual spin flips can occur in first order due to the matching of quadrupole splittings.

$$\bar{\mathcal{H}}_Q^1 = \omega_Q^2/\omega_0 \{r_0 r_1 [S_1^Q, S_0^Q] + r_0 r_{-1} [S_0^Q, S_{-1}^Q]$$

$$+ \tfrac{1}{2} r_0 r_2 [S_2^Q, S_0^Q] + \tfrac{1}{2} r_0 r_{-2} [S_0^Q, S_{-2}^Q]\} \qquad \text{(I-39)}$$

where $S_0^Q = 3S_0^2 - S^2$

$$S_{\pm 1}^Q = S_{\pm 1} S_0 + S_0 S_{\pm 1}$$

$$S_{\pm 2}^Q = S_{\pm 1}^2 \qquad \text{(I-40)}$$

and the r_i contain the spatial variables derived from the $R_{\ell,m}$ and are given explicitly in Appendix A. These terms have been evaluated in detail by Maricq and Waugh and their results are summarized here. Equation I-39 can be written in the form $AI_0 + BI_x$ where A, B contain all but the spin operators in Equation I-39. The diagonal part, AI_0, corresponds to the result obtained from time independent perturbation theory in second order and is sufficient to describe the average Hamiltonian when $H^{Q,sec}$ is large. However, under "magic" angle spinning, $H^{Q,sec} = 0$, and both A and B terms are necessary. Both A,B contain tensors up to fourth rank and do not vanish when $\beta'' = \beta_m$. Also, $\bar{\mathcal{H}}_Q^1$ does not commute with itself at all times under sample rotation and in order to observe $\bar{\mathcal{H}}_Q^1$ experimentally the fast spinning criterion for an homogeneous interaction must be met, i.e., $\omega_r > 0\omega_Q^2/\omega_0$. The important point is that $\mathcal{H}_Q^1$ is a function of $(\alpha',\beta',\gamma')_i$, or simply β_i' when $\eta = 0$, and thus produces a "powder pattern" broadening.

The fast spinning criterion is easily met for ^2H where usually $\omega_Q^2/2\pi\omega_0 < 1$ kHz. Furthermore, in this case the time independent perturbation theory result to second order gives a close approximation to $\bar{\mathcal{H}}_Q^1$ in magnitude with the same lineshape. Since a simple analytic solution can

be obtained from the perturbation theory result, this calculation was performed. The results for exact magic angle rotation, $\beta'' = \beta_m$, and the nonspinning case are shown in Figure 7. The lineshape in the nonspinning case, which is not normally observed since it is masked by the first order $H^{Q,sec}$, is shown in Figure 7a for an axially symmetric spin-1 quadrupole coupling with principal axis V_{zz}. Under "fast" magic angle rotation this lineshape is reduced to that shown in Figure 7b. The result is that the residual quadrupole coupling in magic angle rotating solids contributes both a broadening of width $0.0268\ \omega_Q^2/2\pi\omega_0$ Hz and a "downfield" shift of the resonance by $0.1324\ \omega_Q^2/2\pi\omega_0$ Hz. As the axis of sample rotation deviates from the "magic" setting, the large first order $H^{Q,sec}$ grows rapidly and the lineshape quickly returns to that depicted in Figure 2, reduced by approximately $(\frac{1}{2})(3\cos^2\theta''-1)$. A detailed description of calculation is given in Appendix A and comparison with experiment is given in Chapter III.

5. Rotational Echoes and Removal of $H^{Q,sec}$

The result of the coherent averaging theory is that the evolution of the spin density matrix is known at multiples of the cycle time. The results above indicate that the quadrupole, chemical shift anisotropy, and dipolar broadening may be removed under magic angle rotation by observation of the nuclear free induction decay (fid) at multiples of the spinner cycle. When the internal Hamiltonian is composed of large inhomogeneous anisotropic interactions, e.g., $H^{Q,sec}$, $H^{\sigma,sec}$, and the system is rotated slowly with respect to the anisotropic linewidth (see Figs. 1,2) and fast with respect to the smaller homogeneous width of the spin packets comprising the system then the magnetizations of the spin

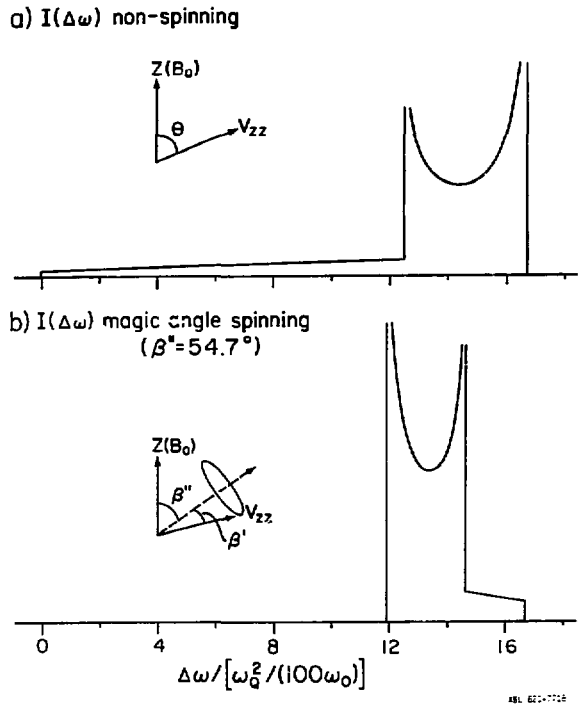

Figure 7

Theoretical powder pattern lineshapes, $I(\Delta\omega)$, for the second order perturbation correction to the Zeeman energy for an axially symmetric spin I = 1 quadrupole coupling in high magnetic field. a) Lineshape for non-spinning sample which is normally unobservable due to the large first order term. b) Lineshape for magic angle rotating sample illustrating the broadening and shift of the resonance line from the Larmor frequency.

packets will dephase during the rotor cycle nearly the same as they do in the non-spinning fid. After each rotor cycle they must rephase in a rotational echo since the average of the anisotropic interaction over the cycle is the same for all spin packets. The magnitude of the echo is reduced from cycle to cycle by the slower dephasing due to non-zero average of the anisotropy when the spinner axis is offset from magic, different σ_{iso}^{P} for distinct species P, and T_2 decay due to the homogeneous dephasing. Thus the fid after a single rf pulse appears as a train of rotational echoes as illustrated by the deuterium fid in Figure 8 of per-deuterohexamethylbenzene rotated about the magic axis at 4.0 kHz. In Figure 8a is shown the on-resonance rotational echo fid and in Figure 8b is shown the isotropic decay obtained by sampling the peaks of the echoes. Corresponding fid's under the same conditions, but 0.4 kHz off-resonance are shown in Figures 8c and 8d.

6. Large Quadrupole Couplings: ^{14}N

The quadrupole interaction for ^{14}N ranges from approximately $\omega_Q/2\pi$ = 0.1 to 3 MHz. The homonuclear dipole coupling is usually less than 1 kHz and H^D, H^J can be neglected under sample rotation. The zeroth order average Hamiltonian under sample rotation from Equation I-37 is

$$\bar{\mathcal{H}}_{int}^{rot(0)} = \bar{\mathcal{H}}^{\sigma,iso} + \overline{\delta\omega_Q^2/\omega_0}. \qquad (I-41)$$

The homogeneous second order term thus ranges from a few Hertz to some 7 kHz in the highest magnetic fields available (12 Tesla, $\omega_0/2(^{14}N)$ = 37 MHz) with the limits of ω_Q above. For the larger ω_Q values, higher correction terms are important and Equation I-34 becomes

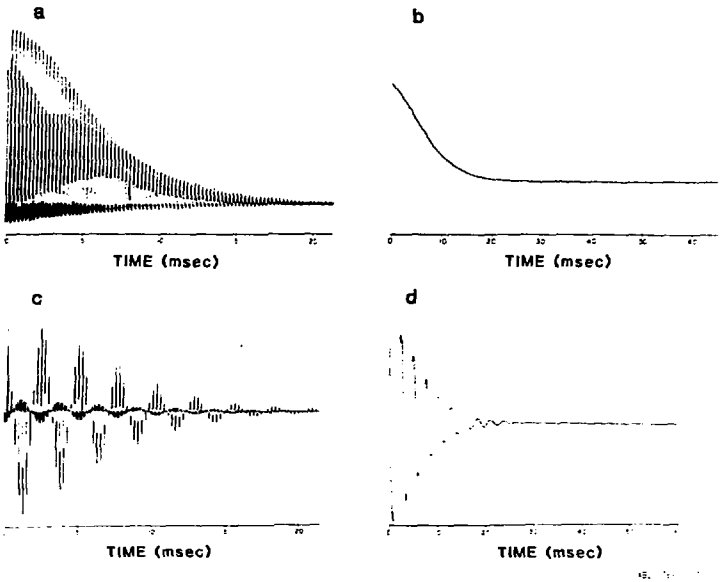

Figure 8

Deuterium free induction decays in per-deuterated hexamethylbenzene rotated about the magic angle at 4.0 kHz. a) On resonance decay consisting of rotational echo train. b) Isotropic decay obtained by sampling the peaks of echoes in a). c) Off resonance rotational echo train. d) Isotropic decay obtained by sampling the peaks of echoes in c).

$$\bar{\mathcal{H}} = \{\bar{\mathcal{H}}^0\} + \{\bar{\mathcal{H}}^1\} + \{\bar{\mathcal{H}}^2\}$$

$$= \{H^{Q,sec} + H^{\sigma,sec}\}$$

$$+ \{0\omega_Q^2/\omega_0 + 0\omega_Q\omega_\sigma/\omega_0\} + \{0\omega_Q^3/\omega_0^2\} \qquad \text{(I-42)}$$

where a cross term of quadrupole and chemical shift terms may become important. Furthermore, the various terms of Equation I-42 do not commute at all times under sample rotation and the spinning average would be needed to higher order; $\bar{\mathcal{H}}_{int}^{rot} = \mathcal{H}_{int}^{rot(0)} + \mathcal{H}_{int}^{rot(1)} + \ldots$ (12). Also, the quadrupole coupling for ^{14}N is usually asymmetric, $\eta \neq 0$. Including the asymmetry will change the lineshape under spinning (as depicted in Fig. 7), but should not drastically change the values given above.

At a field of 12 Tesla the full range of ^{14}N chemical shifts may be up to some 30 kHz. In order to resolve differences $\Delta\sigma \simeq 300$ Hz = 8 ppm it is desirable that the broadening, $0.0268\ \omega_Q^2/2\pi\omega_0 < 300$ Hz. With these values and noting earlier discussion in this chapter and Appendix A a practical limit of $\omega_Q/2\pi \simeq 0.6$ MHz is expected for magic angle spinning with spinning synchronized data acquisition. For this case the rotation frequency should exceed the full range of $0\omega_Q^2/\omega_0$ (see Fig. 7a) which is about 2 kHz and easily satisfied. Also, three experimental details become important for the larger ω_Q's. First, the sensitivity to spinner axis adjustment to remove $H^{Q,sec}$ precisely is several times greater. Second, spinning synchronized acquisition of the fid limits the observed bandwidth (with quadrature phase detection) to the spinner frequency. "Foldover" of isotropic resonances would have to be analyzed by collecting spectra at different spinning frequencies (12). Third, nuclei of different sites may have the same $H^{\sigma,iso}$, but different ω_Q's. The "second

order" residual quadrupole shift can then aid in separating the resonances.

The difficulties associated with large values of ω_Q can be eliminated by limiting the effective Ω_Q in an experiment to some fixed value, e.g., 0.3 MHz. This can be accomplished by selective excitation and/or observation of only a fraction of the powder. Referring to Figure 2, a slice of the full powder lineshape centered about ω_0 with a fraction, f, of the full powder linewidth contains f of the full integrated intensity. Since $H^{Q,sec}$ is usually by far the largest term in the internal Hamiltonian, all distinct chemical or crystallographic sites are represented in the slice. Such a fraction still contains all orientations (α',β',γ') with respect to the spinner fixed frame and restriction of β' to $\pm\epsilon$ (orientations which remain close to the β_m in LAB) achieves a substantial reduction of the effective second order quadrupole powder lineshape. Weak rf irradiation during a time not short compared to the rotor cycle and audio filtering of the fid to a bandwidth of the effective $_Q$ or selective cross polarization with Hartmann-Hahn matching (25) could be used to provide the restriction of β'.

Thus magic angle spinning can be applied to obtain high resolution single quantum spectra in solids for integer spin systems with arbitrary ω_Q. Magic angle spinning may also be applied when double quantum transitions are observed and experiments on deuterium in solids are described in Chapter III for both cases along with sensitivity enhancement by cross polarization for both cases. Due to lack of time, experiments on ^{14}N have not been performed. When ω_Q becomes very large, e.g., for ^{14}N in many solids, both single and double quantum resonances can be severely broadened to second or higher order as described above which results in

a loss of resolution and sensitivity. The methods mentioned above can narrow the observed resonances to recover the resolution and it is desirable to use a selective cross polarization method to enhance sensitivity.

II. TECHNOLOGY

A. Spectrometers

Experiments were performed on two homebuilt high field pulsed Fourier transform instruments. Each was designed for rapid changeover of the observed frequency for concurrent multinuclear studies. Their main features are very similar and are described below.

1. Magnets

The superconducting magnets used were Bruker Instruments Co. 42.7 kGauss ($\omega_0/2\pi(^1H)$ = 182 MHz) and Bruker Instruments Inc. 84.7 kGauss ($\omega_0/2\pi(^1H)$ = 361 MHz) with Oxford dewar. Resonance frequencies of various nuclides were given in Table I.

2. Pulse Programmer

Each instrument was equipped with a versatile solid state pulse programmer based on an INTEL 8080 or Z-80 microprocessor which are described in full detail elsewhere (26). Software programs (listed in Appendix C) are executed by the microprocessor to output a real time hexadecimal word sequence from a RAM/FIFO memory system. The word sequence defines the pulse programmer real time logic level output channels which trigger the spectrometer and execute the experiment. Each word is initiated by a low level pulse on the LOAD line. The entire system is clocked at a rate of 10 MHz with a tick of 100 ns.

3. Radio Frequency Generation

The low power rf is generated by mixing a local oscillator (LO) with an intermediate frequency (IF). The cw LO is generated by

multiplication or direct use of a frequency synthesizer output. A 30 MHz IF is split into four channels with "quadrature" phase (X, Y, $\bar{X}$, $\bar{Y}$) and gated by the pulse programmer. The LO and IF are mixed to produce the irradiation rf. This is gained by high power transmitters; 1) a modified 2 kWatt tuned tube Henry Radio L7 (up to 60 MHz), 2) broadband Amplifier Research models 100LM13 (used for 200 Watt output for frequencies up to 182 MHz) and 200L (used for up to 500 Watt output for frequencies up to 182 MHz), and 3) two homebuilt 200 Watt units for 361 MHz based on either EIMAC tube 4CX-250B or Motorola transistors MRF-327.

4. Receiving Section

The nuclear signal is mixed down with the LO and compared by quadrature phase sensitive detectors to the IF to produce the audio signal. The preamp is two-stage broadband and based on transistors Avantek Inc. UTO-511 and UTO-512.

5. Data Acquisition

The audio signal is digitized with two Datel Systems Inc. SHM-2 sample and hold and two ADC-EH10B analog to digital converters. Triggering of the pulse programmer and storage of data is done with a Data General NOVA 820 (32 k core memory) minicomputer. The maximum observable spectral window was 200 kHz.

In order to sample the fid in synchronism with the probe sample spinner a tachometer system was used and coupled to the pulse programmer. An optic fiber cable (DuPont Crofon) was used to carry light from a lamp to the rotor surface. A return cable monitored the reflected light which was modulated at the spinner frequency due to a blackened area on the spinner surface. The modulated reflection was converted

with a phototransistor and amplified to a square wave which was interfaced directly to the pulse programmer LOAD line. Optimal stability of the spinner synchronous time base was better than 1 microsecond. Schematics and details of the tachometer system and interface appear in Appendix B.

B. Sample Probes

1. High Frequency Sample Turbines

a. Conical (Andrew)

A high frequency sample turbine probe head of the conical design first used in NMR by Andrew et al.(27) is shown in Figure 9. The rotors, manufactured from Delrin and Kel-F polymers, are driven by streams of compressed gas oriented tangentially to the conical surface. The rotor rides in the base cup on a cushion of gas. The NMR coil is fixed in space just outside the sample chamber. Stable spinning frequencies between one and four kiloHertz could sometimes be maintained with Delrin rotors and up to 1.7 kHz with Kel-F rotors. Orientation of the axis of rotation with respect to the external magnetic field was controlled by rotating the base cup assembly with a worm screw. Overall performance of the system in starting and maintaining stable rotation was poor. Performance was greatly enhanced by coating the NMR coil with epoxy or by using a "magic finger", i.e., a small strip of thin material or a human finger gently touching the outer surface of the sample chamber. Similar effects have been observed by a number of workers which has led to a variety of modifications and improvements in performance (28) and reliable systems are commercially available. A general feature of this design is a wobble or precession of the rotor axis which limits the adjustment of the axis to the magic angle setting.

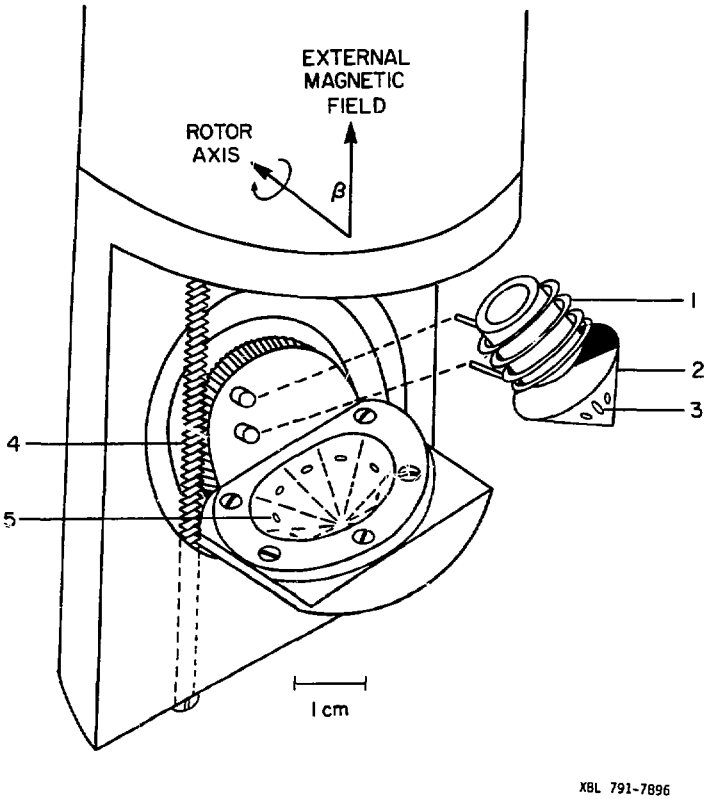

Figure 9

NMR sample spinning probe head with rotor of the Andrew-Beams design: 1) NMR coil, 2) rotor, 3) gas drive flute, 4) rotor axis angle (β) adjust screw, 5) rotor gas drive gas outlet.

b. Cylindrical

Due to the difficulty of holding one finger on the sample spinner and reaching the spectrometer console at the same time a new cylindrical spinner system was developed which allows more routine experimentation and meets the critical requirements of rotor axis stability for the deuterium experiments (29). The complete high speed turbine probe head is shown in Figure 10. The basic rotor design is that of a cylinder riding in gas bearings with end cones and packaged to fit the bore of a superconducting magnetsystem. A barrel shaped rotor system was first used in NMR by Lowe (10). Spinners of cylindrical design were first used by Schneider and Doskocilova et al. (30), and in Tallinn (11,13) after which the design described below was based. Several other similar designs have been developed (31,32) including a recent one by Doty et al. (33) which offers promising ease of operation.

All parts except screws were machined from Delrin polymer. The path of the operating gas through channels in the top and side plates and into each end of the cradle is shown in Figure 10. The magic angle adjustment is made by rotating the cradle with a worm screw. The worm is driven by a reducing gear and pinion on top of the probe outside the magnet so that an increment of less than 0.003° was possible. An access hole was provided on top of the cradle for the leads to the NMR coil and for operating gas escape from the stator centerpiece. The ends of the stator were enclosed by cover plates with exit holes to allow free escape of the operating gas. Temperature of the spinner can be readily controlled by the temperature of the operating gas. The high temperature limit is due mainly to the melting of sample or probe components and the low temperature limit is due mainly to the low temperature limit of the input

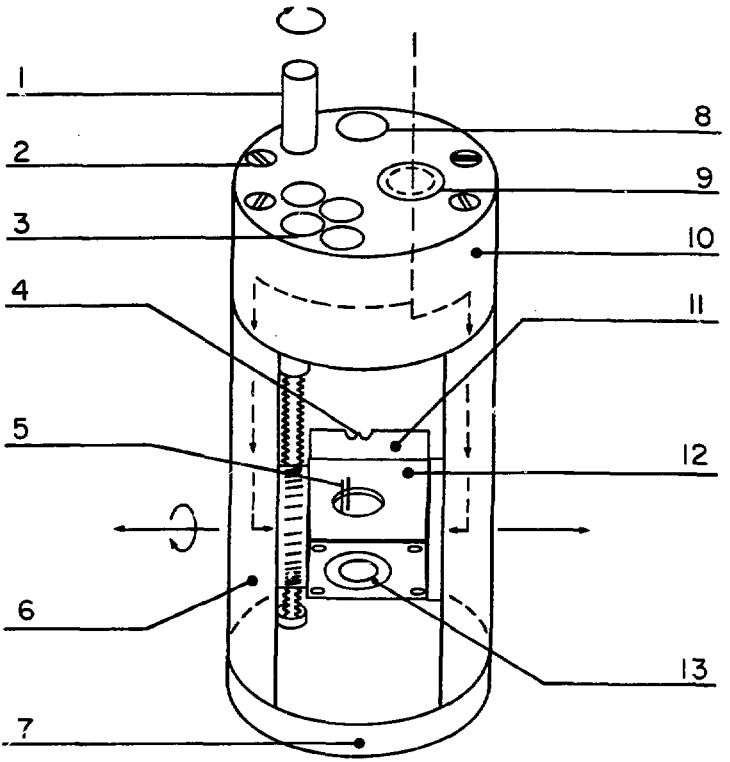

XBL 802-8315

Figure 10

Cylindrical gas-bearing type sample spinning probe head for superconducting magnet bore: (1) worm screw for cradle angle adjustment, (2) top plate-side plate machine screws, (3) holes for rigid copper coaxial cable, (4) inlet holes for fiber optic cables, (5) NMR coil leads, (6) side plate, (7) bottom plate, (8) hole for fiber optic cables, (9) spinner operating gas inlet holes for vacuum-jacket transfer line, (10) top plate, (11) stator end cover plate, (12) cradle, (13) stator.

operating gas. Compressed air or nitrogen is the best operating gas since the supply can be made continuous and virtually unlimited and is inexpensive. Helium requires substantially less pressure for operation and is desirable for low temperature work since a heat exchanger can easily be made from copper tubing immersed in liquid nitrogen. However, it is more expensive and causes arcing in the NMR coil with rf of 182 MHz or greater (and perhaps at lower frequencies) and must be isolated from the coil.

Designs for 8, 7, and 5 mm diameter rotor systems have been developed and detailed mechanical drawings are given in Appendix B. The pressure/frequency specifications vary with a variety of mechanical factors. Available pressures for compressed air of about 50-100 psig are generally required, while input pressures up to about 20 psig are usually used for the spinner. The long time stability of the spinning frequency depends on the long time stability of the input pressure. It is desirable to operate from a stable input source, e.g., a large holding volume compressed air system with few other users. Rotation frequencies of over 500,000 rpm (9-10 kHz) were obtained with the 5 mm version. Typical frequencies during experiments were 3-6 kHz for the 5 mm version and less than that for the larger diameters. Rotor instabilities are clearly the larger with increasing rotor diameter and sample weight and volume leading to lower frequencies of operation. This is also apparent from the data cited in references above.

A cross section along the cradle axis is shown in Figure 11. The separate paths of the drive and bearing gas, which are controlled by separate pressure regulators, into ballast chambers about the circumference of the stator is indicated. Rotors are reuseable and machined from

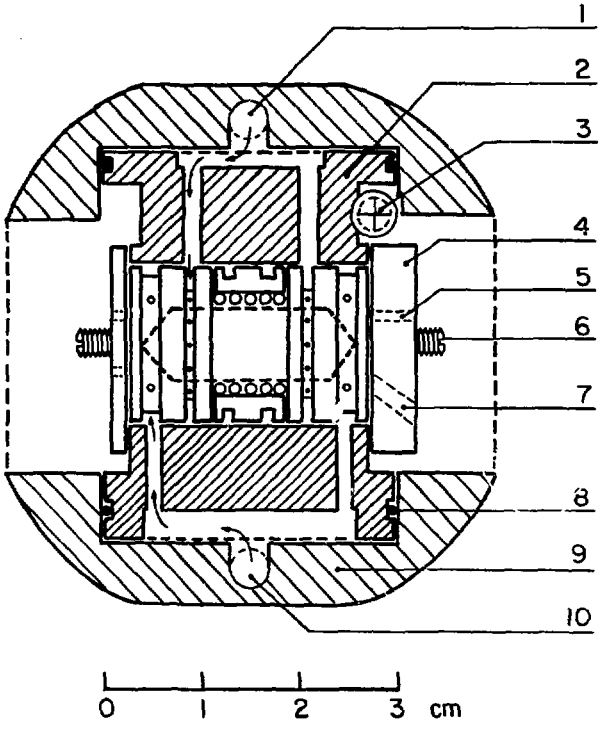

Figure 11

Cross section of cylindrical gas-bearing spinner probe head along spinner axis: (1) gas bearing gas inlet hole, (2) cradle, (3) worm screw for cradle angle adjustment, (4) stator end cover plate, (5) gas exit hole, (6) rotor end stop screw, (7) fiber optic cable inlet hole, (8) o-ring, (9) side plate, (10) turbine drive gas inlet hole.

Delrin and Kel-F polymers. Corning Macor was also used as a material for rotor tubes. A minimum wall thickness of about 0.6 mm for the polymer tubes was necessary for handling. Machining was performed on standard equipment to tolerances of 0.0127 mm (~0.0005 in) where necessary, however, a finished polymer piece does not maintain that tolerance uniformly. It is necessary that cutters be maintained "razor sharp" for the polymers. Flutes in the end cones or caps were cut some 0.4 mm deep such that they present a flat face to the drive gas stream, but their dimensions were not critical. Also shown in Figure 11 are the stator end cover plates, the thicker one serving to hold two fiber optic cables near the cap. Brass machine screws with polished ends in both cover plates acted as end stops for the spinner. To operate at high speed, one end screw was first adjusted to center the spinner in the stator. Then with the operating gas on, the other end screw was tightened against the spinner and backed off just until a stable rotation occurred with no vibration. Total rotor end clearance was usually about 0.2 mm.

Caps must fit tightly into the tubes so that they are not pushed out by the sample at frequencies above about 4 kHz and for stable rotation at lower frequencies. Threaded caps and tubes can be used to avoid this problem at the higher frequencies. The points of the caps act as thrust bearings with the brass cover plate screws to maintain the rotor position. Thus it is essential that the points are sharp. The points of the polymer caps tend to wear out after some uncontiguous hours to days of use and another material, e.g., hard stone or ceramic, is probably the best solution.

Kel-F is a fluorinated polymer and gives no ^{13}C signal in a Proton-Enhanced ^{13}C spectrum and also gives no proton signal. Delrin, $(-CH_2O-)_n$, is one of the strongest polymers and is the better material when observing nuclides other than ^{13}C, ^{1}H. Ceramic materials have been used in some designs and are much stronger, but more delicate since they are brittle. A survey of materials is given in Reference 33.

A cross section of rotor and stator is shown in Figure 12. The stator is composed of three sections with the gas bearings and drive contained in the outer sections which are mirror images. The point group symmetry of combined spinner and stator is D_{4h}, but it is not necessary to orient the outer stator sections with respect to each other. Two gas bearings are located at either end of the spinner tube and a difference of 0.05 to 0.08 mm between bearing i.d. and spinner o.d. worked best. A cross section (B-B in Fig. 12) of the bearing illustrates the twelve cylindrical gas inlet holes which are at equal intervals and normal to the spinner axis. The spinner is driven by gas jets shown in cross section A-A in Figure 12. The four drive gas holes on either end were arranged so that the stream contacts the face of the flute at 60% to 65% of the distance from point to outer edge of the cap. This was the most critical dimension and was adjusted using the values of θ and d in Figure 12. Further details of dimensions are given in Appendix F. In practice, a slant bearing was actually used. The bearing may also act in part as a driver by drilling the bearing holes with an offset as shown in cross section A-A. This reduces the pressure required for the drive, but also reduces the load handling of the bearing. Striking a compromise with a bearing offset of d = 1.15 mm or slanting only every other bearing hole worked best.

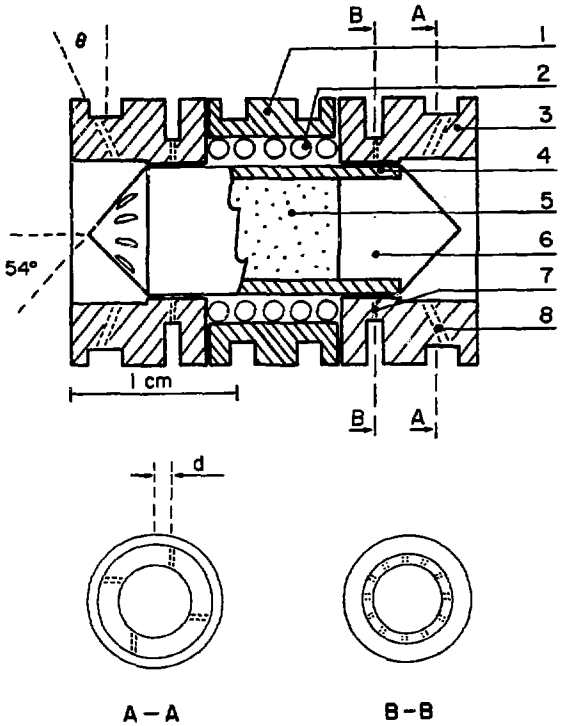

Figure 12

Cylindrical spinner and stator: (1) center coil section, (2) NMR coil, (3) drive and bearing section, (4) rotor tube, (5) sample chamber, (6) rotor cap, (7) gas bearing inlet hole, (8) turbine drive inlet hole.

The stator centerpiece serves to hold the NMR coil and maintain a sufficient back pressure for the bearings. The coil may be wound inside the centerpiece, as shown in Figure 12, or on the outside so that a smooth surface faces the rotor. Either version gives an excellent sample filling factor. The latter was found to be slightly better overall. Rotors would generally spin at some several hundred Hz on bearing gas alone for the straight bearing, and up to about 2.5 kHz on bearing gas alone for the slant bearing. A gas exit hole 1-2 mm in diameter in the centerpiece or equivalent space about coil leads for the inside type coil was necessary for stable operation. When spinners did not readily reach high speed stability, they were usually brought to a stable condition by lowering the bearing input pressure to near zero. A sudden stabilizing usually occurred followed by a rapid increase in spinning frequency, after which the input pressures were adjusted to final value. This is due to the "magic finger" effect as the spinner momentarily touches the bearing surface at low bearing pressure.

An important feature of the system described above is that it can be fabricated with standard machine tools and does not require any special sample preparation. Powder samples may leave space in the chamber or may be compressed to fill the chamber. Crystals may be rotated when packed with some filler, e.g., cotton or another powder. The frequency stability could typically be maintained to ±0.5%. Stability of the rotor axis during smooth operation was better than one millidegree. Change of the input pressure altered the axis by several millidegrees. The fineness of adjustment of the axis was less than three millidegrees. The latter three facts are inferred from the results of the deuterium experiments presented in Chapter III.

2. Probe Radiofrequency Circuit

The rf circuit of the probe is based on the design of Cross et al. (34). In this section their results are reviewed and some practical modifications described. For double resonance experiments the use of a single double-tuned coil is desirable since the inhomogeneity of the rf field will be identical for both frequencies. The usual NMR probe circuit has a series and parallel capacitance to the coil with the components placed in the region near the coil. A coaxial transmission line connects that circuit to the rf transmitters and receiver section. The impedance transformation due to the transmission line is (35)

$$Z_{in} = Z_0[Z_L + Z_0\tanh(\gamma L)]/[Z_0 + Z_L\tanh(\gamma L)] \qquad \text{(II-1)}$$

where Z_{in} is the input impedance of the line, Z_0 is its characteristic impedance (50 ohms real), Z_L is the load impedance, γ is a complex propagation constant, and L is the length of the line. The probe circuit is the load and is tuned to the NMR frequency with its impedance adjusted to $Z_L = R_L = 50$ ohms. Since $Z_0 = R_0 = 50$ ohms, then $Z_{in} = R_{in} = 50$ ohms and the probe is matched to the transmitter and receiver circuitry.

In the design of Cross et al. the complex impedance of the coil is not matched in the region of the probe head. A transmission line tuning method is used in which the probe circuit is matched at a point outside the probe at the end of a "50 ohm" transmission line which acts as a component of the circuit. Thus the transmission line is "unmatched" and Z_L, Z_{in} are complex. As long as Z_{in} is inductive, $\mathrm{Im}(Z_{in}) > 0$, then high Q factor capacitors may be added to the transmission line input outside the probe to tune and match the entire circuit. It is desirable to keep L as small as possible since it is unmatched and adds to the inductive loss of the probe circuit.

The probe circuit used in this work is shown in Figure 13. Isolation between low frequency (LF) and high frequency (HF) sides is obtained by the use of coaxial quarter wave "stubs", $L_3 = \lambda_{HF}/4$. The open ended stub has a high input impedance for the LF and is a short to ground for the HF. The shorted stub is a short for the LF and high input impedance for the HF. Capacitor Q, which does not appear in the design of Cross et al., was empirically found to improve the isolation. The coil dimensions were fixed by the dimensions of the sample spinner stator and cradle with an inductance in the range 0.1 to 0.5 H. The length L_2 was fixed by the probe length, from 45 to 90 cm. The external capacitors and P,Q were easily empirically adjusted to tune and match the probe. Obtainable overall Q factors for the probe were 50-100 for the LF and up to 200 for the HF and were as high as those obtained by other methods. An advantage of this design was that a transmission line of length L_1 could be inserted on the LF side so that a rapid changeover of the LF over a wide range of NMR frequencies (0-200 MHz) could be made for multinuclear studies.

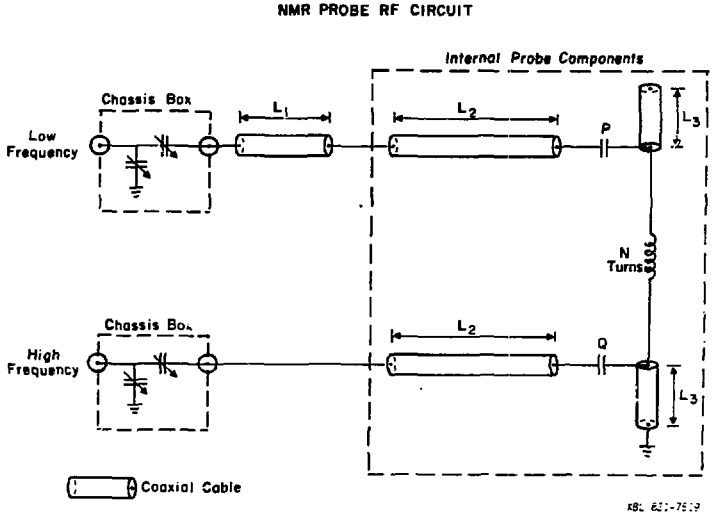

Figure 13

Radiofrequency design for double-tuned, single-solenoid coil NMR probe after the design of Cross et. al. (Reference 34).

III. HIGH RESOLUTION DEUTERIUM NMR OF SOLIDS

A. Approach to High Resolution

In this chapter experimental results on quadrupolar nuclei in rotating solids will be presented. As shown in Chapter I, magic angle spinning can be used to remove the broadening due to the internal Hamiltonian and to observe high resolution isotropic chemical shift spectra. Details of experimentation and results and comparison with theory are given here. The bulk of the work is motivated by the desire to observe isotropic spectra of deuterium in solids. All results were obtained at room temperature.

The basic approach to high resolution deuterium NMR in solids is illustrated by the spectra in Figure 14 of an equal deuterium mole mixture of per-deutero hexamethylbenzene (per-d-hmb) and 20% randomly deuterated ferrocene (36). The top spectrum is the non-spinning case and consists of the overlapping powder patterns of the two components of the mixture. The inner peaks are the singularities of the per-d-hmb pattern and the outer peaks are those of the ferrocene pattern. From these we can immediately measure the quadrupole coupling "constants" as the splitting between the peaks in each pair which are 16 kHz (per-d-hmb) and 73 kHz (ferrocene). The shoulders of the per-d-hmb pattern are visible, but those of the ferrocene pattern are not which is due to the strength of the rf pulse used as will be discussed in a later paragraph. Previous measurements of deuterium quadrupole couplings in solids show that the variation in the coupling constant for carbon bonded deuterons is roughly 20% and that the asymmetry is usually $\eta < 0.2$, with $\omega_Q = 130$ kHz (37). The coupling constants evident in Figure 14 are the

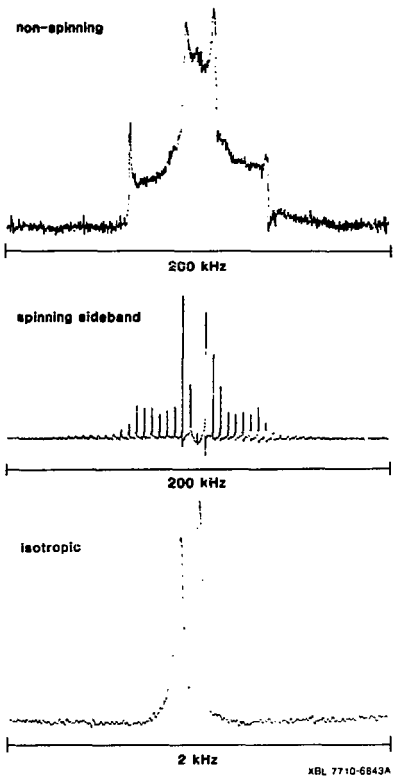

Figure 14

Demonstration of solid state deuterium spectra of an equal deuterium mole mixture of per-deuterated hexamethylbenzene and 20% deuterated ferrocene: (top) overlapping quadrupole powder patterns of the two components, (middle) spinning sideband spectrum from Fourier transform of rotational echo free induction decay, (bottom) isotropic chemical shift spectrum from Fourier transform of synchronously sampled free induction decay.

reduced average couplings observed under rapid molecular rotation at room temperature. The well-known and approximately uniaxial rotations in this case are the rotation of the methyl group about its C_3 axis and rotation of the molecule about its C_6 axis for hmb, and a rotation of the cyclopentadienyl rings about their C_5 axes in ferrocene. Applying Equation I-30 twice for hmb, the reduction factor for $\eta = 0$ is $\frac{1}{2}[3\cos^2(180° - 109.5°)-1] = 0.333$ for the methyl rotation and $\frac{1}{2}[3\cos^2(90°)-1] = 0.500$ for the molecular rotation; giving $\omega_Q' = (0.33)(0.50)9130) \approx 21$ kHz. Applying Equation I-30 for the ferrocene rotation; $\omega_Q' = (0.50)(130) = 65$ kHz. Differences between these rough estimates and Figure 14 are due to the actual $\omega_Q \neq 130$ kHz, $\eta \neq 0$, and distortion of the motion from simple uniaxial free rotation. The effects of motion in these deuterated solids have been studied in detail previously (38,39).

The middle spectrum in Figure 14 shows the distribution of the total powder spectrum into a set of spinning sidebands when this sample is rotated about the magic axis at 4.0 kHz. The sideband spectrum is the Fourier transform of a rotational echo fid as depicted in Figure 8a. The sidebands are spaced at 4 kHz and their envelope approximates the non-spinning pattern since $\omega_r << \omega_Q$. Sampling the fid in synchronism with the rotation effectively folds - in the sideband spectrum in such a way as to produce the lower spectrum in Figure 14, the isotropic chemical shift spectrum in which the resonances of the two components are resolved.

Thus relatively slow magic angle sample rotation can be applied to remove the broadening from spectra of deuterium in powders. High power proton decoupling is used to remove the effect of H_{IS}^D, the proton-deuterium dipole-dipole coupling, for selectively or partially deuterated materials. This is especially effective when the strength of decoupling,

$\omega_{II} >> \omega_r$, so that both the decoupling and magic angle rotation act independently to reduce H_{IS}^D on their separate time scales (3,12,14) and this is an easy requirement to meet. In the rest of this chapter it is assumed where not specifically stated that decoupling is applied to remove the effects of H_{IS}^D, where I is the decoupled heteronuclear spin which is usually ^1H. Dipolar coupling to other spins, e.g., ^{13}C, ^{14}N, is generally negligible when deuterium is observed since they are usually naturally dilute and/or the γ_I, $\gamma_S(^2H)$ involved are relatively small and magic angle rotation "spins it away". Also, the spectrum from Fourier transformation of a synchronously sampled fid is referred to as the "isotropic" spectrum.

B. Measurement of Quadrupole Anisotropy

It has long been known that a Hahn spin echo is observed for integer spin quadrupolar nuclei in solids by application of a $90_\phi - \tau - 90_{\phi+\pi/2}$ pulse sequence (1,40-41). This sequence is commonly used to eliminate the effect of receiver dead-time since the echo appears at a time τ after the second pulse and Fourier transformation of the decay half-echo gives the undistorted powder pattern. In a rotating solid the fid is composed of a train of rotational echoes (see Fig. 8) and Fourier transformation of the decay half of the first echo appearing outside the receiver dead-time, usually the largest echo, also gives the non-spinning powder pattern in the limit $\omega_r << \omega_Q$. Since the latter is the usual case, then Fourier transformation of rotational echoes has utility in measuring ω_Q when one is prepared to do the rotating sample experiment anyway.

In Figure 15 is shown the rotational half-echo decay and its Fourier transform of per-deutero-para-dimethoxybenzene powder with magic angle rotation at 1.24 kHz (42). The motionally reduced ω_Q' for the $-CD_3$ is immediately apparent and the singular peaks of the rigid lattice aromatic deuterons' powder pattern are seen with $\omega_Q \approx 130$ kHz. In Figure 16 is shown the powder pattern from rotational echo FT of a mixture of per-d-hmb and per-d-p-dimethylterephthalate, $D_3CO_2C\phi D_4CO_2CD_3$, with $\omega_r/2\pi \approx 1.43$ kHz. The lineshapes showed non-linear phase errors which were not completely corrected due to an apparent time or phase shift between the two quadrature detection channels and some improvement can be made in this regard, however, this technological problem was not pursued. The low S/N obtained for the rigid lattice $-\phi D_4$ deuterons is due partly to the strength of the single rf pulse used and is described in the next section along with other sensitivity considerations.

As discussed in Chapter I, the effect of magic angle spinning is to reduce or scale the anisotropic lineshape by approximately $\frac{1}{2}(3\cos^2\beta''-1)$. When $\mathcal{H}_Q$ dominates $\mathcal{H}_{int}$, the Fourier transform of the synchronously sampled "isotropic" fid should resemble the lineshapes of Figures 2, 15, 16 until β'' is very close to the magic value. This is illustrated in Figure 17, the isotropic spectra of per-d-hmb for a series of spinner axis settings ranging from very close to magic (top left) to some 0.9° from magic (bottom right). The completely narrowed resonance (top left) shows no singular features since the second order quadrupole broadening is negligible for hmb; $0.0268\ \omega_Q^2/2\pi\omega_0 < 1$ Hz. The off magic spectra can be used to measure an unknown ω_Q. An internal standard can be mixed with the sample or knowledge of ω_Q for any one of the resolved powder patterns in the off magic spectra can be used for calibration. In

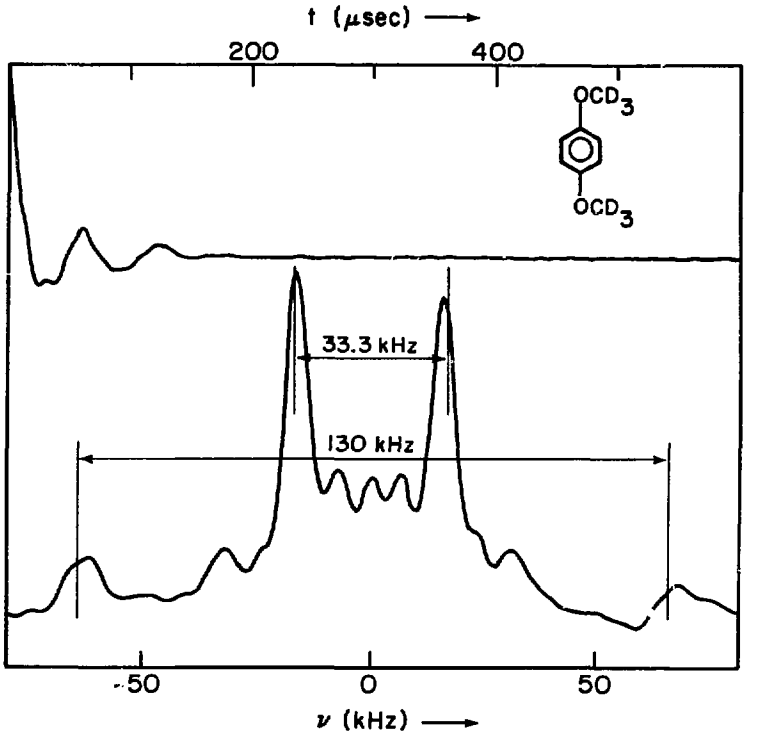

XBL 787-9797

Figure 15

Rotational echo decay and corresponding Fourier transform showing overlapping deuterium quadrupole powder patterns for per-deuterated p-dimethoxybenzene with magic angle rotation at 1.24 kHz.

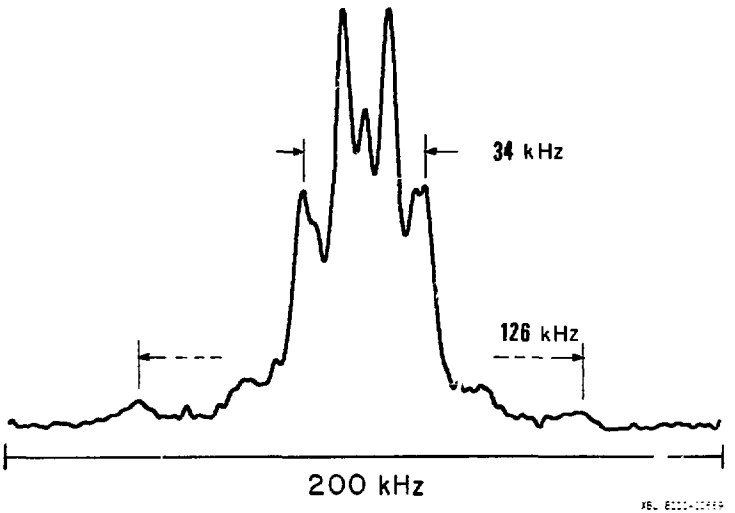

Figure 16

Deuterium quadrupole powder pattern spectrum for a mixture of per-deuterated hexamethylbenzene and per-deuterated p-dimethylterephthalate. Spectrum obtained from Fourier transformation of the rotational echo decay with magic angle rotation at 1.43 kHz.

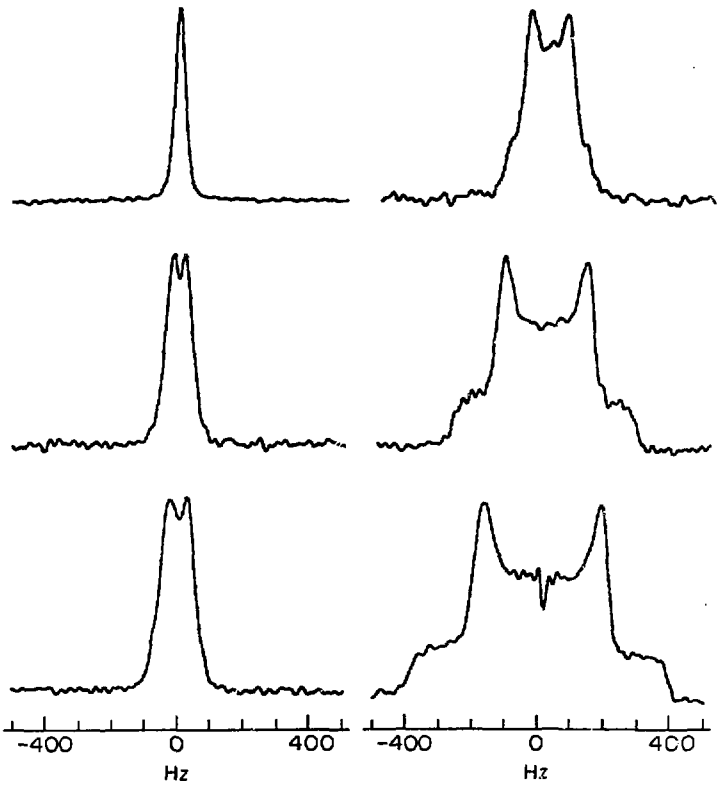

Figure 17

Isotropic spectra of per-deuterated hexamethylbenzene for a series of spinner axis settings ranging from the magic angle (top left) to some 0.9^{o} from magic (bottom right). The anisotropic lineshape is preserved and scaled down by near magic angle rotation.

Figure 18 the isotropic spectra of 93%-deutro-lauric acid are shown for a series of spinner axis settings. The presence of some ^2H_2O in the sample gives the peak at the center. Previous measurement of the $-CD_3$ $\omega_Q' = 36$ kHz shows that the methylene quadrupole couplings range from 102-120 kHz.

Quadrupole couplings measured by the methods described above are listed in Table III. Measurement of resonance shifts in the exact magic angle isotropic spectra gives an additional method to obtain ω_Q since part of the shift is due to the quadrupole coupling and this is described in a later section. All values were taken as the splitting between the singular peaks of the powder pattern which is smaller than the true value when $\eta \neq 0$, however, from previous work the asymmetry in all the compounds of Table III should be less than 10% (37). Some small significant differences were found between spinning and non-spinning values, but were not accounted for since some technical problems existed. The rotational echo Fourier transform is actually the envelope of the sideband spectrum (12) and a difference of about one kiloHertz between spinning and non-spinning values could probably be attributed to the finite rotation frequency. Other methods have been developed to retrieve the anisotropy, ω_Q, from the spinning sample experiment, but as long as $\omega_r << \omega_Q$ the spinning methods above are simple and accurate to within a few percent. As pointed out by Waugh et al. (43) the overlapping powder patterns in the rotational echo Fourier transform may be obtained selectively, i.e., individually, when their corresponding sharp isotropic resonances are resolved in the near magic angle spectrum.

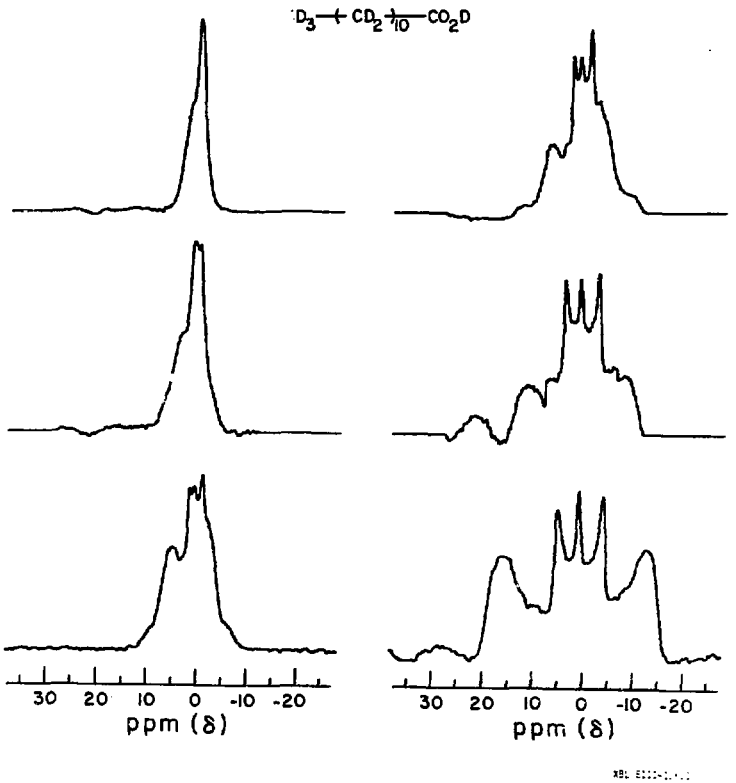

Figure 18

Near magic angle isotropic spectra for 93% deuterated lauric acid powder. Overlapping powder patterns of methyl and methylene deuterons are evident allowing measurement of their quadrupole couplings.

TABLE III: Deuterium solid state quadrupole couplings, ω_Q(kHz)

Compound	Position	Method: Pulsed echo	Method: Rotational echo	Method: Isotropic spectrum
hexamethylbenzene[1]	—	15.8±0.2	14.4±0.5	
25%-d-hexamethylbenzene[2]	—	13.7±0.		
p-dimethylterephthalate[1] $D_3CO_2C\phi D_4CO_2CD_3$	methyl aromatic	37.8±0.5	34±1 126±5	
monomethyl succinate DOOCCHDCHDCOOCD$_3$	methyl	34±1		
p-dimethoxybenzene[1] $D_3CO\phi D_4OCD_3$	methyl aromatic	33.2±0.5	32±1 130±3	
p-dimethoxybenzene[3]	aromatic			125±4
p-diethylterephthalate[1] $D_3CD_2CO_2C\phi D_4CO_2CD_2CD_3$	methyl methylene aromatic	35.0±0.5 113±3 133±4	34±1 111±6 130±6	(115±8)[6]
4,4'-dimethylbenzophenone[1] $D_3CD_4\phi CO\phi D_4CD_3$	methyl aromatic	(35)[4]		142±12; (142±12)[6]
lauric acid[1] $CD_3(CD_2)_{10}COOD$	methyl methylene	36±1 (125)[5]		102-120

1. per-deuterated (>90% gram-atom ^2H).
2. randomly deuterated, most probable type $-CH_2D$.
3. 44% randomly deuterated in methyl position, 66% randomly deuterated in aromatic position.
4. assumed value for calibration of isotropic spectrum.
5. uncertain due to lineshape distortion.
6. determined from field dependence of resonance shifts.

C. Sensitivity Considerations

1. Strength of Irradiation Pulse

In all the deuterium experiments a general consideration for sensitivity is the strength of rf pulse used. In a well-known argument, a short irradiation pulse of width τ_p is thought to "cover" or excite over a bandwidth of π/τ_p, its Fourier transform being a sinc τ_p function. In the experiments here, the effect of pulse strength and width must be calculated using well-known density matrix methods. The operator formalisms developed by Vega and Pines (17), Vega (44), and Wokaun and Ernst (45), have had great use in recent years in describing the preparation, evolution, and detection of phase coherent properties of the magnetization for spin systems $I > \frac{1}{2}$. In this section their formalism is applied to calculate the single quantum deuterium signal after a single pulse.

During irradiation the deuterium spin experiences an effective field in the rotating frame due to the rf field, strength ω_1 along the x-axis, and a "quadrupole" field, strength ω_Q along the z-axis. In the basis of Vega and Pines the rotating frame Hamiltonian is

$$\mathcal{H} = -\Delta\omega I_z + \omega_1 I_x + \frac{1}{6}\Omega_Q(3I_z^2 - I^2)$$

$$= -2\Delta\omega I_{z,1} - 2\omega_1 I_{x,1} + \frac{1}{3}\Omega_Q(I_{x,3} - I_{y,3}). \qquad \text{(III-1)}$$

The directly observable single quantum signal after a pulse of length t is given by the coefficient of $I_{y,1} = \frac{1}{2}I_y$ in the density matrix $\rho(t)$ and from Table IV of Reference 17 the result for $\Delta\omega = 0$ is

$$a_{y,1}(t) = \cos(\theta/2)\sin^2\theta/2)\{\sin[\tfrac{1}{2}(\omega_e + \Omega_Q/2)t]$$

$$+ \sin[\tfrac{1}{2}(\omega_e - \Omega_Q/2)t]\} \qquad \text{(III-2)}$$

where

$$\omega_e = [4\omega_1^2 + (\tfrac{1}{2})\Omega_Q^2]^{\frac{1}{2}}$$

$$\theta = \text{Arctan}(4\omega_1/\Omega_Q). \qquad \text{(III-3)}$$

The intensity of single quantum resonances in the isotropic magic angle spectra is given by Equation III-2 summed and weighted over all Ω_Q due to the orientations of the crystallites of the powder and the result is shown in Figure 19. It is assumed that the length of the pulse, $t_p << 2\pi/\omega_r$, so that the Ω_Q are time independent during the pulse. The maximum value of $a_{y,1}$ (powder sum) = $\langle M_y \rangle_m$ attainable when the pulse is not strong is plotted for various relative strengths, ω_1/ω_Q. The length of pulse, t_p, for which the $\langle M_y \rangle_m$ is obtained is also shown in the lower curve. In most experiments $\omega_1 \sim 40$ to 60 kHz so that for a methyl group with $\omega_Q' \simeq 35$ kHz the full single quantum intensity could be achieved. However, for rigid lattice positions usually $\omega_Q \sim 130$ kHz and $\langle M_y \rangle_m \simeq 0.75$. Furthermore, when large differences in ω_Q's exist in the sample, $\langle M_y \rangle$ cannot always be maximized for all components with a single pulse. The nutation of the powder sum single quantum coherence which is the intensity, $\langle M_y \rangle$, observed in the isotropic magic angle spectra is plotted in Figure 20 for pulses of constant ω_1 and increasing length t. The solid curves are the theoretical result obtained above and the dotted curves are experimental data in arbitrary units for comparison with the solid curves.

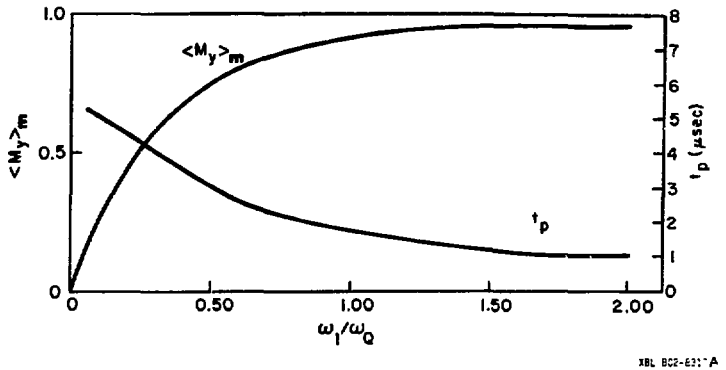

XBL 802-631 A

Figure 19

Maximum single quantum intensity, $\langle M_y \rangle_m$, available in the isotropic magic angle deuterium spectrum after a single, weak radiofrequency pulse of strength ω_1. The length of pulse for which the maximum is observed is plotted as t_p.

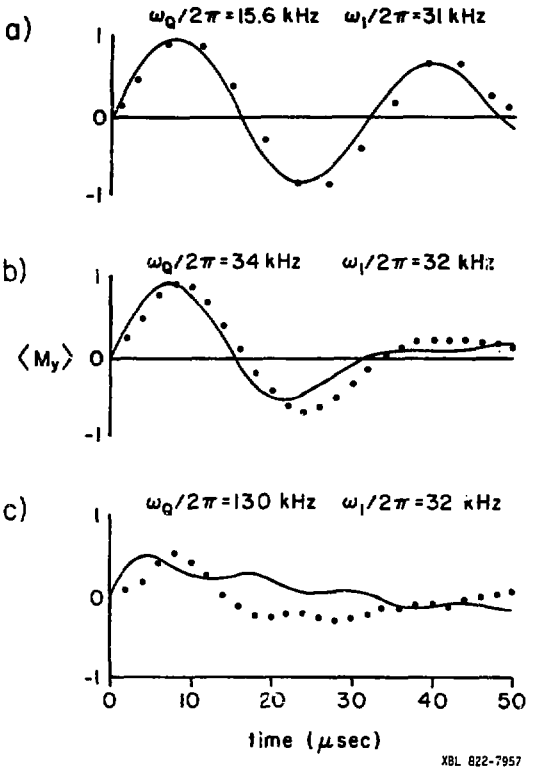

Figure 20

Nutation of the powder sum single quantum coherence which is the intensity, $\langle M_y \rangle$, observed in the isotropic spectrum plotted for pulses of constant ω_1 and increasing length, t. The solid curves are the theoretical result and the dotted curves are the experimental values.

Figure 20a shows the results for per-d-hmb for which the pulses are strong over the entire static powder spectrum. Figure 20b shows the results for the $-CD_3$ resonance of per-deutero-para-dimethoxybenzene, $CD_3O\phi D_4OCD_3$ (per-d-p-dmb), and Figure 20c showd the results for the aromatic peak of per-d-p-dmb.

The results illustrated in Figure 20 show an inhomogeneous dephasing of the magnetizations of the crystallites of the powder in the rotating frame and the resulting decrease in $\langle M_y \rangle$ for longer pulses. This result suggests that the use of "composite pulses" may be useful (46). Differences between theory and experiment are largely due to non-ideality of the pulse shape which is more critical for larger ω_Q and shorter pulses. An interesting point is that when partially unresolved resonances have very different ω_Q's, then ω_1 and t_p can be adjusted so that one peak appears in absorption phase ($\langle M_y \rangle$ positive) while the other is in emission ($\langle M_y \rangle$ negative).

The effect of insufficient pulse strength is a distortion of intensity which was seen in Figure 14 (top) in the distorted powder pattern of ferrocene. Wemmer et al. (47) have recently demonstrated a new method for non-spinning samples using relatively long, weak, amplitude modulated pulses to give Multiple Frequency Excitation and piece together the powder pattern for large ω_Q with no intensity distortion.

2. Synchronous Sampling

To compare the relative sensitivities of the spinning and non-spinning experiments it is useful to review the case of narrowing the chemical shift powder spectra (see Fig. 1) by magic angle spinning (12). As the sample is rotated slowly the pattern is broken up into sidebands

(see Fig. 14) of which there are roughly $\Delta\sigma/\omega_r$, the total non-spinning anisotropic linewidth divided by ω_r. Sampling the fid at a rate of $\omega_r/2\pi$ adds all the sidebands together, but the spectrometer audio filters must have a pass bandwidth of $(\frac{1}{2})\Delta\sigma$ (for quadrature detection) to do so. The accumulation of noise degrades the S/N ratio by about $(\Delta\sigma/\omega_r)^{\frac{1}{2}}$ from the fast spinning case where all the intensity is in the isotropic centerpeak. Conversely, the pass bandwidth may be reduced to $2\pi/\omega_r$ and the tallest sideband observed which has only a fraction of the total intensity. The true resonance frequency is deduced by changing ω_r by $\delta\omega$, which shifts the n^{th} sideband by $n\delta\omega$. In either case there is no need to sample at a rate faster than $\omega_r/2\pi$ to obtain the "isotropic" spectrum. As ω_r increases, the number of sidebands decreases and the isotropic peak intensity increases until $\Delta\sigma \approx \omega_r$, when almost all of the intensity has gone into the isotropic peak. In practice, as ω_r increases the pass bandwidth can be reduced also since the sidebands in the wings are generally smaller. Therefore increasing ω_r maximizes sensitivity by putting more intensity into the isotropic peak and allowing reduction of the pass bandwidth. In practice, the rotation frequency (observed spectral window) cannot always cover the range of isotropic chemical shifts, e.g., ^{13}C at $\omega_0 \gtrsim 18$ MHz, and the complexity of spectra can limit the usefulness of synchronous sampling. An alternative approach, which requires strong pulses, is to digitize the entire sideband spectrum and selectively eliminate sidebands of all orders n except one (48).

For deuterium spinning experiments, $\omega_r \ll \omega_Q$; the rotation frequency is always in the very slow spinning regime. Fortuitously, an observation window of $\omega_r/2\pi$ will always cover the range of ^2H (or ^1H) isotropic

chemical shifts. The pass bandwidth is always set to the largest ω_Q of the sample, typically ~130 kHz, and as above the signal to noise increases as $\omega_r^{\frac{1}{2}}$. With increasing magnetic field strength the full factor $(\Delta B_0)^{3/2}$ gain in signal to noise is realized since ω_Q does not change. In the chemical shift case, $\Delta\sigma$ increases linearly with magnetic field and in the slow spinning regime a reduced gain of factor (ΔB_0) is realized with increasing field, all other factors being equal.

3. Sensitivity in Measurement of ω_Q

Following the discussion of pulse strength effects in paragraph 3a, the recovery of magnetization or height of the rotational echo is generally better than for the pulsed quadrupolar echo since the latter requires two pulses which are usually far from ideal. Furthermore, when the ^2H is not dilute, the height of the pulsed echo decays according to T_2 due to the static homonuclear dipole coupling which is much shorter than that for the magic angle rotating sample. A factor of ten savings in time was not uncommon for the rotational echo over the pulsed echo method. The comparable S/N of the off magic isotropic spectra was slightly better than the rotational echo Fourier transform. The spectra of Figures 17 and 18 were obtained in several minutes. A useful feature of the isotropic spectra is that the lineshapes were usually closer to the theoretical shape for large ω_Q than the echo Fourier transforms.

D. High Resolution Results

1. Sample Spinner Stability

The isotropic chemical shift spectrum of per-deutero-para-dimethylterephthalate powder, per-d-p-dmt, rotating at 3.53 kHz about

approximately the magic angle is shown in Figure 21. This result was obtained with the conical spinner system described in Chapter II. The taller peak is assigned to the methyl groups, with the zero of the scale arbitrarily set to that peak, and its full width at half maximum (FWHM) is 3.2 ppm. The downfield peak due to the aromatic deuterons ($-\phi D_4$) is not resolved. The isotropic spectrum of per-deutero-para-diethylterephthalate ($\omega_r/2 = 3.33$ kHz), per-d-p-det, is shown in Figure 22. The resonances are assigned as shown and the methyl FWHM is 1.6 ppm. The instability of the axis of the conical spinner makes it difficult to remove the quadrupolar broadening even in first order. In fact, the fid varied significantly from shot to shot and in Figure 23 is shown the spectrum of per-d-p-det obtained by visually selecting fid's with long decays for the average. Clearly, rotor instability was the major factor limiting resolution.

The isotropic spectrum of per-d-p-dmt taken with the cylindrical spinner described in Chapter II is shown in Figure 24, $\omega_r/2\pi = 1248 \pm 4$ Hz. A narrowing of lines is evident and a splitting of 1.3 ppm in the aromatic peak appeared which is attributed to the inequivalence in the solid state of the 2,5 and 3,6 ring positions. Linewidths and limits of resolution are discussed in a following paragraph. The cylindrical rotor provides the long time stability necessary for complete removal of the first order quadrupole broadening of deuterium in solids. It can be made large in size for its relative stability and the coil filling factor approaches that of the usual stationary sample NMR. These characteristics provide good relative sensitivity and allow signal averaging to be used which brings the technique into the regime of high resolution work (29,49).

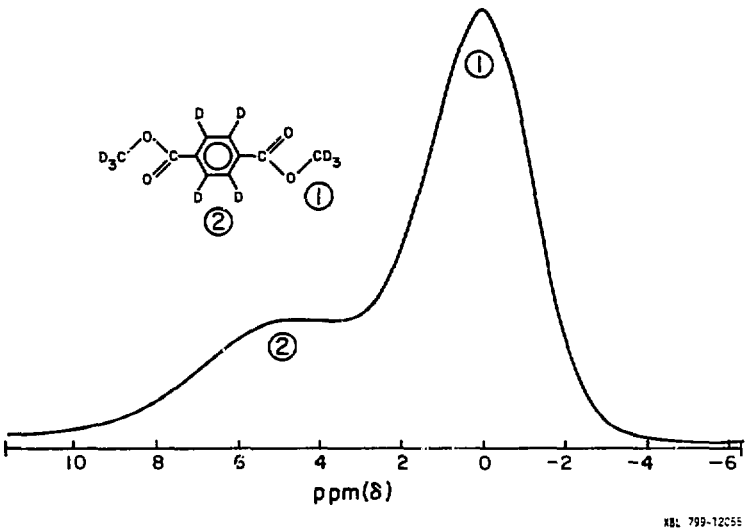

Figure 21

Isotropic chemical shift spectrum of polycrystalline perdeuterated p-dimethylterephthalate rotating at 3.53 kHz, taken with conical spinner. Resonances from methyl and aromatic deuterons were not resolved due to rotor instability.

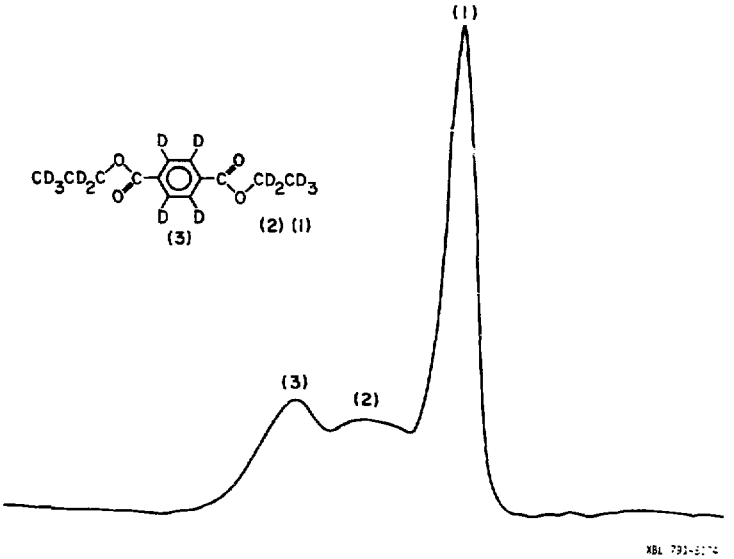

Figure 22

Isotropic deuterium spectrum of per-deuterated p-diethylterephthalate rotated at 3.33 kHz. Resonances are unresolved due to instability of conical sample rotor.

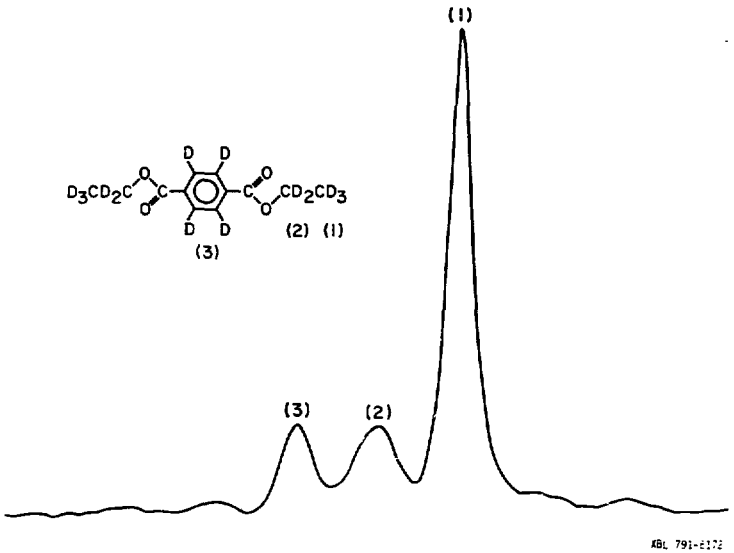

Figure 23

Isotropic deuterium spectrum of per-deuterated p-diethylterephthalate produced by visually selecting scans with long decays for the signal average. Selection compensates for rotor instability and indicates that the conical rotor stability is insufficient for high resolution.

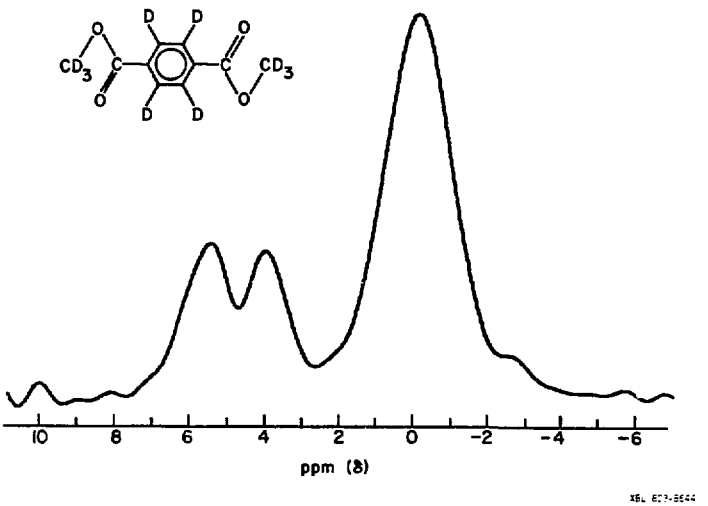

Figure 24

Isotropic chemical shift spectrum of polycrystalline perdeuterated p-dimethylterephthalate rotating at 1.25 kHz, taken with cylindrical-gas bearing type spinner. Downfield aromatic doublet is resolved from methyl resonance. Splitting of 1.3 ppm occurs in aromatic peak due to inequivalence of 2,5 and 3,6 ring positions in the solid state.

2. Chemical and Quadrupole Shifts

a. Magnetic Field Dependence

As discussed in Chapter I, Equation I-37 and Figure 7, the residual quadrupole coupling not removed by magic angle rotation contributes both to the linewidth and shift in the isotropic spectra. The dependence of resonance shift on B_0 is illustrated in Figure 25 by the isotropic spectra of para-dimethoxybenzene at three field strengths (50). The zero of all scales was set arbitrarily to the methyl peak in the highest field spectrum and the absolute frequency scale is given at the bottom. The aromatic region shows a doublet due to inequivalence in the solid of the 2,5 and 3,6 ring positions. The molecule is locked in the rigid lattice in the anti-conformation. The resonance shift is the sum of the downfield quadrupolar shift, Δ, and the isotropic chemical shift, σ. The complete powder pattern shape shown in Figure 7b was at no time observed since it was never much larger than other factors contributing to the linewidth. The isotropic peaks are roughly triangular in shape at their narrowest and Δ was taken theoretically as the midpoint between the singular peaks in Figure 7b. The variation in linewidths in Figure 25 is discussed in a later paragraph.

Only a slight shift Δ is observed for the methyl peak since it has a smaller $\omega_Q'/2\pi$ = 33 kHz. The shift of the aromatic region is dramatic since it has $\omega_Q/2\pi$ = 130 kHz. At low field $\Delta(\phi d_4)$ is large and it decreases linearly as B_0 increases. On the other hand, σ increases linearly as B_0 increases. At about $\omega_0/2\pi$ = 31 MHz the aromatic doublet begins to move back downfield as $\Delta < \sigma$.

To compare deuterium solid state chemical shifts with liquid state σ's or with proton chemical shifts it is useful to separate Δ and σ.

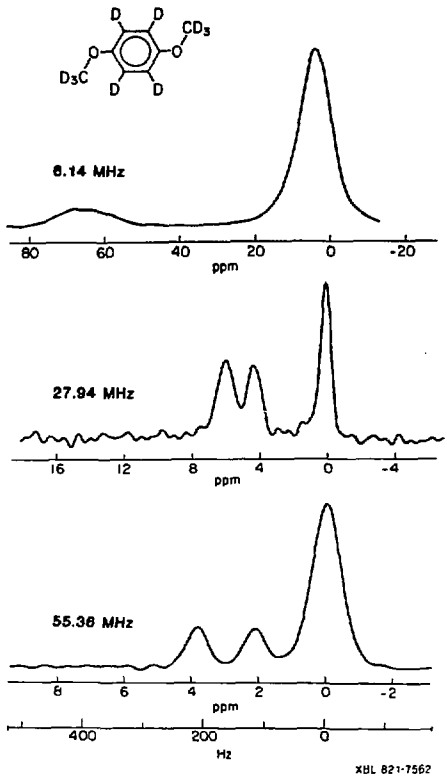

Figure 25

Magnetic field dependence of solid state deuterium chemical and quadrupole shifts. The second order quadrupole downfield shift goes as $1/B_0$ while the chemical shift is proportional to B_0.

The results for para-dimethoxybenzene and the theoretical values are summarized in Table IV. The shift between the center of the aromatic doublet and the methyl peak is labeled δ and is given by

$$\delta = B_0\sigma + B_0^{-1}[\Delta(-\phi D_4) - \Delta(-CD_3)]$$

$$= \sigma' + \Delta'. \qquad \text{(III-4)}$$

Values of σ', Δ' given were obtained from the data at the two higher fields in Equation III-4. Comparison of Δ' with the theoretical values indicates that the spinner axis was within 0.003° of magic. These results verify that measurement of ω_Q can be used to extract σ for comparison with liquid or proton σ's. The small lineshifts and broadening observed for fine adjustments of the spinner axis verify the mechanical estimate that a minimum adjustment of less than 0.003° was possible. It is interesting to note that such tiny adjustments can easily be made with that simple arrangement while more elaborate mechanisms could certainly be devised.

b. Isotropic Chemical Shifts

The results of the previous paragraphs demonstrate the measurement of high resolution parameters of deuterium in solids. Deuterium isotropic chemical shifts extracted from magic angle spectra are compared with corresponding liquid state values in Table V. The uncertainties are ±0.1 ppm for liquid state values and ±0.2 ppm for solid state values. There are small significant differences between liquid and solid values in many cases. All measurements were made using an internal standard; hexamethylbenzene powder mixed with the unknown. It is interesting to note that in some cases, e.g., organic molecular

TABLE IV: Deuterium solid state chemical and quadrupole shifts for para-dimethoxybenzene. Shifts in Hz (ppm).

$\omega_0/2\pi$ (MHz)	OBSERVED[1] SHIFT	EXPERIMENTAL[2] σ'	EXPERIMENTAL[2] Δ'	THEORETICAL[3] β_m	THEORETICAL[3] Δ' $\beta_m-0.003^o$	THEORETICAL[3] Δ' $\beta_m-0.006$
6.14	377±16 (61)	14±1 (2.3)	363±10 (59)	339±14 (55)	345±14 (56)	351±14 (57)
27.94	143±2 (5.1)	64±2 (2.3)	79±2 (2.8)	75±3 (2.7)	81±3 (2.9)	86±3 (3.1)
55.36	166±4 (3.0)	126±4 (2.3)	40±1 (0.72)	38±2 (0.69)	44±2 (0.79)	49±2 (0.88)

1. Shift between center of aromatic doublet and methyl peak.
2. From Eq. III-4 and data at 27.94, 55.36 MHz.
3. See Appendix C.

TABLE V: Deuterium liquid and solid state isotropic chemical shifts, σ. Values in ppm (δ) vs. per-deutero-hexamethylbenzene internal standard.

Compound	Position	Liquid	Solid
ferrocene	——	1.9*	2.2
p-dimethylterephthalate $D_3CO_2C\phi D_4CO_2CD_3$	methyl	1.8	2.2
	aromatic	5.9	3.8 5.1
p-dimethoxybenzene $D_3CO\phi D_4OCD_3$	methyl	1.5	1.4
	aromatic	4.6	2.8 4.5
p-diethylterephthalate $D_3CD_2CO_2C\phi D_4CO_2CD_2CD_3$	methyl methylene	-0.8 2.2	-0.2 2.1
	aromatic	5.9	5.4 5.8

* Proton σ vs. protonated hexamethylbenzene.

solids, the mixing of powders caused a lowering of melting points and some mixtures quickly liquified. To avoid this problem an internal standard can always be sealed in a small container placed in the unknown powder, but this is a less desirable method.

There is no reason to assume that the hexamethylbenzene shift is the same in solid and liquid states, but no general shift of resonances was observed using it as the standard. Differences between solid and liquid values were both upfield and downfield. Small differences in liquid and solid state shifts are not surprising due to the vast differences in molecular environment and conformation in the two states and the fact that the deuterons (or protons) are generally located on the periphery of molecular structures and should be most susceptible to those differences. For instance, solvent effects in the high resolution NMR of solutions are replaced by the effects of crystal packing and point group symmetry in crystals.

The most striking feature of the data in Table V is the effect of rigid lattice molecular conformation which leads to a doublet in the aromatic resonances of the para-di-substituted benzenes. This "solid state" effect has also been observed in the ^{13}C spectra of some of these and other solids (12,13), however, as a fraction of the total range of isotropic shifts this effect is much larger for ^{2}H (or ^{1}H) due to their peripheral location. The subjects of $^{1}H/^{2}H$ isotope effects and the ring current theory will be discussed in Chapter IV.

The ability to obtain deuterium (or proton) high resolution isotropic spectra provides a useful tool for the study of the solid state, especially since the results demonstrated above are applicable to e.g., amorphous, glassy, or plastic crystalline solids and, of course, polycrystalline

solids which eliminates any need to produce single crystals. Several further examples will be presented in the next section. These results offer the possibility to gain direct information on a variety of phenomena of interest to physical chemists, e.g., phase transitions, ferroelectric and paraelectric materials, interactions with surfaces (adsorption, chemisorption, catalysis), hydrogen bonding, and solid state reactions. The isotropic solid state spectra sacrifice the information on chemical shift anisotropy in order to gain resolution and make use of the resonance shifts in empirical structure determination. General theoretical calculation of chemical shifts has been a difficult task with uncertain results. More recently, the isotropic shift has become an all important tool as a spreading parameter of resonances in two-dimensional spectroscopy in both solids and liquids.

The isotropic and quadrupole shift data at the two high magnetic fields used to determine the σ's for per-d-p-det is summarized in Table VI. Also shown is the two field data for per-d-4,4'-dimethylbenzophenone, per-d-4,4'-dmbp, used to estimate ω_Q as well as extract σ. Since the Δ for the methyl position in these two compounds are very similar, the $\Delta' = 0.78$ ppm for the aromatic position in per-d-4,4'-dmbp can be simply related to the $\Delta' = 0.68$ for per-d-p-det with Equation III-4 and the dependence $\Delta \propto \omega_Q^2$. The result is ω_Q(4,4'-dmbp) = 142 kHz as shown in Table III.

3. Spectral Resolution

a. Contributions to the Linewidth

A number of factors contribute to the linewidth in the isotropic deuterium spectra and in this section those factors most

TABLE VI: Deuterium solid state chemical and quadrupole shifts in Hz(ppm)

Compound (position)[1] (per-deuterated)	OBSERVED[2] SHIFT	EXPERIMENTAL σ'	Δ'
$\omega_0/2\pi$ = 27.94 MHz			
4,4'-dmbp (aromatic)	207(7.4)	122(4.5)	85(3.0)
p-det (methylene)	120(4.3)	65(2.3)	55(2.0)
p-det (aromatic)	236(8.5)	161(5.8)	75(2.7)
$\omega_0/2\pi$ = 55.35			
4,4'-dmbp (aromatic)	285(5.2)	242(4.5)	43(0.78)
p-det (methylene)	156(2.8)	128(2.3)	28(0.50)
p-det (aromatic)	357(6.5)	319(5.8)	38(0.68)

1. dmbp = dimethylbenzophenone; det = diethylterephthalate.
2. Shift between center of resonance and methyl peak for p-det; shift between upfield aromatic peak and center of methyl resonance for 4,4'-dmbp.

appropriate to crystalline organic molecular solids will be enumerated. Comparison with experimental results is given in the following sections. Other factors of importance for non-crystalline and conducting solids as well as those given here have been discussed in detail previously in regard to spin ½ nuclei in solids (51,52). In the paragraphs below it is assumed that the contribution from laboratory magnetic field inhomogeneity can be eliminated or simply measured in a liquid sample and taken into account. Also, the spin-lattice relaxation times for deuterium in the class of solids considered generally gives no more than two Hertz width for methyl groups and a negligible contribution for rigid lattice deuterons where usually $T_1 > 1$ sec. Some exceptions are pointed out below. All of the contributions listed below are affected to a greater or lesser degree by the stability and axis adjustment of the sample turbine, however, only the residual ^2H quadrupole terms are significant in this respect since they dominate the internal Hamiltonian. The absolute frequency of rotation is generally irrelevant since it always exceeds the frequency width of the non-spinning homogeneous interactions; i.e., homonuclear dipole and second order quadrupole interactions.

The stability of the frequency of rotation while averaging the synchronously sampled fid's is crucial since it determines the time base of the fid's. Since the scans are added digitally and point by point, a drift of the spinner frequency, $\delta\omega_r$, gives a broadening of approximately $f\Delta\omega\delta\omega_r/\omega_r$ where the fraction f takes into account the distribution about a mean of ω_r's from scan to scan and $\Delta\omega$ is the resonance offset. The data presented in this section were obtained with $\Delta\omega$ and $\delta\omega_r$ minimized so that this contribution to the linewidth was negligible.

i) Bulk diamagnetic susceptibility

Crystallites of a powder sample often have an anisotropic susceptibility and voids in the powder may also appear as anisotropic susceptibilities. For a powder, magic angle rotation should usually remove the broadening due to isotropic susceptibilities, but the broadening due to anisotropic susceptibilities are not completely removed. The residual broadening is proportional to B_0 (51-55).

ii) Homonuclear dipole couplings

The residual deuterium homonuclear dipole coupling under magic angle rotation was examined in Chapter ID4. The residual broadening does not depend on ω_r as mentioned above, or B_0.

iii) Residual quadrupole effects

From the results of the previous sections it is concluded that the first order quadrupole interaction may be made smaller than the second order term, $\overline{\omega_Q^2}/\omega_0$. At high laboratory magnetic field the latter is reduced to a very few Hertz for all but the largest ω_Q's.

Heteronuclear dipole couplings can be efficiently removed by the combination of magic angle rotation and rf decoupling in most cases. A dispersion of the isotropic chemical shift which results in a marked linebroadening in amorphous solids appears to be negligible in crystalline solids. The isotropic ^2H-^1H J coupling is on the order of 1-2 Hz and may contribute to linewidths in partially deuterated samples. Isotropic ^2H-^{13}C J couplings, which can be some 25 Hz, are not observed since the ^{13}C is naturally dilute.

b. Results for p-dimethoxybenzene

Experimental resonance linewidths for p-dimethoxybenzene in a variety of deuceration schemes are shown in Table VII. The uncertainty in methyl resonance widths is ±1 Hz and for aromatic resonance widths is ±3 Hz. Some of the corresponding spectra are shown in Figure 26. Differences in integrated intensities in Figure 26 are due to the strength of pulse and the use of cross polarization, the latter to be described in a later section.

In order to isolate the various contributions to the linewidth two methods were used. First, the generally unknown susceptibility contribution was determined by independently measuring the other contributions and subtracting from the measured width. The results used were: i) 3-4 Hz magnetic field inhomogeneity, ii) 2 Hz for methyl T_1, iii) 1 Hz for methyl second order quadrupolar contribution (theoretical), iv) 18 Hz for aromatic second order quadrupole at $\omega_0/2\pi$ = 28 MHz (theoretical), and v) 10 Hz for aromatic second order quadrupole at 55 MHz (theoretical). The latter two values allow a slight (0.002°) deviation from the θ_m. The heteronuclear $^1H-{}^2H$ dipole contribution was assumed to be zero and the residual $^2H-{}^2H$ homonuclear dipolar contribution was taken as the difference between deuterations (1) and (2) in Table VII. With these values the susceptibility contribution was determined to be 0.5 ± 0.1 ppm.

The magnetic field dependence of linewidths can be used to extract the susceptibility and second order quadrupole contributions in the same manner as for resonance shifts in Equation III-4 as long as the field independent contributions are known with reasonable precision. Applying this method to the data at 28;55 MHz for deuteration (1) in Table VII gives a susceptibility contribution of 0.4 ppm and a second order

TABLE VII: Deuterium isotropic resonance linewidths for p-dimethoxybenzene (Hz)

	Deuteration	Position	Linewidth $\omega_0/2\pi$ (MHz) 6.14	27.94	55.35
1)	> 99%	methyl	58	42	58
	97%	aromatic	109	37	40
2)	2.8% ($-CH_2D$)	methyl		21	
	4.8%	aromatic		33	
3)	44% ($-CD_3$)	methyl		25	
	66%	aromatic		33	
4)	98% ($-CH_2D$)	methyl		35	
	66%	aromatic		38	
5)	negligible	methyl		—	
	> 95%	aromatic		39	
6)	> 99%	methyl		54	
	negligible	aromatic		—	

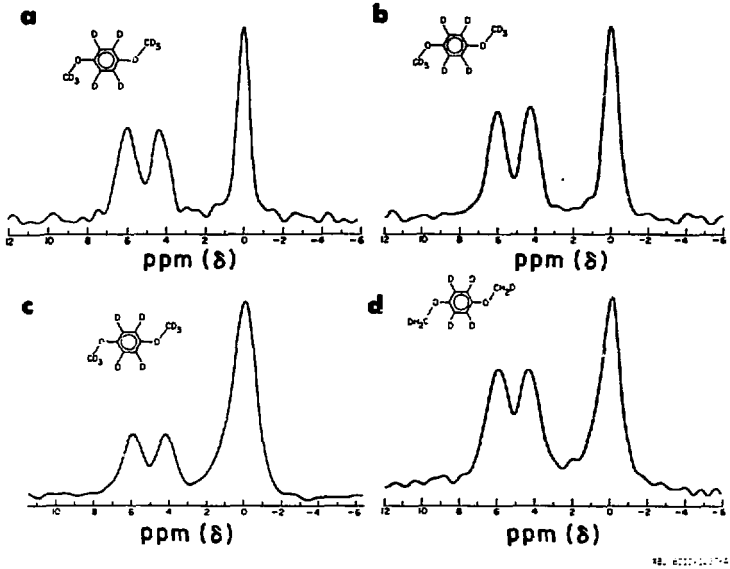

Figure 26

Isotropic deuterium spectra of polycrystalline p-dimethoxybenzene obtained by magic angle rotation with spinning synchronized data acquisition. Level of deuteration (see Table VII): a) 2.8% $-CH_2D$, 4.8% aromatic, b) 44% $-CD_3$, 66% aromatic, c) per-deuterated, d) 98% $-CH_2D$, 66% aromatic.

quadrupole contribution of 18;9 Hz for the two fields respectively. These are in close agreement with the theoretical values cited above.

The heteronuclear $^{1}H-^{2}H$ dipolar contribution is probably not completely removed by decoupling (2,51) which is important for samples (2) through (6) in Table VII. In samples (2) through (4) the decoupling conditions were similar and it is interesting that the resonances in highly deuterated sample (3) are as narrow as those in slightly deuterated (2). The conclusion is that the deuterons need not be extremely dilute to remove their homonuclear dipole couplings. Also, since the resonances of sample (4) were broader than sample (3) it cannot be assumed that nearest neighbor dipole couplings always dominate - the summation over all sites and the effects of molecular reorientation must be considered. Spinner axis adjustment was not optimized for sample (5) because T_1 was being measured at the time and was extremely long. The reason for the larger FWHM of sample (6) is not understood. It is possible that several Hertz broadening, due to ^{1}H which is not removed by ^{1}H decoupling existed and that there was some variation of this amount from sample to sample.

In conclusion, three major contributions to resonance linewidths have been extracted and identified. Since the ability to study solids without special physical preparation or growing of single crystals is quite valuable, the susceptibility broadening presents a major problem in obtaining resolution comparable to that of the NMR of fluids. The deuterium homonuclear dipole coupling can be completely removed when the solid is not fully deuterated. Allowing a few Hertz broadening by $^{1}H-^{2}H$ residual dipole coupling due to off resonance proton decoupling and insufficient decoupling power will reduce the estimated susceptibility

decoupling contribution cited above slightly. The second order quadrupole contribution to the linewidth is negligible at $\omega_0/2\pi$ = 55 MHz for ω_Q < 60 kHz, but gives an important contribution for lower fields or larger quadrupole couplings.

In order to determine the best deuteration scheme for solid state studies, resolution and sensitivity must be considered. The results above indicate that the highest resolution may be obtained when the level of deuteration is up to ½ of all sites and this also reduces the technical requirements for proton decoupling. The question of sensitivity is addressed in a later section with cross polarization results. For the present, the sensitivity attained by application of a single "weak" pulse for synchronous magic angle FT-NMR is indicated by Figure 27, the isotropic spectrum of 0.1 g of per-d-p-dmb obtained from a single scan at $\omega_0/2\pi$ = 55 MHz and $\omega_r/2\pi$ = 5076 Hz exactly.

c. Results for p-diethylterephthalate

Experimental resonance linewidths for p-diethylterephthalate in a variety of deuteration schemes are shown in Table VIII. Some of the corresponding spectra are shown in Figure 28 in which selective isotopic substitution is demonstrated as opposed to random isotopic exchange. Independent contributions cited in the last section were similar with the additional values: i) 13 Hz for methylene second order quadrupole at 28 MHz and ii) 7 Hz methylene second order quadrupole at 55 MHz. The susceptibility contribution was determined to be 0.7 ppm ± 0.2 ppm, however, if 10 Hz contribution is assumed for residual $^1H-{}^2H$ dipole coupling this value is reduced to 0.4 ppm. Precision of data in Table VIII is less than in the previous section and the variation of

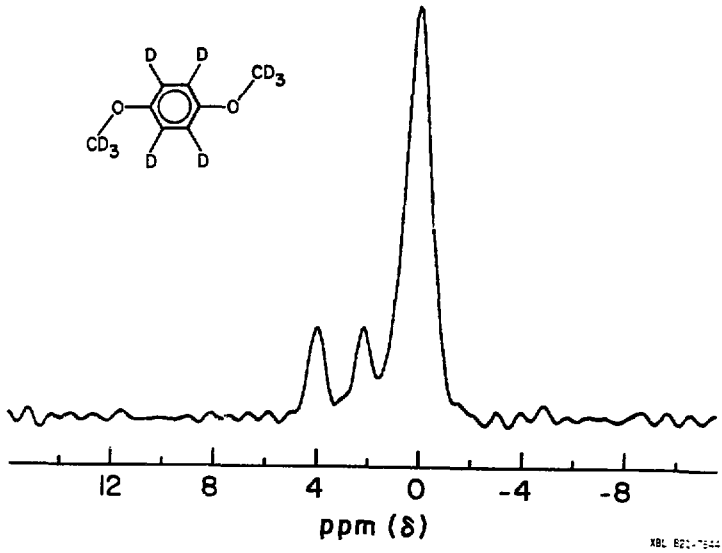

Figure 27

Isotropic deuterium spectrum from a single scan of per-deuterated p-dimethoxybenzene with magic angle rotaation at 5076 Hz. Sample weight was 0.1 gram and $\omega_0/2\pi(^2H)$ = 55 MHz.

TABLE VIII: Deuterium isotropic resonance linewidths for p-diethyterephthalate (Hz).

Deuteration	Position	Linewidth	
		$\omega_0/2\pi$ (MHz)	
		27.94	55.35
1) 98.7%	methyl	31	39
of all sites	methylene	75	106
	aromatic	52	72
2) 2.5%	methyl	20	
5.9%	methylene	33	
9.5%	aromatic	40	
3) 87%	methyl	39	68
negligible	methylene	—	—
> 98%	aromatic	64	86
4) > 95%	methyl	34	
> 95%	methylene	64	
negligible	aromatic	—	

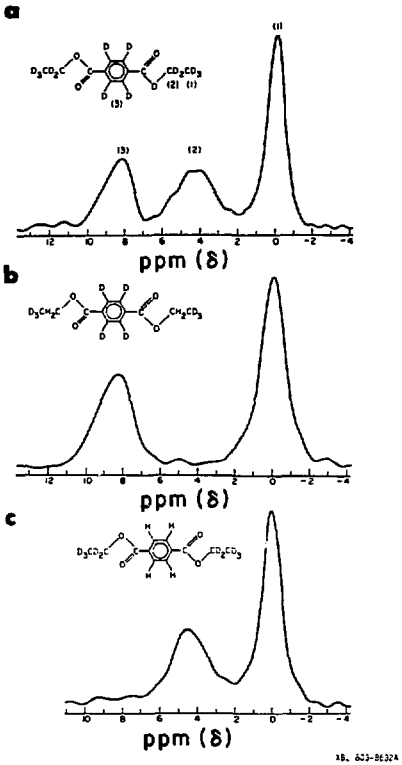

Figure 28

Isotropic deuterium spectra of selectively deuterated p-diethylterephthalate at $\omega_0/2\pi(^2H)$ = 28 MHz. Level of deuteration (see Table VIII): a) per-deuterated, b) per-deuterated except methylene position, c) per-deuterated except aromatic position.

linewidths was not pursued further, however, a residual $^1H-{}^2H$ dipole contribution is certainly indicated. The spectrum of sample (2) is shown in Figure 29. Taking into account the "weak" pulse, the integrated intensities agree with the results of the solution NMR and mass spec analysis within 3%.

d. Further Results

Experimental resonance linewidths for a variety of model deuterated solids are shown in Table IX. Some observations are enumerated below.

i) 4,4'-dimethylbenzophenone

Since the methyl linewidth has a negligible second order quadrupole contribution, the width is the sum of a constant term and the susceptibility term which is linear in B_0. Using the independent contributions cited previously the two field data indicate that the residual $^2H-{}^2H$ homonuclear dipole contribution is negligible and the susceptibility contribution is 0.7 ppm. Estimating the aromatic second order quadrupole contribution from ω_Q in Table III gives a similar result for the aromatic resonances with susceptibility broadening 0.9 ppm. There is no uncertainty in these results due to proton decoupling.

ii) p-dimethylterephthalate

Assuming a homonuclear dipole contribution of 30 Hz from samples (2) and (4), the linewidth for the spinning single crystal (3) is expected to be 37 Hz in the absence of susceptibility broadening. This compares with the observed value of 35 Hz and indicates that no susceptibility broadening is found in a single crystal even of prismatic shape (although a residual resonance shift is possible). The susceptibility contribution is determined to be 0.8 ppm for the powder.

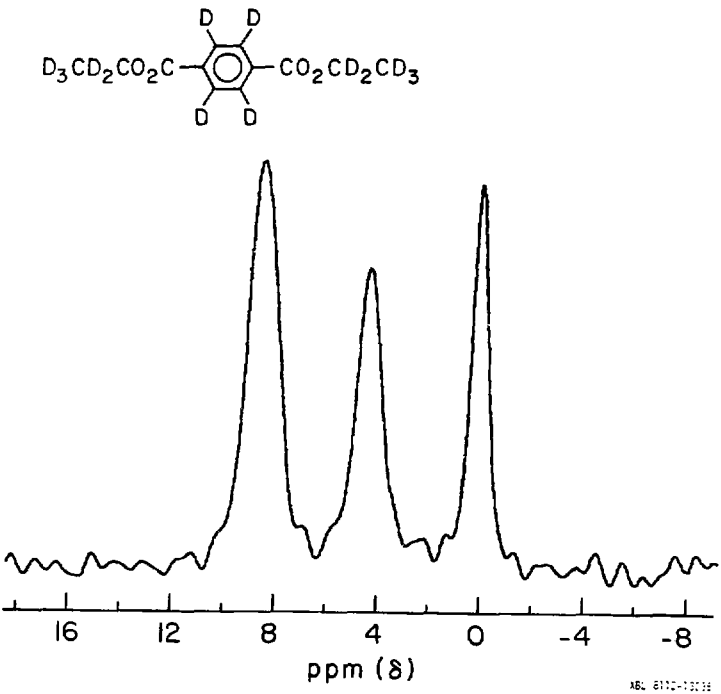

Figure 29

Isotropic deuterium spectrum of p-diethylterephthalate obtained by multiple contact cross polarization with magic angle rotation and spinning synchronized data acquisition at $\omega_0/2\pi(^2H)$ = 28 MHz. Level of deuteration: 2.5% methyl, 5.9% methylene, 9.5% aromatic.

TABLE IX: Deuterium isotropic resonance linewidths (Hz).

Compound	Deuteration/Position		Linewidth $\omega_0/2\pi$ (MHz) 27.94	55.35
1) 4,4'-dmbp[3]	97% of all sites	methyl	24	45
		aromatic	44[1]	62[2]
2) p-dmt[3]	> 99% of all sites	methyl	57	
		aromatic	38	
3) p-dmt single crystal	> 95% of all sites	methyl		35
		aromatic		—
4) p-dmt	2% ($-CH_2D$)	- methyl	27	
	9.5%	- aromatic	—	
5) ferrocene	28%		20	
6) p-dtbb[3]	98.8% of all sites	methyl	61	69
		aromatic	—	—
7) p-dtbb	negligible	- methyl	—	
	98%	- aromatic	49	
8) adamantane	30%			15

1. FWHM of unresolved peaks minus σ difference measured at 55 MHz.
2. Twice the HWHM of upfield peak.
3. dmbp = dimethylbenzophenone.
   dmt = dimethylterephthalate.
   dtbb = di-*t*-butylbenzene.

iii) p-di-t-butylbenzene

The unusually short methyl T_1 = 10 msec, probably due to hindered rotation and the quadrupolar relaxation mechanism, gives a contribution of 32 Hz. The two field data result is 0.2 to 0.3 ppm for susceptibility and 18 Hz for homonuclear dipole broadening. There is no uncertainty in these results due to proton decoupling.

iv) adamantane

The 0.27 ppm width was the narrowest resonance observed.

v) hexamethylbenzene

Linewidths ranging from 35-68 Hz were observed at 28;55 MHz for various level of deuteration, with a susceptibility contribution of 0.8 ppm. The methyl linewidth for ^{13}C at 45 MHz was 1 ppm and Garroway et al. (53) have reported that the susceptibility contribution is 0.7 - 0.9 ppm.

Compressing the sample or dispersing the powder in a medium of similar and isotropic susceptibility can largely reduce the residual broadening due to isotropic susceptibilities (51-55). A part of the contributions cited above may be due to isotropic susceptibilities. Dispersing the hexamethylbenzene and ferrocene in paraffin did not change the observed linewidths, but this test was not conclusive.

e. Resolution

Due to the magnetic field dependence of the quadrupole shifts and susceptibility contribution to the linewidth, the resolution attainable depends on ω_Q and B_0. Holding ω_Q constant and defining resolution as the range of isotropic chemical shifts divided by the

resonance FWHM, the resolution can increase dramatically from $B_0 \approx 1$ Tesla to $B_0 = 8.5$ Tesla as shown for the aromatic resonances in Figure 25. In general, resolution varies according to $\Delta\sigma B_0/(qB_0^{-1} + sB_0)$ where q,s are the second order quadrupole and susceptibility contributions to the linewidth respectively. From 1T to 8.5 T resolution increases by nearly a factor of 20 for large $\omega_Q = 130$ kHz as in Figure 25, but only a further 20% increase could be realized at higher fields.

When there are many ω_Q's for the observed nuclei, resolution varies according to $(\Delta\sigma B_0 + \Delta')/(q_{avg}B_0^{-1} + sB_0)$ where Δ' is the difference in quadrupole shifts defined in Equation III-4. The resolution gain by decrease in quadrupole broadening can be offset by reduction of Δ'. In general, the optimum resolution is attained for higher fields, but little is to be gained above 8.5 T. For larger ω_Q, e.g., ^{14}N, the susceptibility contribution is negligible compared to the quadrupole effects. For instance, holding ω_Q constant the resolution increases as approximately B_0^2. However, selective methods to reduce quadrupole broadening would be useful as mentioned in Chapter I.

Optimum resolution for deuterium at 8.5 T is illustrated in Figure 30, the isotropic spectrum of per-d-p-det. Resonances are assigned as before and the crystallographic inequivalence of aromatic sites is revealed with an 0.4 ppm splitting. In the ^{13}C CP-MAS spectrum of this compound, this inequivalence was found to be 1.1 ppm (56) and for other para-disubstituted benzenes differences in the 2,5 and 3,6 ring carbons of 2-7 ppm have been reported (12,13,51,53,57).

The isotropic spectrum of 4,4'-dimethylbenzophenone at 4.3 T is shown in Figure 31. Optimum resolution at 8.5 T is illustrated in Figure 32. The downfield aromatic resonance shows a splitting attributed to

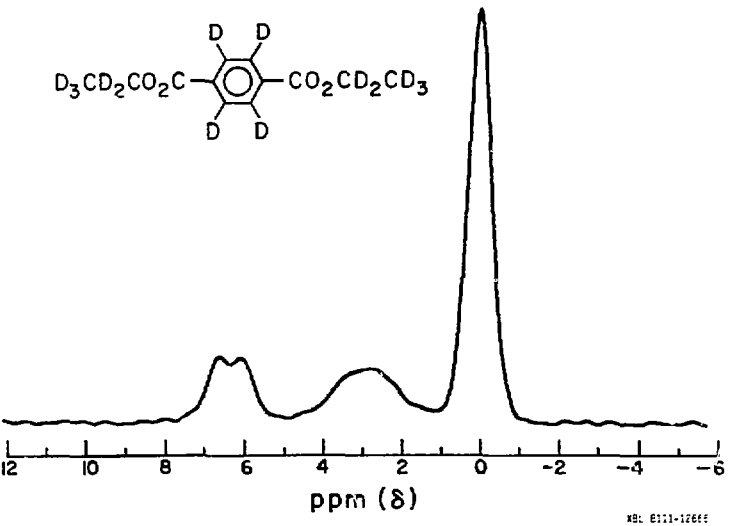

Figure 30

Isotropic deuterium spectrum of per-deuterated p-diethylterephthalate at $\omega_0/2\pi(^2H)$ = 55 MHz. Splitting of 0.4 ppm in aromatic resonance is due to crystallographic inequivalence of 2,5 and 3,6 ring positions.

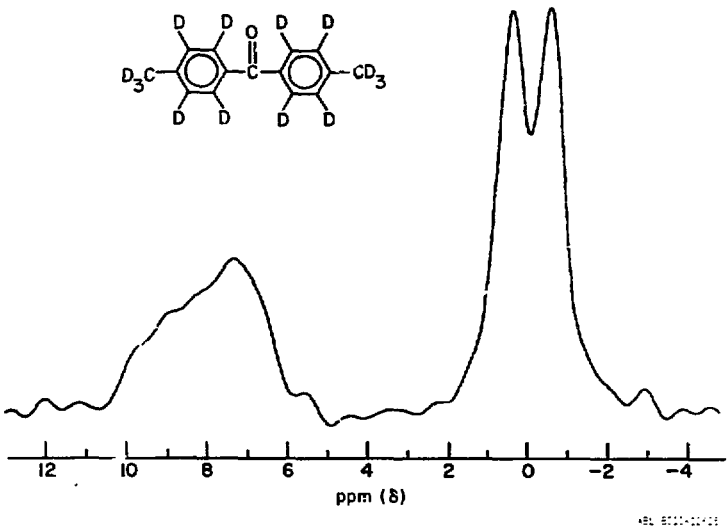

Figure 31

Isotropic deuterium spectrum of per-deuterated 4,4'-dimethylbenzophenone at $\omega_o/2\pi(^2H)$ = 28 MHz. The methyl resonance appears as a doublet indicating that the 4,4' methyls are not magnetically equivalent. The broad aromatic resonance appears to have unresolved structure.

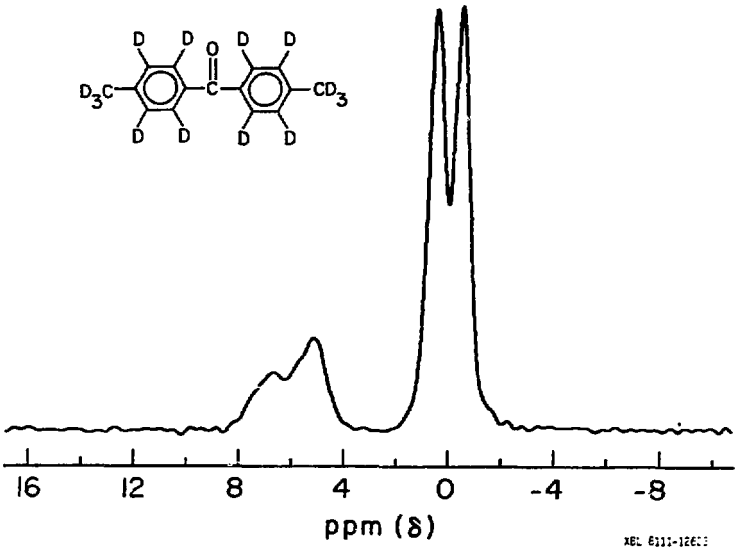

Figure 32

Isotropic deuterium spectrum of per-deuterated 4,4'-dimethylbenzophenone at $\omega_0/2\pi(^2H)$ = 55 MHz. Methyl doublet indicates that the 4,4' methyl groups are not magnetically equivalent. The distribution of aromatic isotropic shifts agrees with a non-planar conformation of the molecules in the crystal.

non-planarity of the molecule in the solid state. Observation of two resonances in the methyl region is an interesting result and will be discussed further in Chapter IV with the isotropic ^{1}H results.

Resolution at 8.5 T is further illustrated in Figure 33, the isotropic spectrum of *per-d-para-di-t-butylbenzene* for a series of spinner axis settings ranging from $\beta_m - 0.020°$ (top left) to $\beta_m + 0.017°$ (bottom right). The single methyl resonance is off scale due to its large intensity. Crystallographic inequivalence of the 2,5 and 3,6 ring carbons was detected by a 1.7 ppm splitting in the ^{13}C spectrum by Lippmaa *et al*. (13) and it is well-known that the t-butyl groups do not rotate at room temperature. The deuterium isotropic spectrum at the magic angle (bottom left) shows two unequal peaks with 2.2 ppm splitting. Residual second order quadrupole and homonuclear dipole couplings evidently cause this effect. The ^{13}C, ^{2}H, and ^{1}H (Ch. IV) results are not consistent and further study is required to unravel the cause of the differences.

E. Proton-Enhanced Deuterium NMR in Rotating Solids

1. Introduction

Proton-enhanced nuclear induction spectroscopy is a powerful method for increasing the sensitivity of NMR in solids (8). It has been applied to enhance ^{13}C signals in magic angle spinning solids and those of various other spin ½ nuclei (7,11,13,58). The spinning modulates the dipole-dipole interactions which induce the transfer of polarization between the ^{1}H and ^{13}C Zeeman reservoirs in the rotating frame, but does not quench that process as long as the rotation frequency is somewhat smaller than the local dipole field (58). Transfer of polarization

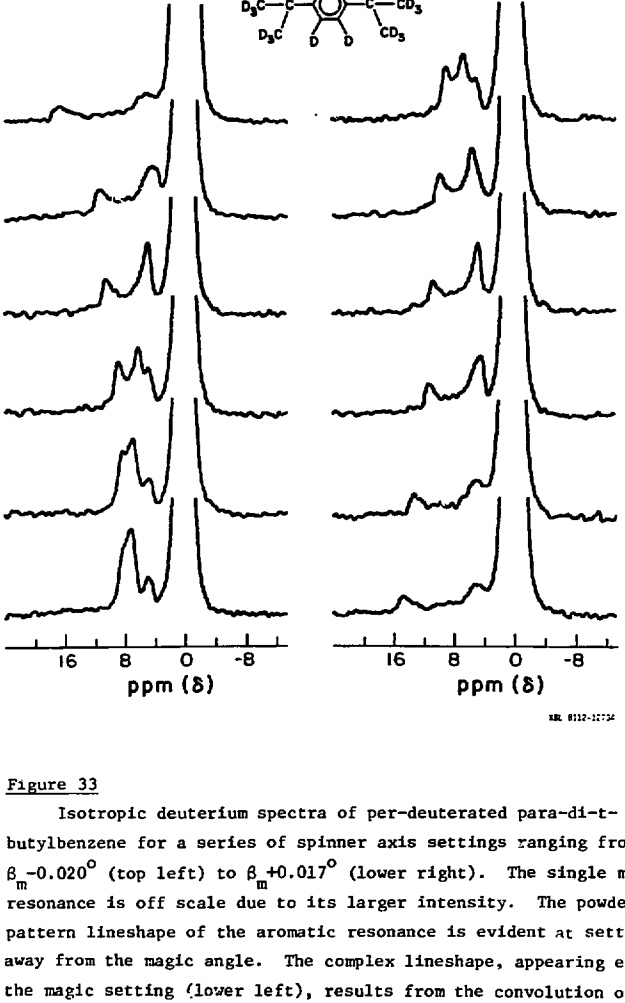

Figure 33

Isotropic deuterium spectra of per-deuterated para-di-t-butylbenzene for a series of spinner axis settings ranging from β_m-0.020° (top left) to β_m+0.017° (lower right). The single methyl resonance is off scale due to its larger intensity. The powder pattern lineshape of the aromatic resonance is evident at settings away from the magic angle. The complex lineshape, appearing even at the magic setting (lower left), results from the convolution of residual dipolar and second order quadrupole lineshapes.

between spin-½ (^{1}H) and spin-1 (^{2}H) systems has been investigated recently in non-rotating solids. Selective single- and double-quantum cross polarization have been demonstrated and their dynamics analyzed (25). Also, deuterium quadrupole tensor polarization by thermal contact between proton dipole and deuterium quadrupole reservoirs has been reported (50). Sample rotation modulates the quadrupole coupling as well as the dipole couplings and this affects both the efficiency and dynamics of the transfer of polarization. In this section the application of proton-enhanced NMR to deuterium in magic angle spinning powders is described and the conditions for efficient transfer of polarization from ^{1}H to ^{2}H analyzed (60).

2. Theoretical

The Hamiltonian for the deuterium spin systems (S) in the rotating frame and on-resonance ($\Delta\omega << \omega_{1S}, \omega_Q$) in the rotating frame has the form

$$H_S = \omega_{1S} S_x + \frac{1}{3}\omega_Q(t)(3S_z^2 - S^2), \qquad \text{(III-5)}$$

in frequency units, where ω_{1S} is the deuterium rf field amplitude and

$$\omega_Q(t) = \frac{3}{4} e^2 qQ\{\frac{1}{2}[3\cos^2\beta(t)-1]\} \qquad \text{(III-6)}$$

is the time-dependent quadrupole coupling amplitude. For simplicity, an axially symmetric quadrupole interaction is assumed where $\eta = 0$. H_S is diagonalized by a unitary transformation (44,45) and the result is given by

$$H_S^T = T^{-1} H_S T = \frac{1}{2}\omega_e(t) S_z - \frac{1}{6}\omega_Q(t)(3S_z^2 - S^2),$$

where

$$\omega_e(t) = [\omega_Q^2(t) + 4\omega_{1S}^2]\ ,$$

$$\tan\theta = \frac{2\omega_{1S}/\omega_e(t)}{\omega_Q(t)/\omega_e(t)}\ , \qquad \text{(III-7)}$$

$$T = \begin{pmatrix} 2^{-\frac{1}{2}}\cos\tfrac{1}{2}\theta & -2^{-\frac{1}{2}} & -2^{-\frac{1}{2}}\sin\tfrac{1}{2}\theta \\ \sin\tfrac{1}{2}\theta & 0 & \cos\tfrac{1}{2}\theta \\ 2^{-\frac{1}{2}}\cos\tfrac{1}{2}\theta & 2^{-\frac{1}{2}} & -2^{-\frac{1}{2}}\sin\tfrac{1}{2}\theta \end{pmatrix}$$

are the effective field amplitude, tilt angle, and transformation matrix respectively. In this transformation, columns 2 and 3 in the matrix of Equation 37 in Reference 45 are permuted in order to preserve the numerical labeling of states and symmetry in the tilted frame of reference. Thus both the magnitude and orientation of the effective field are modulated by the magic angle spinning. If deuterium Zeeman polarization can be generated, it must be able to adiabatically follow that modulation in order to remain spin-locked. The set of Bloch-like equations for an oscillating three-level system have been analyzed, which have previously been solved for a stationary three-level system (61). When the frequency of sample rotation, $\omega_r < \omega_{1S}, \omega_Q$ the spin polarization can adiabatically follow the modulation if the condition is fulfilled that

$$\omega_{1S}^2 >> \omega_r\omega_Q(t)_{max}, \qquad \text{(III-8)}$$

where $\omega_Q(t)_{max}$ is the maximum value of $\omega_Q(t)$ during the spinner cycle. Explicitly, when $\omega_{1S}^2 > 10\omega_r\omega_Q(t)_{max}$ the maximum deviation of spin orientation from the quantization axis in the frame given by Equation III-7 is less than 4°.

The Hamiltonian for the combined deuterium (S) and proton (I) spin system in a souble rotating frame defined by Equation III-7 and an on-resonance rf irradiation at the proton Larmor frequency has the form

$$H^T = H_I^T + H_{II}^T + H_S^T + H_{IS}^T, \qquad \text{(III-9)}$$

where H_S^T is given in Equation III-7, H_{II}^T is the secular dipole-dipole coupling amongst the protons, and $H_I^T = \omega_{1I} I_x$. The transfer of polarization is induced by H_{IS}^T which is given by

$$H_{IS}^T = \sum_{ij} 2b_{ij}(-I_{x,i}S_{x,j}^{1-2}\cos\tfrac{1}{2}\theta + I_{x,i}S_{x,j}^{2-3}\sin\tfrac{1}{2}\theta),$$

$$b_{ij} = -2\gamma_i\gamma_j r_{ij}^{-3} P_2(\cos\alpha_{ij}), \qquad \text{(III-10)}$$

where θ is given in Equation III-7 and the $S_{x,}^{p-q}$ are the fictitious spin-½ operators describing the spin-1 system (44,45). By second-order perturbation, H_{IS}^T induces either effective field deuterium single-quantum flips 1-2 or 2-3 accompanied by a proton flip. The Hartmann-Hahn matching conditions for these energy conserving flip-flops are given by

$$\omega_{1I} = \tfrac{1}{2}[\omega_e(t) - \omega_Q(t)] \text{ for the 1-2 transition} \qquad \text{(III-11a)}$$

and

$$\omega_{1I} = \tfrac{1}{2}[\omega_e(t) + \omega_Q(t)] \text{ for the 2-3 transition.} \qquad \text{(III-11b)}$$

The result of the transfer of polarization can be calculated by application of the spin temperature theory. For a non-spinning sample one can set $\Delta\omega$, $\omega_{1S} \ll \omega_Q$ and thus $\theta \ll 1$ so that only the S_x^{1-2} term survives in H_{IS}^T. This makes selective double-quantum cross polarization

possible (25). In a rotating sample the modulation of $\omega_Q(t)$ causes both terms in H_{IS}^T to be non-zero at some point during the rotor cycle. This results in a complex transfer of polarization involving both 1-2 and 2-3 transitions. The deuterium polarization created after a cross-relaxation contact is represented by the operators S_z and $3S_z^2 - S^2$ in Equation III-7. Transformation of these operators back into the original rotating frame of Equation III-5 gives

$$TS_zT^\dagger = 2^{-1/2}\sin\theta(S_x) + \frac{1}{4}\cos\theta(S_+^2 + S_-^2) + \frac{1}{2}\cos\theta(3S_z^2 - S^2), \qquad \text{(III-12)}$$

$$T(3S_z^2 - S^2)T^\dagger = -\frac{1}{2}(3S_z^2 - S^2) + \frac{3}{4}(S_+^2 + S_-^2). \qquad \text{(III-13)}$$

Thus the proton-enhanced deuterium system will exhibit single-quantum, double-quantum and quadrupole tensor polarization as a function of the effective frame tilt angle, $\theta(t)$, which is determined by the relative strength of ω_{1S} to $\omega_Q(t)$.

In a non-spinning polycrystalline sample only a few deuterium spins match the Hartmann-Hahn conditions of Equations III-11 and the polarization transfer is inefficient. However, rotation of the sample about the magic axis modulates the deuterium energy levels of Equation III-7 and thus the corresponding transition frequencies as shown in Figure 34 (top). The 1-2 and 2-3 transitions oscillate with large amplitudes. Setting the value of ω_{1I} within the range of that oscillation allows the deuterium spins to match the conditions of Equations III-11 at least once during the spinner cycle. Assuming an isotropic distribution for the orientation of the unique axis of the quadrupole interaction tensor in the sample, the fraction of deuterium spins that achieve the matching conditions is shown in Figure 34 (bottom) as a function of ω_{1S} for a

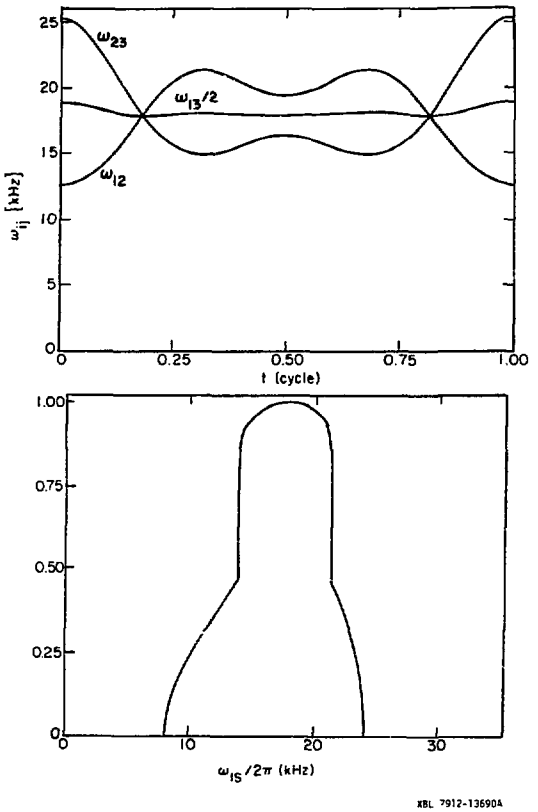

Figure 34

Theoretical aspects of ^{1}H-^{2}H cross polarizati n in rotating solids. Top: Dependence of the effective field transition frequencies, ω_{ij}, in the tilted rotating frame on the sample rotation for one spinner cycle. Parameters: $\Theta = 60^{o}$, $\omega_{Q} = 14.2$ kHz, $\omega_{1S} = 18$ kHz. Bottom: Fraction of sample, f_{S}, which meets one of the single quantum Hartmann-Hahn conditions at least once during a spinner cycle plotted vs. ω_{1S}.

constant ω_{1I}. In the region $\omega_{1S} \simeq \omega_{1I}$ all spins achieve matching and efficient cross polarization is expected. The distinct tails in Figure 34 (bottom) represent regions where only one of the two conditions in Equations III-11 can be matched during the spinner cycle. Thus the polarization transfer induced by H_{IS}^{T} via effective field single-quantum flips is possible over a wide range of $\omega_{1S} - \omega_{1I}$, however, the matching is obtained only for a fraction of the spinner cycle, and this reduces the rate of transfer that is possible (62).

An alternative mechanism for polarization transfer is a transition in which the deuterium spin undergoes an effective field double-quantum flip accompanied by one or two proton flips (63). This is the 1-3 transition in Figure 34 (top) which is forbidden by second-order perturbation and would require that $n\omega_{1I} = \omega_e(t)$, where n = 1,2. Since this transition oscillates over a much smaller range during the spinner cycle than the 1-2 and 2-3 transitions, it would lead to a much narrower matching region than that shown in Figure 34 (bottom).

3. Experimental Results

Proton-enhanced deuterium signals were obtained by spin-locking the proton magnetization followed by single-contact thermal mixing between the I and S reservoirs. The duration of the contact was a multiple of the spinner cycle. Both I and S rf irradiation were on-resonance. Following the mixing, the S irradiation was turned off and the I irradiation left on for proton decoupling while the S free induction decay was monitored directly. Experiments were performed at $\omega_0/2\pi(^2H) = 28$ MHz and $\omega_0/2\pi(^1H) = 182$ MHz.

Results on proton-enhanced deuterium signals for a sample of polycrystalline 30% randomly deuterated hexamethylbenzene rotating at 1.47 kHz are shown in Figure 35. The experimental proton rf field amplitude was $\omega_{1I}/2\pi = 20.8$ kHz. In Figure 35 (top) is shown the ratio of cross-polarized signal intensity, S^{CP}, to the intensity after a single 90° pulse, S^0, as a function of ω_{1S}. The duration of cross-relaxation contact was 25 cycles = 17 ms. The cross-polarization rates, $1/T_{IS}$, for this same data set are shown in Figure 35 (bottom). The cross-relaxation curves were fit to a single exponential to extract T_{IS}, however, the curves were not single exponential and the relative error in $1/T_{IS}$ is estimated to be ±20%. Maximum enhancement observed for this sample was $S^{CP}/S^0 = 3.2$.

The proton-enhanced high-resolution spectrum of polycrystalline dimethoxybenzene is shown in Figure 36. This sample was randomly deuterated to 66% in the aromatic position and selectively mono-deuterated to 98% in the methoxy position, $DH_2CO\text{-}\phi D_4\text{-}OCH_2D$. The maximum enhancement factors, S^{CP}/S^0, for some polycrystalline samples are summarized in Table X. Good enhancement was obtained in each case.

Theoretical values S^{CP}/S^0 for single-quantum spin-locked cross polarization are calculated from (8)

$$S^{CP}/S^0 = (\gamma^I/\gamma^S)(1+\varepsilon)^{-1}$$

$$= 6.514\ (1+8N_S/3N_-)^{-1} \qquad \text{(III-14)}$$

where $\varepsilon = [S(S+1)/I(I+1)]N_S/N_I$. In comparing these values to experimental values, it should be noted that the experimental S^0 is somewhat smaller than expected since the pulse is not "strong" for the entire

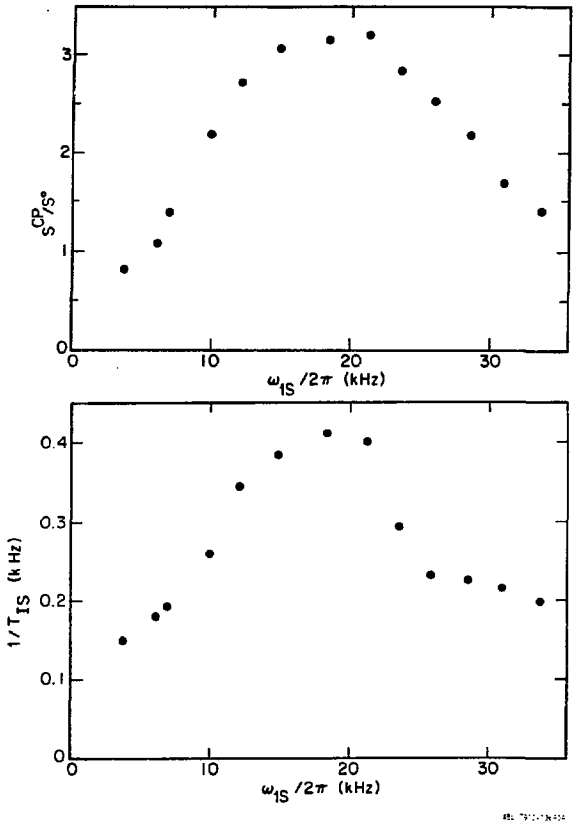

Figure 35

Cross polarization results for deuterated hexamethylbenzene with $\omega_r/2\pi$ = 1.47 kHz, $\omega_{1I}/2\pi$ = 20.8 kHz, and 17 msec contact time. Top: Deuterium signal enhancement factor, S^{CP}/S^{o}, as a function of ω_{1S}. Bottom: Cross polarization rates, $1/T_{IS}$, for the same data set.

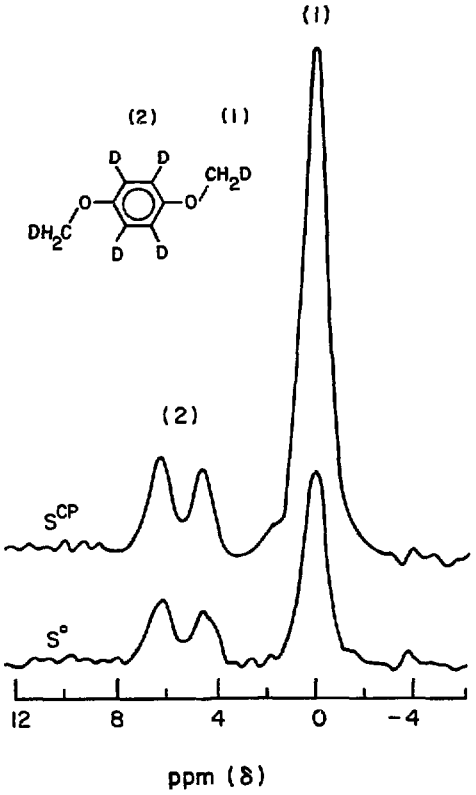

XBL 806-10092

Figure 36

Isotropic deuterium spectra of partially deuterated p-dimethoxybenzene (see Table VII, 4). Lower trace, S^{O}, was obtained from the fid after a single 90^{O} pulse. Upper trace, S^{CP}, shows gain in sensitivity resulting from 9 msec single contact cross polarization from protons.

TABLE X: Deuterium polarization enhancement for ^{1}H-^{2}H cross polarization in rotating powders

Compound	Position	τ (msec)	$\omega_{1S}/2\pi$ (kHz)	$\omega_{1I}/2\pi$ (kHz)	S^{CP}/S^{O} (expt.)	S^{CP}/S^{O} (theory)
1) p-dmb[1]	methyl(CH_2D 98%) aromatic (66%)	21	64	42	2.2 2.6	2.0
2) p-dmb	methyl (negligible) aromatic (>95%)	22	41	50	- 0.7	2.3
3) p-dmb	methyl (CH_2D 3%) aromatic (5%)	18	36	42	5.6 6.6	6.1
4) p-det[2]	methyl (2.5%) methylene (5.9%) aromatic (9.5%)	19	36	42	4.1 4.5	5.6

1. p-dimethoxybenzene
2. p-diethylterephthalate

powder. When $\omega_{1S} < \omega_Q$ the magnetizations of crystallites with different orientations are rotated by different angles. Thus a single pulse does not bring them all into the transverse plane as described in a previous section and it also generates some double-quantum coherence.

The theoretical enhancement for hmb was 3.0, slightly smaller than observed. Experimental values in Table X are given for each resolved region and the average of those values should be compared to the theoretical value. Close to theoretical enhancement was achieved in most cases, however, deuterons in rigid lattice positions with $\omega_Q \sim 130$ kHz gave enhancements strongly dependent on the matching conditions. This empirical result is illustrated in Figure 37 by the enhancement and T_{IS} data for p-dimethoxybenzene (sample (3) of Table VII). For this experiment $\omega_{1I}/2\pi = 42$ kHz. The unusual feature is that T_{IS} for the methyl resonance changes drastically in the region $\omega_{1I} \sim \omega_{1S}$ and the enhancement falls off rapidly for increasing ω_{1S}. Correspondingly, the enhancement in the aromatic resonance jumps sharply. While this is not completely explained, it is due in part to the broader matching region (see Fig. 34) of the aromatic deuterons with larger ω_Q and makes possible selective observation of one deuterium type over another when their ω_Q's are very different. For example, in Figure 38 are shown the isotropic spectra of p-dimethoxybenzene (sample (3) of Table VII) for various spinner axis settings obtained by cross-polarization. In Figure 38c, the $\omega_{1S}/2\pi =$ 63 kHz and $\omega_{1I}/2\pi = 42$ kHz so that the aromatic signal is selectively enhanced (see Fig. 37), which was used in this case to measure ω_Q. It is also interesting that in Figure 38b the quadrupole powder patterns of the aromatic peaks are clearly seen to be separated by their difference in isotropic shifts (measured in Fig. 38a).

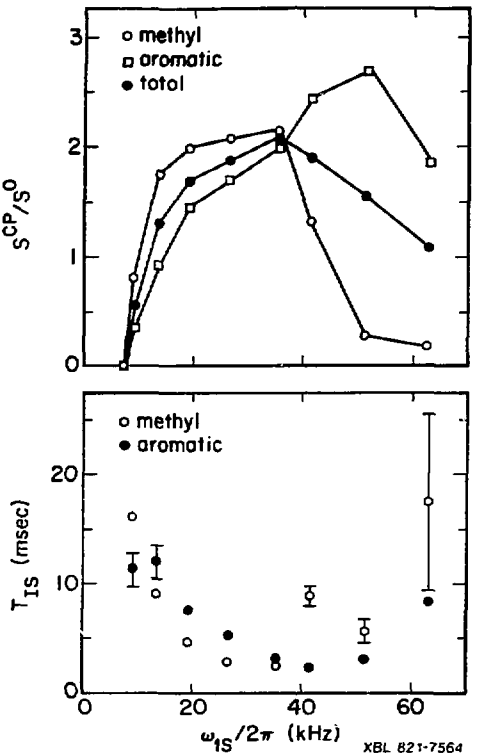

Figure 37

Cross polarization results for partially deuterated p-dimethoxybenzene (see Table VII, 3), with $\omega_{1I}/2\pi$ = 42 kHz. Top: Deuterium signal enhancement factor, S^{CP}/S^{O}, as a function of ω_{1S}. Increase of aromatic enhancement at higher ω_{1S} is due mainly to its larger ω_Q and Hartmann-Hahn matching region. Bottom: Cross polarization times, T_{IS}, for the same data set.

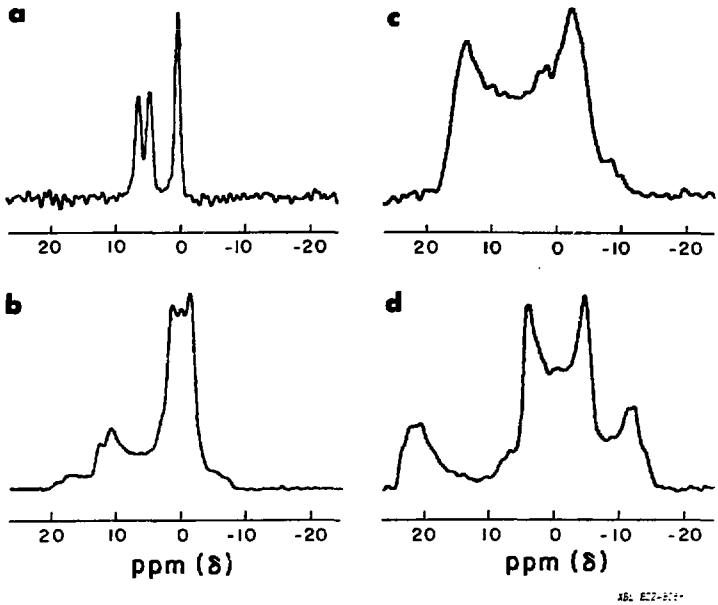

Figure 38

Isotropic deuterium spectra of p-dimethoxybenzene (Table VII,3) obtained by ^{1}H-^{2}H cross polarization for a series of sample spinner axis settings. a) Exact magic angle setting, b) off magic setting with chemical shifts and quadrupole powder patterns observable, c) A further off magic setting with selective cross polarization enhancement of the aromatic deuterons (see Figure 37) at $\omega_{1S}/2\pi$ = 63 kHz, d) A further off magic setting illustrating chemical shifts and quadrupole powder patterns.

4. Conclusion

Evidently most of the transferred polarization does remain locked along the effective field as its direction oscillates. The broad matching curve and cross-relaxation data of Figures 35 and 37 strongly support the conclusion that the transfer of polarization occurs by the two-spin single-quantum flip-flop process. In a rotating powder there is a continuum of oscillating Hartmann-Hahn conditions which leads to a very complex cross-polarization dynamics and a broad range of ω_{1S} over which the energy conserving heteronuclear flip-flops occur. In the limit that $\omega_{1S} >> \omega_Q$ and $\omega_{1S} = \omega_{1I}$, pure single-quantum signal is generated by the transfer of polarization. However, when $\omega_{1S} \geq \omega_Q$ the single-quantum signal exceeds 95% of the total. Thus the observed polarization should fall off more quickly on the low-frequency side where $\omega_{1S} < \omega_{1H}$ than the high frequency side since in this region more of the transferred polarization appears as double-quantum coherence and quadrupolar polarization. The experimental cross-polarization curves, Figures 35 and 37, are broader than the theoretical matching curve, Figure 34 (bottom). Two reasons for this are: 1) the cross-relaxation spectral density function is considerably broadened by spinning sidebands as demonstrated by Stejskal et al. (58) and 2) the mismatch energy, $\omega_{1I} - \frac{1}{2}[\omega_e(t) \pm \omega_Q(t)]$, appears in the proton reservoir H_{II}^T and can be the limiting factor in cross relaxation in a non-rotating sample. However, it was recently demonstrated that sample rotation strongly couples this reservoir to the lattice (64).

Since the substitution of ^2H for ^1H is under the control of the experimenter, two effects become important for high resolution deuterium NMR. First, the level of ^2H substitution should not be too high so that

the small residual homonuclear dipole broadening is minimized. Second, the sensitivity gain by proton-enhanced spectroscopy must take into account the substitution of ^{1}H by ^{2}H. In the usual case, e.g., ^{13}C at 1% natural abundance, the protons are at 100% natural abundance. In the present case, the substitution changes drastically the ratio N_S/N_I. Furthermore, the theoretical gain must in fairness be compared to a 30% deuterated sample, for example, which the experimenter might choose and which has negligible residual homonuclear dipole broadening. Using the enhancement factor calculated by Pines et al. (8) for multiple contact cross polarization, but comparing the gain to an arbitrary 30% deuteration level, the actual enhancement factor is about two for levels of substitution from 10-80%, but it is much less outside that range. As will be shown in Chapter IV, levels of deuteration 90% are also desirable and thus in practice one would prepare samples with e.g., 30% and 90% deuteration. Cross polarization then offers a substantial savings in time of approximately a factor of four, not including relaxation considerations. The advantage of Proton-Enhanced spectroscopy often lies in the fact that the S spins may be repolarized after T_1 of the I spins or may be repolarized many times during the spin-locked $T_{1\rho}$ of the I spins. The T_1 for deuterium and many other naturally dilute nuclei can be extremely long in solids while T_1 for protons is usually some several seconds or less when methyl groups are present and can be more easily controlled by paramagnetic relaxation agents due to its abundance and large γ_n. For instance, taking relaxation into account the gain for sample (5) of Table VII is enormous since T_1 for the rigid lattice deuterons is several hundred seconds. Several of the results of the previous section were obtained by multiple contact cross polarization,

e.g., Figure 29 for which six contacts were used. Details of cross polarization dynamics and off resonance irradiation have been investigated by Muller (65).

F. Double Quantum NMR with Magic Angle Spinning

1. Introduction

Magic angle spinning removes the broadening of spectra of amorphous and polycrystalline samples due to anisotropic quadrupole and chemical shift interactions. Practically, a spectral narrowing of about three orders of magnitude is achieved and an extremely stable sample spinner is required having angular fluctuations smaller than a few millidegrees. It has been shown that by detecting the deuterium double quantum transitions in non-rotating samples the anisotropic chemical shift powder pattern can be obtained since the double quantum absorption lines are free of the large first order quadrupole broadening (17-21, 44,45). In this section the combination of magic angle spinning with double quantum NMR is presented as an alternative approach to high resolution in solids (66). In removing the quadrupole coupling via the detection of double-quantum transitions the spinner requirements become much less stringent since it has only to remove the smaller chemical-shift anisotropy as in the case of high-resolution magic angle ^{13}C NMR.

2. Double Quantum NMR in Rotating Solids

The "forbidden" deuterium ($I = 1$) double-quantum transitions ($\Delta m = 2$) are independent of the quadrupole coupling to first order. Thus the double-quantum spectrum for polycrystalline and amorphous solids

usually consists of overlapping chemical-shift powder patterns. By rotating the sample about the magic angle and sampling the double-quantum FID in multiples of spinner cycles, $\tau_r = 2\pi/\omega_r$, the remaining chemical shift anisotropy is also removed. Since the range of the chemical shift is over two orders of magnitude smaller than the quadrupole splittings, it is expected that the width of double-quantum resonance lines is considerably less sensitive to deviations of the spinner axis from the magic angle. Also, the chemical shift of the double-quantum line is just twice that of the single-quantum line.

Double-quantum coherence is prepared by two strong pulses near resonance separated by a short delay as in Figure 39. After evolution for some number of spinner cycles, $t_1 = n\tau_r$, a detection pulse creates single-quantum signal (FID) which appears as a train of rotational echoes since the sample is rotating about the magic angle. A series of such FIDs for increasing values of $n = 1,2,3...$ are collected. The decay of the first rotational echo in each of these FIDs is Fourier transformed to give a single-quantum quadrupole powder pattern spectrum. The double-quantum FID is obtained as a cross section through these spectra in the second or t_1 time domain. This procedure avoids receiver ring-down after the detection pulse and phase cancellation of double-quantum coherence which occurs in a cross section through the rotational echoes. Fourier transformation of the double-quantum FID then gives the frequency spectrum of the t_1 domain (2D or two-dimensional spectrum). For the three-level spin-1 deuterium system this spectrum exhibits any single- and double-quantum coherence which existed after evolution time t_1. In the present work, α was set to a value less than 90° (Fig. 39) in order to allow simultaneous generation of single- and double-quantum lines in the 2D spectrum.

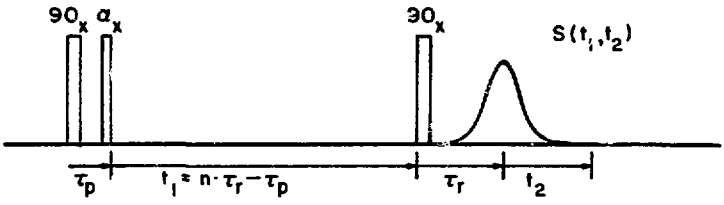

XBL 7912-6211

Figure 39

Pulse sequence for observation of deuterium isotropic chemical shift spectrum in solids by double-quantum NMR with magic angle spinning. Double-quantum coherence is prepared by a pair of strong pulses and evolves during time t_1 which is an integral multiple of sample spinner cycles. A third detection pulse transfers double-quantum to observable single-quantum coherence which appears as a train of rotational echoes. The decay of the first echo (t_2 domain) is Fourier transformed and the double-quantum FID is obtained as a cross section through those spectra as n = 1,2,3,...(t_1 domain). Proton decoupling is applied except during the deuterium rf pulses.

The pulse sequence of Figure 39 was applied to a powder sample of 28% randomly deuterated ferrocene rotating at 1.11 kHz with $\omega_0/2\pi(^2H)$ = 28 MHz. The ferrocene ω_Q' = 73 kHz. A new set of spectra were taken with β'' adjusted to the optimal narrowing setting and at successive deviations from that setting. Each set consisted of the usual single-quantum spectrum from the FID after a single pulse (one-dimensional or 1D) and the 2D spectrum as described above. The results are shown in Figure 40.

3. Results

The 1D spectra show the narrowing of the quadrupole powder pattern to a sharp line as the angle β'' becomes magic. The 2D spectra exhibit single-quantum (1-Q) and double-quantum (2-Q) lines and the chemical shift of the 2-Q line is just twice that of the 1-Q line. While the 1-Q linewidth depends strongly on the adjustment of β'', the 2-Q linewidth is insensitive to it. For small deviations of β'' from the optimal setting, the 1-Q line broadens and falls into the noise while the 2-Q linewidth does not change.

The width of the 1-Q line is 20 Hz and the width of the 2-Q line is about twice that value. Static field inhomogeneity and susceptibility contributions to the linewidth have exactly double their effect for double quantum transitions since all relative shifts are doubled. The second order quadrupole perturbation shifts only the $m = \pm 1$ levels leading to a broadening and shift as described previously, which are exactly twice in size for the double quantum transition relative to the single quantum transition at exact magic angle.

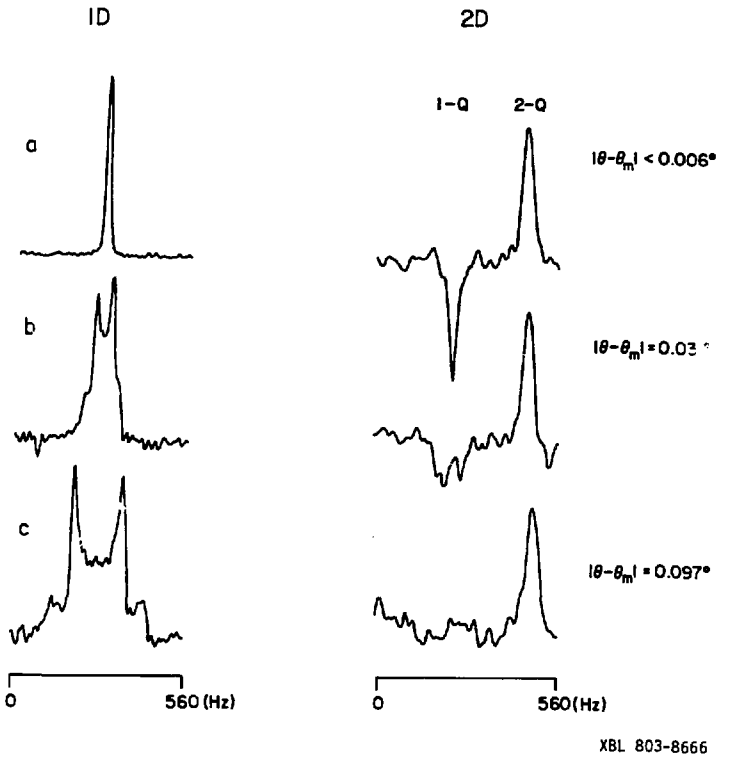

Figure 40

One-dimensional (1D) and two-dimensional (2D) deuterium solid state spectra of polycrystalline 28% randomly deuterated ferrocene-d_{10} rotating at 1.11 kHz. The 1D spectra show the narrowing of the ferrocene (ω_Q = 73 kHz) quadrupole powder pattern by the spinning as θ approaches the magic angle. The 2D spectra exhibit the single-quantum (1-Q) and double-quantum (2-Q) lines and illustrate the fact that the 2-Q chemical shift is double that of the 1-Q. As θ deviates from the magic setting, the 1-Q line splits into the quadrupole powder pattern and is lost in the noise while the 2-Q line remains sharp.

On the basis of these results, the combination of double-quantum NMR with magic angle spinning offers the possibility for high resolution without unusually stringent spinner requirements, especially in complicated molecules with several inequivalent deuterium positions. Furthermore, the use of double-quantum magic angle NMR was combined with cross-polarization to enhance sensitivity. The 90° pulse applied to deuterium in Figure 39 is replaced by the spin-locked cross polarization sequence as described in the previous section.

G. Deuterium Spin Diffusion and Spin-Lattice Relaxation

1. Introduction

In the previous sections techniques for high resolution deuterium NMR of solids were demonstrated. It is therefore important to understand the mechanisms of deuterium spin-lattice relaxation in the solid state. It is well-known that T_1 in this case can become some minutes and longer making the observation of deuterium resonances almost useless. However, it was first noticed in this work that certain spin-lattice relaxation rates in rotating solids were much faster than expected and that this must be due to dipolar spin diffusion between crystallographically inequivalent deuterium nuclei.

Thus the question of spin diffusion in the deuterium system is a critical aspect of deuterium NMR in solids in both the stationary and rotating sample cases. The related problem of cross relaxation by level crossing between the Zeeman levels of a spin-$\frac{1}{2}$ system and the quadrupole levels of a spin > $\frac{1}{2}$ system has been studied extensively (6,67). In this section, a new regime of homonuclear cross relaxation or spin diffusion within a quadrupolar spin system ($I = 1$) is described by further

application of the average Hamiltonian theory (68). The results are discussed in regard to stationary and rotating samples.

2. Relaxation Mechanism

The spin-lattice relaxation of spin-1 deuterium in solids in high magnetic field at high temperature is normally dominated by its large quadrupole coupling (1). When there is molecular motion, the time dependence introduced into the quadrupole coupling by the motion can be effective in producing spin-lattice relaxation. In the absence of such motion, T_1 can be orders of magnitude longer since other motions in the crystal, e.g., lattice vibrations, are much less effective in producing spectral density at the deuteron Larmor frequency. In a crystal containing both rapidly reorienting and rigid deuterium types, for example, a typical organic molecular solid containing $-CD_3$ groups, the spin diffusion between deuterons attempts to bring both types into internal equilibrium at a common spin temperature. The complete system would then relax to the lattice temperature (6). However, the dependence of the quadrupole coupling on orientation in the external magnetic field quenches the spin diffusion and causes the different deuterium types to relax at independent and widely different rates.

This effect is described qualitatively for deuterium in high magnetic field in an axially symmetric electric field gradient in Figure 5. Neighboring deuterons in a crystal, illustrated by the left and right hand sides in Figures 5a and 5b, can have different orientations of the unique axis of their quadrupole interaction tensors with respect to the external magnetic field direction. They will then have largely different quadrupole splittings, Ω_Q, as indicated in Figure 5a, and a flip-flop

transition due to the $I_+^i I_-^j + I_-^i I_+^j$ term of their dipole-dipole coupling would not be allowed since it is not energy conserving. Thus the spin diffusion between these deuterons is quenched. For spin diffusion to occur, their quadrupole splittings must be equal to within a local field width. In other words, the quadrupole satellites of the two nuclei must overlap as shown in Figure 5b. The dependence of the quadrupole splitting on orientation is illustrated in Figure 5c. The quenching of spin diffusion in a powder sample occurs since there is an isotropic distribution of crystallite orientations. For neighboring deuterons in a crystallite, which have different directions of their unique quadrupole axis in the crystal fixed reference frame, to undergo spin diffusion the crystallite must fall at such an orientation in the lab frame that the two deuterons have the same quadrupole splitting, Ω_Q. Only a negligible fraction of the crystallites of the powder will meet that condition. Since the deuterium quadrupole coupling is much larger than its dipole-dipole couplings, the matching of quadrupole splittings occurs over a very small angular range. A similar quenching of cross relaxation among chemically shifted $^{31}P(I = \frac{1}{2})$ resonances and the restoration of cross relaxation by sample rotation was studied by Andrew et al. (69).

When the sample is rotated about the magic angle, the quadrupole splitting of the deuterons is modulated harmonically. This modulation is shown in Figure 6 for two deuterons which have different orientations, i.e., polar angles, of their unique quadrupole axis with respect to the axis of sample rotation. At some point during the rotation cycle, the quadrupole splittings of the two deuterons must become equal and during this crossing the spin diffusion can occur. The width of the crossing region depends on the magnitude of the dipolar coupling between the

crossing deuterons and the steepness with which their quadrupole splittings cross. During the rotation cycle, the quadrupole splitting of each deuteron crosses with that of every other deuteron. Therefore, the sample rotation matches the quadrupole splittings of all pairs for some part of the cycle and partially restores spin diffusion in the deuterium system. This may also be viewed as a cross relaxation between crystallographically inequivalent deuterons.

3. Average Hamiltonian for Dipolar Coupled Spins I = 1

The crucial issue at this point is to elucidate the couplings between deuterons provided by their mutual homonuclear dipole coupling, $\mathcal{H}^D_{SS}$, and determine the possible pathways for spin diffusion. This analysis was performed by application of average Hamiltonian theory and was given in Chapter ID4. Details are given in Appendix A.

The results of the calculation shown in Equations I-35 through I-38 are summarized in Table XI. Consider first the non-rotating solid. When the quadrupole splittings are equal or equal and opposite, the usual first order spin diffusion process is resonant as described in the previous section. When the quadrupole couplings are unequal, the term $0\omega^2_{SS}/\omega_Q$ in Equation I-35 and smaller terms, which are not shown and may be significant, will provide spin diffusion at a lesser rate than the first order process. This is analogous to the result obtained by time-dependent perturbation theory to second order.

In the magic angle rotating solid the first order resonant process exists, but is reduced by one to three orders of magnitude since it is only in effect at "crossing points" as described in the previous section. It is assumed that $\omega_r >> \omega_{SS}$ which is generally true for ^2H, ^{14}N. The

TABLE XI: Average Hamiltonian spin diffusion terms for spins I = 1 in solids

Experiment	term description	average Hamiltonian term	reference equation
non-rotating sample	resonant crossing (equal Ω_Q)	$H''_{SS} \propto I^i_+ I^j_- + I^j_- I^j_+$	I-35
	non-resonant (unequal Ω_Q)	$0\omega^2_{SS}/\omega_Q$ + smaller terms	I-35
magic angle rotating sample	"average" resonant crossing	$H'''_{SS} \propto I^i_+ I^j_- + I^i_- I^j_+ << H''_{SS}$	I-38
	"average" non-resonant	$\overline{0\omega^2_{SS}/\omega_Q}$ + smaller terms	I-37

sample rotation also causes an averaging of the higher order spin diffusion terms and probably reduces them by less than an order of magnitude.

A recent experiment by Schajor et al. (70) seems to indicate that the higher order spin diffusion does take place in the non-rotating solid. While the situation in magic angle rotating solids is not completely explained, it is clear that further experiments performed first on stationary single crystals are necessary to clarify the physics. Major problems remaining to be resolved are 1) full calculation of all the higher order terms and 2) analysis of the effect of even a few percent remaining protons whose dipolar "bath" may still affect the spin-1 deuterium system (71). In the following paragraphs, experimental results are shown to demonstrate some major points of the theory given above.

4. Experimental Results

Spin-lattice relaxation times were measured by the saturation-recovery sequence. High power ($\omega_1/2\pi \simeq 50$ kHz) rf irradiation was applied for 5-20 msec to saturate the deuterium spin system. The recovery of Zeeman magnetization was probed after a variable delay with a "90°" pulse.

In the series of model compounds studied the spin-lattice coupling was provided by the fast rotation of methyl groups. It has long been known that the time dependence induced in the quadrupole coupling by the methyl rotation is an effective relaxation mechanism (1).

A typical saturation-recovery plot for the methyl deuterons in magic angle rotating p-diethylterephthalate is shown in Figure 41. The recovery is exponential within measuring error and does not depend on rotor frequency as expected. The T_1's for methyl deuterons in several

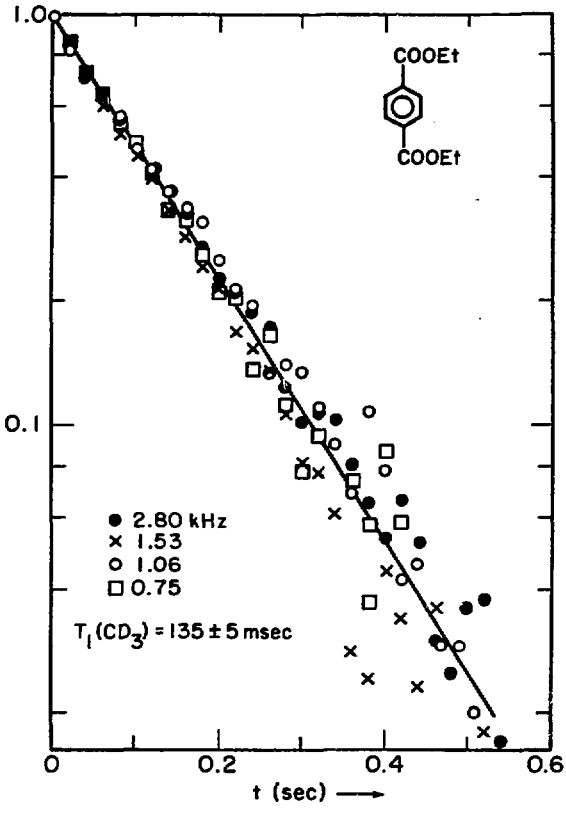

XBL 787-9793

Figure 41

Deuterium magnetization saturation-recovery graph for methyl deuterons in magic angle rotating p-diethylterephthalate. The recovery is single-exponential and does not depend on rotor frequency.

per-deuterated model compounds are summarized in Table XII. The values range from .01 to 1 second reflecting the distribution of rotational correlation times, τ_c, of the methyl groups in the different crystals. The methyl rotation in p-dtbb (Table XII) is evidently sterically hindered leading to a longer τ_c and shorter T_1. The special case of hexamethylbenzene with C_3 and C_6 rotations has been studied in detail previously (72). The methyl T_1 does not depend on the presence of protons and indicates that it has a single particle relaxation mode at room temperature depending only in the time dependence of the quadrupole interaction induced by the C_3 rotation. As the results described below will show, it is also a relatively fast relaxation mode so that a methyl group acts as a polarization or heat sink for non-methyl deuterons.

In the compounds listed in Tables XII and XIII the non-methyl positions are all rigid lattice types. Their spin lattice relaxation will depend on couplings to other nuclei as discussed above. Their T_1 values for per-deuterated solids range from 1 to 28 seconds, reflecting the differences in those internuclear couplings from crystal to crystal. The internuclear coupling is dipolar and thus depends on the distance as r^{-3}. The cross relaxation rate then should be a function of r^{-6}. Assuming that the differences in methyl T_1's in Table XII are inconsequential, one might expect a correlation of the rigid lattice positions' T_1 with inter- and intramolecular crystal distance to the methyl group. The data in Table XII does not show such a correlation. For example, calculation based on X-ray data (73) shows that one phenyl deuteron in p-det has one closest neighbor methyl at 4.25 Å, while in p-dimethoxybenzene the analogous phenyl deuteron has close methyl neighbors at 2.57, 3.40, 3.46, 3.61 Å, and several more at the 4-5 Å range. Furthermore, the phenyl-methyl and phenyl-methylene deuteron distances in p-det

TABLF XII: Deuterium spin-lattice relaxation times (T_1) in per-deuterated magic angle rotating solids (seconds).

Compound	Deuteration	Position		
		methyl[1]	methylene	aromatic[2]
p-det $D_3CD_2CO_2C\phi D_4CO_2CD_2CD_3$	see TABLE VIII 1)	0.14	8±3[3]	22±6
p-dmt $D_3CO_2C\phi D_4CO_2CD_3$	see TABLE IX 2)	0.86	—	28
p-dimethoxybenzene $D_3CO\phi D_4OCD_3$	see TABLE VII 1)	0.26	—	6
p-dtbb $(CD_3)_3\phi D_4(CD_3)_3$	see TABLE IX 6)	0.010	—	7
1,8-dimethylnaphthalene	>97% of all sites	0.92	—	1.1
hexamethylbenzene	>90% of all sites	0.037	—	—

1. uncertainty in methyl T_1 < 10% in all cases.
2. uncertainty in aromatic T_1<17% except where noted.
3. non-exponential.

TABLE XIII: Deuterium spin-lattice relaxation times (T_1) in partially deuterated magic angle rotating solids (seconds).

Compound	Deuteration	Position		
		methyl[1]	methylene	aromatic[2]
(deuteration note)				
1) p-dimethoxybenzene (all positions partially deuterated)	see TABLE VII 3)	0.28	—	3.0
2) p-dimethoxybenzene (all positions partially deuterated)	see TABLE VII 4)	0.28	—	3.3
3) hexamethylbenzene (25% random all positions)	25% random	0.086	—	—
4) p-diethylterephthalate (methylene protonated)	see TABLE VIII 3)	0.13	—	3.0
5) p-diethylterephthalate (aromatic protonated)	see TABLE VIII 4)	0.11	0.45±0.05[3]	—
6) p-diethylterephthalate (methyl protonated)	perdeuterated (except methyl protonated)	—	infinity	infinity
7) p-dimethoxybenzene (methyl protonated)	see TABLE VII 5)	—	—	399±12
8) p-dimethylterephthalate (methyl protonated)	perdeuterated (except methyl protonated)	—	—	640±80

1. uncertainty in methyl T_1 < 10% in all cases.
2. uncertainty in aromatic T_1 < 10% except where noted.
3. exponential within measuring error.

are 4.25 and 2.80 Å respectively. In both the above cases the correlation of distance and rigid lattice T_1 is in the correct direction, but is very weak. Also, the shortest aromatic-methyl distance in 1,8-dimethylnaphthalene is about 3.1 Å, yet the aromatic T_1 is unusually small. Since the methylene magnetization recovery was strongly non-exponential in p-det, then either multiple cross relaxation rates between sites or multiple spin diffusion mechanisms would be predicted.

To distinguish between first order spin diffusion via quadrupole crossing in the rotating sample and spin diffusion via higher order coupling, the powder pattern spectra of per-deuterated p-dimethoxybenzene powder are shown in Figure 42. On the left is the spectrum obtained in the stationary powder by the pulsed echo method. On the right is the spectrum in the magic angle rotating powder obtained by Fourier transformation of the rotational echo, all other factors being equal. The latter spectrum is similar to Figure 15 and the corresponding T_1's were given in Table XII. The T_1 of aromatic deuterons is apparently smaller in the rotating powder since some aromatic signal is available. This suggests that the first order "crossing" mechanism is dominant, however, the difficulty of measuring broad powder patterns with "weak" rf pulses (see Ch. IIIC) makes this result inconclusive.

The deuterium spin-lattice relaxation times in partially deuterated rotating solids are summarized in Table XIII. Except for hexamethylbenzene, the methyl T_1's are the same as in the perdeuterated compounds. When the methyl groups are not deuterated, the T_1 of rigid lattice positions becomes very long. For example, the magnetization recovery of aromatic deuterons in p-dimethylterephthalate, shown in Figure 43, becomes very slow when the methyl groups are protonated.

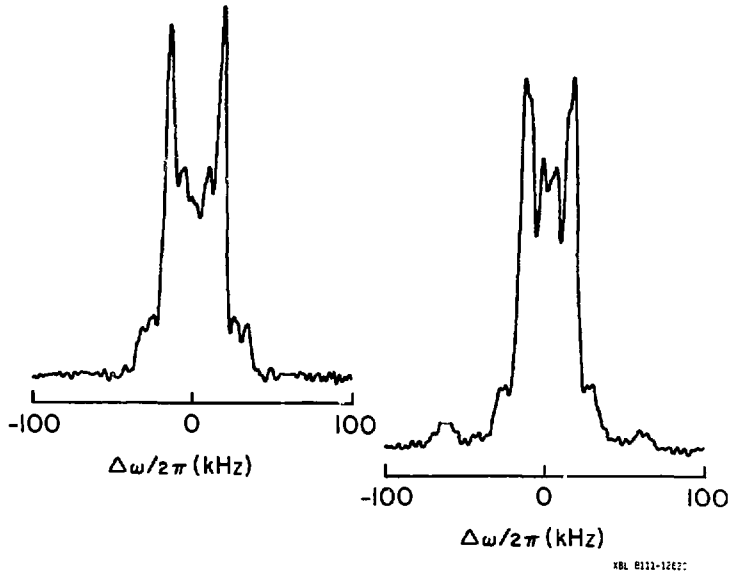

Figure 42

Quadrupole powder pattern spectra of per-deuterated p-dimethoxybenzene. Left: Spectrum obtained from the stationary powder by the pulsed echo method. Right: Spectrum obtained from the magic angle rotating powder from the rotational echo Fourier transform, all other factors being equal. Singular peaks of the powder pattern for aromatic deuterons are evident.

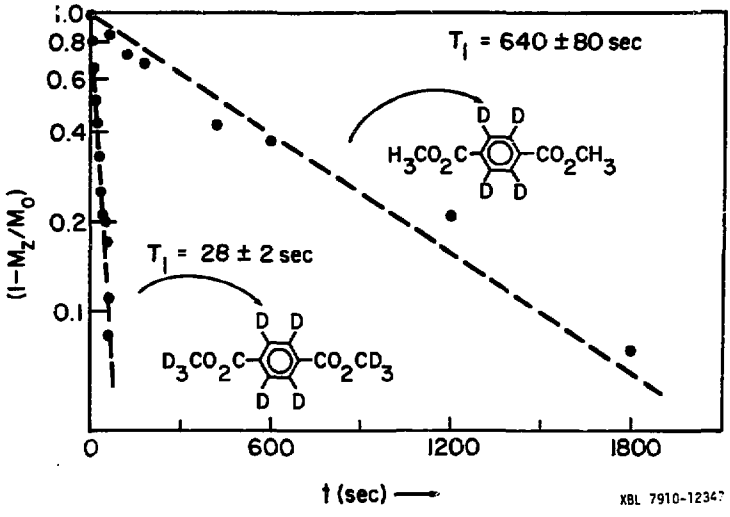

Figure 43

Deuterium magnetization saturation-recovery graph for aromatic resonance in p-dimethylterephthalate with magic angle rotation at 1 kHz. The aromatic group T_1 increases dramatically when the methyl group deuterons are replaced by protons.

It is also clear from the data in Table XIII that the presence of many ^{1}H nuclei strongly affects the T_1 of rigid lattice deuterons, reducing them substantially. Also, the recovery of methylene magnetization in p-det becomes single exponential. The proton dipolar bath is certainly coupled to the deuterium system, however, both the $^{1}H-^{1}H$ and $^{1}H-^{2}H$ dipolar couplings may be of the same order of magnitude as the sample rotation frequency and the physics of the problem becomes more complex. As was pointed out in the description of cross polarization in rotating samples, the sample rotation is known to strongly affect the temperature of a dipole reservoir (64).

In conclusion, the spin-lattice relaxation behavior in the spin-1 deuterium system in rotating solids has been investigated. The sample rotation strongly modulates the nuclear couplings involved. The ability to obtain resolved chemical shift spectra makes possible the measurement of site selective T_1's. A more complete understanding of the relaxation should be gained by measurements made first on stationary single crystals where the many nuclear couplings are more easily unraveled. Such studies are currently being undertaken.

IV. HIGH RESOLUTION PROTON NMR OF SOLIDS

A. Introduction

Measurement of high resolution NMR spectra of hydrogen in solids has long been difficult due to its large homonuclear dipole-dipole broadening. Magic angle sample rotation has made the observation of high resolution spectra of many other spin-½ nuclides routine, e.g., ^{13}C, ^{31}P. Since these nuclides are naturally isotopically dilute, their homonuclear dipolar broadening is small and is readily spun away. However, this is not the case for protons in solids. In the previous chapter the measurement of isotropic chemical shift spectra of deuterium in solids was demonstrated. This may be considered as an alternative to the direct observation of hydrogen.

There are a large number of cases where the proton homonuclear dipole broadening, H_{SS}^{D}, is largely reduced due to rapid internal molecular motions. Also, in many systems hydrogen is found to be spatially dilute, often occurring singly, in pairs, or in small clusters. This situation often occurs in inorganic materials. In these situations, magic angle rotation can often be applied to remove H_{SS}^{D}. In the general case, H_{SS}^{D} can be made under the control of the experimenter by isotopic dilution of ^{1}H with ^{2}H. In Chapter I the average Hamiltonian theory was applied to the case of hydrogen diluted in a deuterated solid under magic angle rotation. In the following paragraphs, experimental results are demonstrated.

B. Partially Reduced H_{SS}^{D} for Hydrogen

When the homogeneous dipolar broadening is large in frequency

compared to the sample rotation, the resonance line is not much affected by magic angle rotation (74). Spinning sidebands do not begin to appear until ω_r becomes a substantial fraction of $(\Delta\omega^2)^{\frac{1}{2}}_{SS}$. For example, in Figure 44 is shown the proton spectrum of 49% randomly deuterated hexamethylbenzene with magic angle rotation at 3.2 kHz. The stationary proton resonance has a full width at half intensity of 8 kHz. Sidebands have appeared even at this rotation frequency and the center band has a width of 1.4 ppm. The susceptibility broadening for this compound was shown in Chapter III to be 0.8 ppm, thus a residual dipolar broadening of the center band of 0.6 ppm = 0.22 kHz is indicated.

A further illustrative example is shown in Figure 45, the spectra of 30% randomly deuterated adamantane with magic angle rotation at 4.1 kHz. This sample was partially deuterated to compare proton and deuterium results. Adamantane is a plastic crystal and its molecules are undergoing rapid isotropic reorientation. Thus the homogeneous proton dipolar broadening results only from a residual intermolecular coupling and was about 10 kHz full width at half intensity. The proton resonance linewidth in Figure 45 is 2.0 ppm. Although a susceptibility broadening of 0.5 to 0.8 ppm for ^{13}C under magic angle rotation has been reported (53), the deuteron resonance in Figure 45 is 0.3 ppm in width. Assuming this value may be taken as the susceptibility broadening, a residual proton homonuclear dipole broadening of 2.0 - 0.3 = 1.7 ppm is indicated.

The residual proton dipolar broadening of the center band under magic angle rotation is much larger for adamantane than for hexamethylbenzene even though the conditions are comparable. A probable explanation for this fact is that the proton dipolar coupling in hexamethylbenzene has a more "inhomogeneous" character than that of adamantane. The most

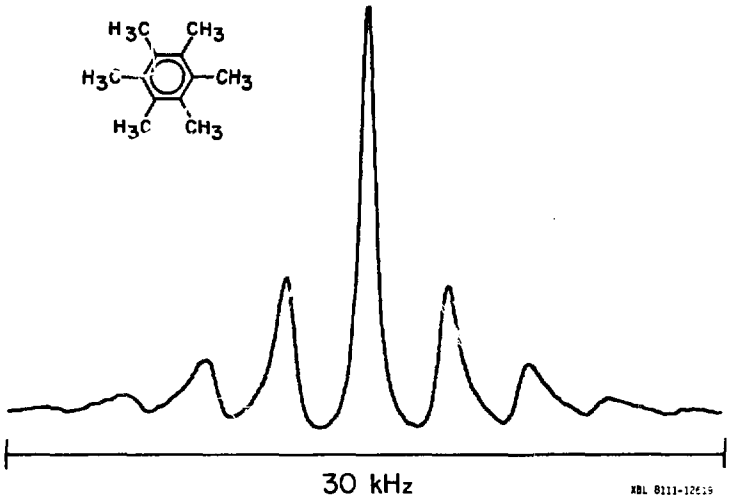

Figure 44

Proton spectrum of 49% randomly deuterated hexamethylbenzene with magic angle rotation at 3.2 kHz. Full width at half intensity of the center band is 1.4 ppm and is due mainly to susceptibility broadening.

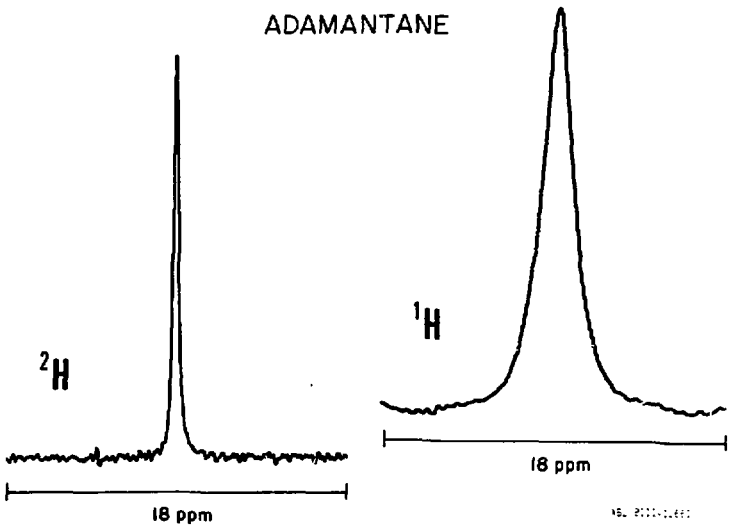

Figure 45

Proton and deuterium resonances of 30% randomly deuterated adamantane with magic angle rotation at 4 kHz.

probable group in the 49%-deuterated hmb is $-CH_2D$, thus each proton has one nearest neighbor proton. The coupling of a pair of spins-½ gives a Pake doublet (75) and the Hamiltonian for such a coupling is nearly completely inhomogeneous (12) and thus can be removed by slow magic angle rotation. In the present case the methyl groups in hmb are not well isolated, however, the criterion for fast sample rotation may be reduced.

The reduction of the static proton H^D_{SS} by molecular motion and semi-isolation of the proton spins should allow the study of many macromolecular systems by magic angle rotation. For example, the isotropic chemical shift spectrum of normal Delrin (Du Pont) polymer is shown in Figure 46. Delrin is a strong polymer used to construct the magic angle rotors. The spectra of Figure 46a, b, and c were of one particular commercial lot. As many as six resonances are detected in the isotropic spectrum and there is clearly a significant difference in the material from the two commercial lots. The chemical shift scale is referenced arbitrarily. Not shown in Figure 46 are the ±1 spinning sidebands which are each 25% of the intensity of the center band. The ±2 spinning sidebands were barely visible.

The appearance of many resonances in Figure 46 is remarkable since the monomer is $-CH_2O-$ and would be expected at first to have a single isotropic shift. However, it is well-known that such polymers contain small percentages of water and the commercial grade material probably contains small amounts of other compounds for commercial purposes. The non-spinning spectrum shows a broad resonance some 30-40 kHz in width having subtle inflections which may indicate overlapping resonances from the amorphous and crystalline regions of the polymer. There was also a narrow line superposed at the center.

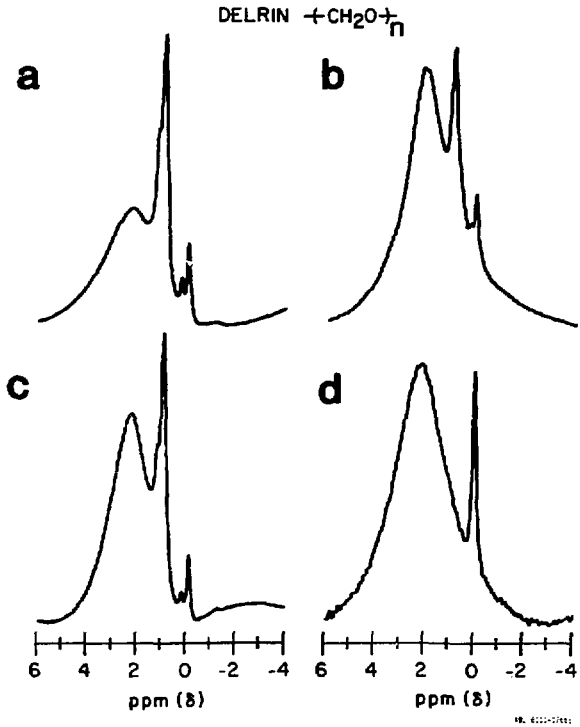

Figure 46

Proton isotropic chemical shift spectra of Delrin (DuPont) polymer. Figures a, b, and c were of one particular commercial lot while spectrum d was of another particular lot showing substantial differences. Spinning frequencies were a = 2.8 kHz, c = 4.2 kHz, and b = 5.1 kHz. Broad resonances probably result from the bulk monomer, $-CH_2O-$, while other resonances are probably due to water and commercial additives.

In Figure 46 the frequencies of sample rotation for spectra a, c, and b were 2.8, 4.2, and 5.1 kHz respectively. The intensity of the broad resonance increased approximately in proportion to the rotation frequency. The narrow resonance remained about the same at different rotation frequencies and was visible even with a few hundred Hertz rotation. These facts suggest that the narrow resonances are due to water and other commercial additives which have a very small static H_{SS}^{D} due to a high degree of molecular reorientation. The appearance of only the ±1 spinning sidebands with significant intensity indicates that the static H_{SS}^{D} of the resonance from the bulk was mostly homogeneous. The broad resonance must be due to the bulk polymer and a possible explanation for the increase of intensity with ω_r is twofold. First, the amorphous regions should have a reduced static H_{SS}^{D} with a wide distribution of correlation times for molecular motion. The narrowing by magic angle rotation is very efficient when ω_r exceeds the motional correlation time. Thus as ω_r increases, it surpasses the correlation time of an increasing fraction of the amorphous region (14). Second, the pair of protons in the monomer may be semi-isolated and have a more inhomogeneous dipolar character. The centerband intensity would then tend to increase with ω_r. Further study is required to distinguish the amorphous and crystalline regions of the polymer.

The results described above indicate that magic angle rotation can obtain useful results for hydrogen in solids when the static proton dipolar coupling is reduced. Extensive applications should also be possible in many inorganic systems. Multinuclear studies, e.g., correlation of the ^{1}H results with ^{13}C results, and heteronuclear double resonance studies should also be fruitful.

C. Observation of Dilute Spins in Solids

1. Introduction

Recent advances in NMR multiple pulse line narrowing have provided measurement of proton chemical shift tensors in solids (2). Similarly, the approach of Pines, Vega, and Mehring to obtain proton chemical shift powder patterns by isotopic dilution of protons in a deuterated solid with deuterium double quantum decoupling has been successful (22). However, the overlapping of powder patterns of chemically or crystallographically distinct sites is a serious limitation. Combination of multiple pulse methods with magic angle sample rotation has demonstrated a solution by observation of only the isotropic chemical shift (14,76). Unfortunately, the relatively small size of proton isotropic shifts has limited the resolution obtainable since the residual proton homonuclear dipole linewidth is substantial. Recent work has shown significant improvement in this situation by use of high magnetic fields to increase the absolute magnitude of the chemical shift (77). An alternative approach, as shown in Chapter III, has been to obtain isotropic chemical shift spectra of deuterium in solids. Quadrupole and dipole broadening are removed by precise magic angle spinning combined with rotation synchronized data acquisition and narrow single and double quantum resonances were observed.

In this section, high resolution proton NMR in solids is demonstrated for the general case by isotopic dilution of protons in a deuterated solid combined with magic angle spinning (78). Isotropic chemical shift spectra are obtained with greater resolution than all other methods to date. The technical difficulties of multiple rf pulse sequences and synchronous data acquisition are removed and heteronuclear rf decoupling

is not required. As described in Chapter I this is accomplished by removal of the proton homonuclear dipole coupling H_{SS}^{D} and heteronuclear dipole coupling H_{IS}^{D}. Dilution of the proton spins (S) reduces H_{SS}^{D} to a very small value. Then in the absence of the homonuclear dipole coupling H_{II}^{D} of the abundant spins (I), H_{IS}^{D} is inhomogeneous and can be spun away at the magic angle. A striking demonstration of this fact is the retrieval of ^{1}H-^{13}C J couplings in ^{13}C-MAS spectra by off resonance proton decoupling (79). For deuterium, the small gyromagnetic ratio and large quadrupole couplings cause H_{II}^{D} to be inhomogeneous, i.e., the ^{2}H-^{2}H dipole flip-flop terms are quenched, as shown in Chapter III. Thus $[H_{II}^{D}, H_{IS}^{D}] = 0$ at almost all times and magic angle spinning alone suffices to remove the effects of both even when the spinner frequency $\omega_r < \omega_{II}^{D}, \omega_{IS}^{D}$ (12).

Experiments described in this section were performed at $\omega_0/2\pi(^{1}H) =$ 361 MHz. For observation of dilute protons, a single $\pi/2$ pulse was applied followed by normal data acquisition. Spectra were taken at room temperature.

2. High Resolution Results

In Figure 47 is shown the isotropic proton spectrum of 98.8% deuterated p-di-tert-butylbenzene powder rotated about the magic axis at 3677 ± 4 Hz. The ^{1}H concentration in this sample was 1.2% of the total number of deuterons and protons. The intense line is assigned to the methyl groups with FWHM = 0.53 ppm and is arbitrarily assigned as the isotropic shift reference. The smaller resonance 6.6 ppm downfield is due to the ring protons with FWHM = 0.45 ppm. The -1 spinning sideband of the methyl line also appears at 10.2 ppm. Total accumulation time was 3.7 minutes.

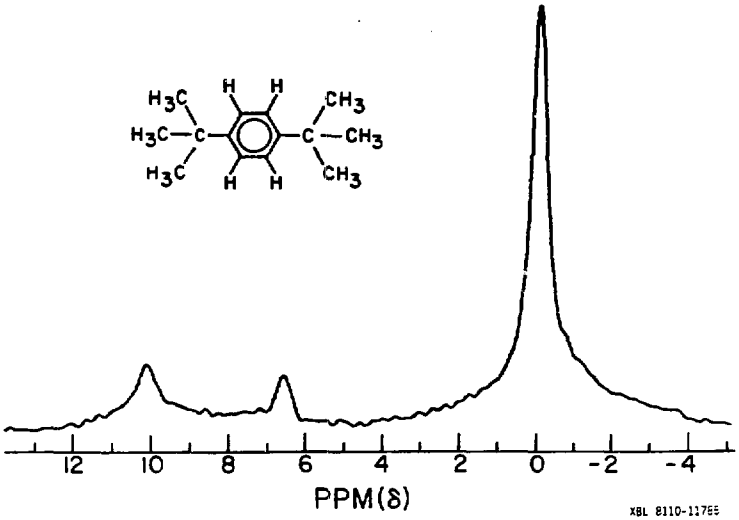

Figure 47

Isotropic chemical shift spectrum of 1.2% protons in 98.8% deuterated p-di-tert-butylbenzene solid powder. Fourier transform of fid obtained by magic angle spinning at ν_r = 3.7 kHz with a single proton $\pi/2$ pulse followed by normal data acquisition and without rf decoupling. Peak at 0 ppm is assigned to methyl groups and resonance at 6.6 ppm is due to ring protons. The -1 spinning sideband of methyl resonance appears at 10.2 ppm.

This preliminary result indicates the reasonable requirements of the experiment. The sensitivity for dilute protons is good. Since sample rotation frequencies up to 6 kHz are available, then for an isotropic shift range of 15 ppm at 361 MHz the spinning sidebands would always fall outside the isotropic spectrum. At high spinner frequency the resonance line intensity is useful, i.e., it is proportional to the number of nuclei.

In Figure 48 is shown the proton chemical shift spectrum of 98.7% deuterated diethyl terephthalate powder with $\nu_r = 3509 \pm 5$ Hz. The ^1H concentration was 1.3% of the total number of deuterons and protons. The isotropic deuterium spectrum from Figure 30 of the same sample is shown for comparison. Methyl resonances in both spectra are used as the shift reference. Resonances in the proton spectrum are assigned from up to downfield to the methyl, methylene, and aromatic protons with FWHM 0.61, 0.57, and 0.98 ppm, respectively. The ±1 spinning sidebands of each are also shown. Sample weight was 0.1 g and total accumulation time 3 minutes. The splitting of 0.40 ppm in the aromatic peak is attributed to overlapping resonances of the 2,5 and 3,6 ring positions which are crystallographically inequivalent. Thus the individual resonances have equal widths of 0.6 ppm. The downfield second order quadrupole shift of the methylene and aromatic resonances in the deuterium spectrum are clearly evident when compared to the proton spectrum. The proton resonances reflect only the isotropic chemical shift.

The presence of spinning sidebands indicates that ω_r is smaller than the width of $^1H - ^2H$ dipolar broadening or the proton chemical shift anisotropy, i.e., that ω_r is in the slow-spinning regime with respect to those couplings. Application of deuterium double quantum decoupling should remove H_{IS}^D and therefore reduce the spinning sidebands. This is

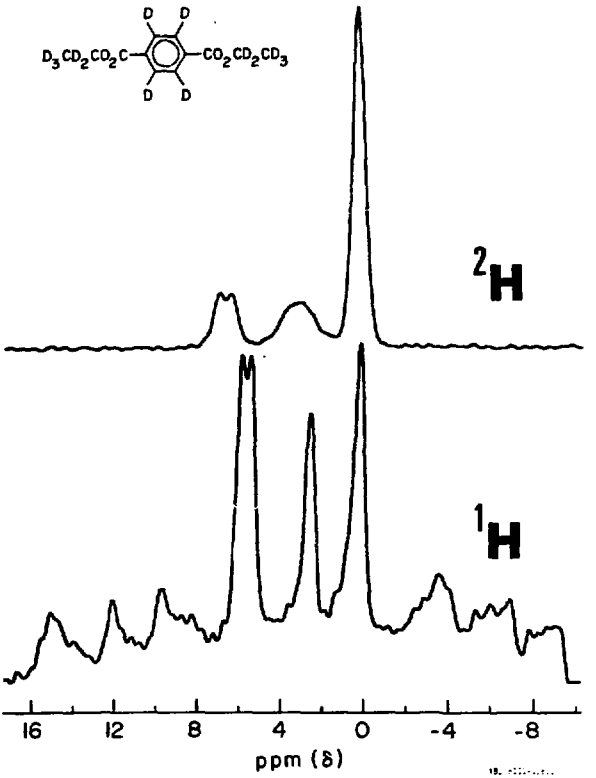

Figure 48

Isotropic high resolution proton and deuterium spectra of polycrystalline 98.7% deuterated p-diethylterephthalate. Resonances are assigned from up- to downfield to the methyl, methylene, and aromatic groups with the methyl resonances arbitrarily set at 0 ppm. Doublet in aromatic resonance is seen in both cases. Downfield second order quadrupole shift of the deuterium methylene and aromatic resonances is evident. Full width at half intensity of the proton resonances is 0.6 ppm.

demonstrated in Figure 49, the proton spectrum identical to Figure 48, with on-resonance deuterium rf irradiation. The spinning sidebands are removed, however, the resonances are slightly broadened. The decoupling is not completely efficient due to 1) small deuterium resonance offsets due to chemical shifts at high magnetic field and 2) similar orders of magnitude of the double quantum decoupling frequency, $1/t_c$ (dq-decouple) = $\omega_1^2/2\pi\omega_Q$, and the spinning frequency, ω_r. In accordance with the average Hamiltonian theory, these latter two time scales must be well separated in order that they each perform an averaging of H_{IS}^D independently. Since spinning sidebands do not usually pose a problem for the magic angle proton spectra, deuterium decoupling is not in general necessary. The complete disappearance of the sidebands upon decoupling indicates that the $^1H-^2H$ dipolar broadening is much larger than the chemical shift anisotropy broadening and that ω_r is large enough to reduce the chemical shift to its isotropic value with no sidebands.

A stringent test of resolution in solid state proton NMR is demonstrated in Figure 50, the isotropic spectrum of 93% deuterated lauric acid in polycrystalline form. The solution spectrum of the same material is shown in the inset (the carboxylic acid resonance further downfield is not shown in the inset). A reduced spinning frequency of 2248 ± 6 Hz was used to illustrate the spinning sidebands at about 7, -5 ppm and the methyl peak (a) is used as internal reference. At this level of deuteration there are about 1.7 hydrogen nuclei per molecule on the average. The distribution of hydrogen nuclei is expected to be random over the molecular sites and mass spec analysis confirm the average level of deuteration stated above and shows a small fraction of molecules having from two to a few hydrogen. The striking features in

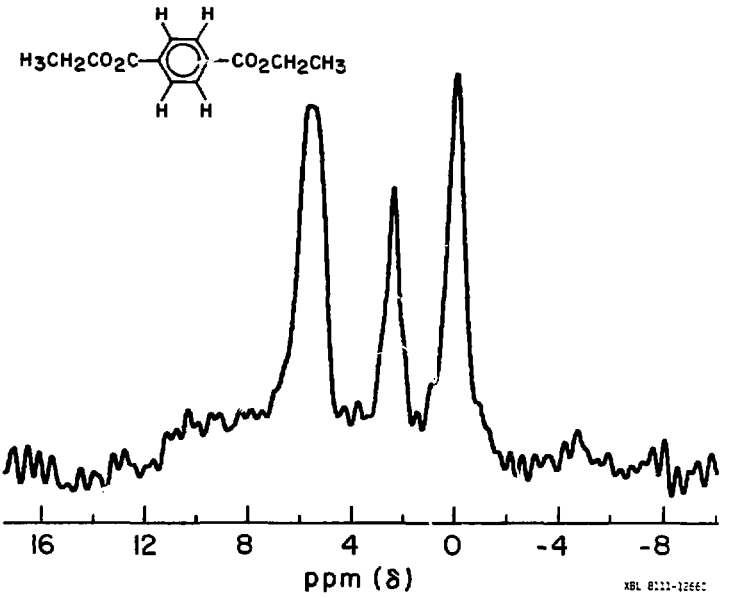

Figure 49

Isotropic proton spectrum of 98.7% deuterated p-diethylterephthalate identical to Figure 48 except with deuterium rf decoupling applied. Absence of spinning sidebands indicates that the ^{1}H-^{2}H dipolar coupling is larger than the rotation frequency and that the latter is equal to or larger than the proton chemical shift anisotropy. The deuterium decoupling leaves a small residual dipolar broadening.

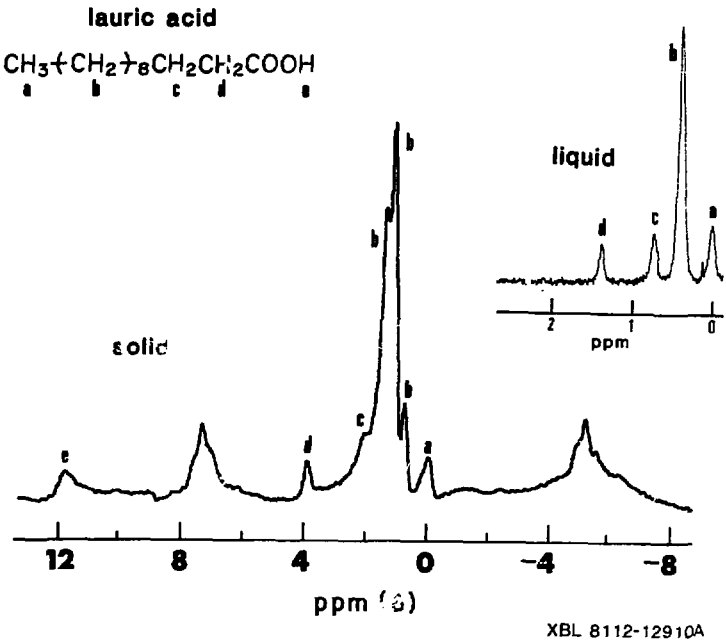

Figure 50

Isotropic high resolution proton spectrum of polycrystalline 93% deuterated lauric acid. The solution spectrum of the same material is shown in the inset (carboxylic acid solution resonance not shown). The rotation frequency of 2.25 kHz or 6.2 ppm illustrates the spinning sidebands at about 7 and -5 ppm. Methyl resonances are assigned to 0 ppm. Large differences between the solution phase and solid state isotropic chemical shifts are evident.

Figure 50 which are discussed in the following sections, are the large differences between solution and solid state chemical shifts and the resolution of possibly three distinct methylene (b) positions which are equivalent in the solution phase.

3. Resolution

The resonance linewidths of the isotropic proton spectra are determined by two main contributions. First, the residual susceptibility broadening of the rotated powder sample was discussed and demonstrated in Chapter III. Secondly, since it is not expected that ω_r can exceed $(\Delta\omega^2)^{\frac{1}{2}}_{IS}$ there may be a residual $^1H-{}^2H$ dipolar contribution resulting from the failure of $H^D_{II}({}^2H-{}^2H)$ to commute with $H^D_{IS}({}^1H-{}^2H)$ at all times as was mentioned previously. Furthermore, any residual $H^D_{SS}({}^1H-{}^1H)$ does not commute with H^D_{IS} and unless the protons are extremely diulte, e.g., less than 1%, this will also contribute a residual dipolar broadening.

The linewidths of all resonances within a particular compound, with the possible exception of the acid position in lauric acid, were found to be equal. This is expected since the susceptibility contribution is the same for all sites and the distribution of ^1H with respect to ^2H produces about the same $^1H-{}^2H$ dipolar couplings for each site.

The resonance linewidths for p-diethylterephthalate, p-di-t-butylbenzene, and lauric acid were 0.6, 0.6, and 0.3 ppm respectively. The susceptibility contributions from Chapter III for the first two compounds were 0.4 to 0.7 ppm and 0.3 ± 0.1 ppm respectively. These values suggest that the residual linewidth is due almost entirely to the susceptibility contribution.

Two further possible broadening mechanisms also exist. First, the $^1H-{}^2H$ dipolar coupling is not completely removed by magic angle rotation

due to the influence of the deuterium quadrupole coupling as was described in Chapter I. While this effect has been observed for ^{13}C and ^{31}P bonded to other quadrupolar nuclei, its effect should be negligible for $^{1}H-^{2}H$ due to the relatively high ratio of the deuterium Zeeman to quadrupole couplings. Second, the dipolar coupling even of a pair of like spins does not vanish under magic angle rotation when the chemical shift tensors of the spins do not have the same orientation in the crystal frame of reference. The residual broadening goes as $\omega_D \Delta\sigma/\omega_r$ and was demonstrated for a bonded $^{13}C-^{13}C$ pair (12). This effect should be less than 0.1 ppm in the present case due to a small ω_D for dilute protons and the relative smallness of the differences in chemical shifts for coupled protons.

4. Isotropic Chemical Shifts

In this section isotropic proton chemical shifts are reported and discussed in light of the solution and corresponding deuterium solid state shifts. The uncertainty in reported solid state shifts is taken as ±0.1 ppm for ^{1}H and ±0.2 ppm for ^{2}H, except where noted. In Chapter III it was noted and discussed that there were significant differences between solid and solution phase isotropic shifts. For the solid values reported below, a methyl resonance of the spectrum was used as internal standard. Thus the solid and liquid values are not truly referenced to the same quantity, however, any difference in methyl group shift between solid and solution phase is expected to be small.

In most cases a significant difference between solid and solution phase shifts was found. For example, the aromatic resonance shift in p-di-t-butylbenzene was found to be 6.6 ppm in the solid as compared to

5.36 ppm in solution. A complete comparison of solid and liquid shifts is summarized in Tables XIV-XVI. The differences in solid vs solution values range from 0.3 ppm (solid upfield) to -2.6 ppm (solid downfield). The remarkable differences for lauric acid, shown in Table XIV, are as yet unexplained by any single major factor. The molecules are expected to dimerize in the crystal (82), forming the usual eight-membered hydrogen bonded dicarboxyclic acid ring. A "ring current" shift effect from such a system has not been reported in the literature (83). Such an effect would give an anisotropic diamagnetic susceptibility to the crystal and a broadening of the resonances as was measured for crystals containing aromatic rings. Since the resonances were also remarkably narrow, this would seem to be an unlikely explanation. This interesting case deserves further study.

A comparison of isotropic chemical shifts for p-diethylterephthalate is shown in Table XV. The solid state shifts for ^{1}H and ^{2}H agree within their combined uncertainty and the splitting of the aromatic resonance due to rigid molecular conformation is seen in both cases. The values of the downfield second order quadrupole shift for ^{2}H taken directly from Figure 48 agree with the theoretical values reported in Chapter III; experimental second order shifts for the methylene and aromatic resonances were 0.41 and 0.80 ppm respectively while the theoretical values were 0.55 and 0.73 ppm respectively. The good agreement here between ^{1}H and ^{2}H chemical shifts and in the further data below strongly indicates that any isotope effect in the solid state is negligible. This fact has been reported in the literature (84) and the precision of the data presented here is an order of magnitude greater than previous comparisons of $^{1}H/^{2}H$ solid state chemical shifts.

TABLE XIV: Proton chemical shifts for lauric acid (ppm).

Position[1]	Sadtler[2]	Aldrich[3]	solution[4]	solid[5]
methyl (a)	0	0	0	0
methylene (b)	0.40	0.38	0.42	0.8 1.2 1.4
β-methylene (c)	0.71	0.91	0.75	2.2
α-methylene (d)	1.44	1.47	1.41	4.0
carboxylic (e)	10.07	—	11.32	11.8

1. See Figure 50. Methyl resonance used as internal reference.
2. Reference (80).
3. Reference (81).
4. 93%-deutero lauric acid in $CDCl_3$.
5. Neat powder 93%-deutero lauric acid.

TABLE XV: Isotropic chemical shifts for p-diethylterephthalate (ppm).

Position[1]	solution[2] ^1H	dilute-mas (solid) ^1H	^2H-mas (solid) ^2H
methylene	2.97	2.4	2.3
aromatic	6.71	5.3	5.6
		5.7	6.0

1. Methyl resonance used as internal reference.

2. In $CDCl_3$.

TABLE XVI: Isotropic chemical shifts for 4,4'-dimethylbenzophenone (ppm.)

Position[1]	Sadtler[2] (solution) ^1H	mp-mas[3] (solid) ^1H	dilute-mas (solid) ^1H	^2H-mas (solid) ^2H
center of aromatic resonances	5.06	4.9	5.6[4]	5.3[5]
aromatic splitting	0.44[6]	1.4	1.5	1.6

1. Methyl resonance used as internal reference.
2. Reference (81).
3. Reference (76). Obtained on fully protonated compound by combined multiple pulse and magic angle spinning.
4. Lineshape distorted.
5. Doublet with 1.0 ppm splitting observed for methyl resonance; center of doublet used as internal reference.
6. Difference between ortho and meta shifts.

A comparison of isotropic chemical shifts for 4,4'-dimethylbenzophenone is shown in Table XVI. Shifts obtained by combined multiple pulse line narrowing and magic angle rotation (76) are also given. The solid and solution phase shifts are nearly the same in this case. However, in the solution the four ortho ring positions are equivalent as are the four meta ring positions due to free rotation about single bonds. In the solid, two aromatic resonances with approximately 3 to 1 intensity ratio were observed for both ^{1}H and ^{2}H (see Fig. 32). An explanation for this splitting, given by Ryan et al. (76), is that the splay of the aromatic rings in the solid places two of the ortho positions above and near the aromatic rings so that they experience a 1.5 ppm downfield shift relative to the other six ring positions. This situation agrees with the results presented here. However, the 4,4'-methyl groups are not necessarily magnetically equivalent (85) and a 1.0 ppm split doublet was observed for the methyl resonance in the deuterium spectrum. Such a splitting was not reported in Reference 76, but the methyl resonance there was broader than the aromatic resonances which suggests the possibility of unresolved shifts. Unfortunately, the spectrum obtained here for dilute protons was distorted due to a technical problem and the methyl resonance lineshape was not reliable.

5. Discussion

a. Comparison of High Resolution Methods

In this section a brief comparison of methods to obtain $^{1}H/^{2}H$ chemical shift information is made. There are three approaches to obtain the full chemical shift tensor. First, multiple pulse line narrowing sequences can be applied to fully protonated materials. In the

general case of large proton homonuclear dipolar coupling the residual dipolar broadening is substantial and limits the precision of measurement of the tensor components. Second, dilute protons in a deuterated solid may be observed with deuterium double quantum decoupling. Very well defined powder patterns may be obtained. For semi-dilute protons a third approach combines multiple pulse and deuterium decoupling methods. This has not been demonstrated in the literature to date and is limited by the ability to produce largely different cycle times, t_c, for the two methods simultaneously. All the above methods are limited for powder or amorphous samples to systems with one distinct site by the overlapping of powder patterns for multicomponent systems.

Thus it is useful to reduce the chemical shift tensor to its isotropic average and attempt to resolve all distinct sites. This is done by magic angle sample spinning. There are four general approaches to obtain the isotropic spectrum; 1) observation of ^1H with combined multiple pulse and magic angle spinning on fully protonated solids, 2) observation of single quantum ^2H spectra with magic angle spinning, 3) observation of double quantum ^2H spectra with magic angle spinning, and 4) observation of dilute ^1H by magic angle spinning. Since the $^1H/^2H$ isotropic shift range is some 15 ppm for most systems it is crucial to obtain the narrowest resonances possible.

The first method, multiple pulse magic angle rotation, has an advantage in not requiring the use of isotopic substitution, but has several technical and theoretical drawbacks. It requires high power, fast response rf sample probe designs and careful control and production of the rf pulse sequences. Aside from susceptibility effects which are common to all experiments, the resolution is determined by a) scaling

down of the chemical shift by a factor of $3^{-\frac{1}{2}}$, b) unresolved $^1H-^1H$ J couplings, and c) the residual proton dipolar broadening. Resonance linewidths in typical organic molecular solids such as those studied in this work are 1-2 ppm with respect to the reduced chemical shift scale in the best case and several ppm when the most advanced technology is not available. The residual broadening is mainly dipolar and is largely independent of magnetic field strength, but its relatively large magnitude makes use of a high magnetic field necessary to increase resolution.

The second and third methods involve observation of single and double quantum deuterium resonances and were demonstrated in detail in Chapter III. Aside from magic angle rotation which is common to all the isotropic methods, the technical requirements here are modest. Typical linewidths are in the range 0.7 to 1.4 ppm for low levels of deuteration at B_0 = 42 kG and as much as 0.5 ppm less at higher field strengths.

The observation of dilute protons affords the highest resolution and technological ease. Results demonstrated above indicate that linewidths of 0.3 to 0.6 ppm can be expected at 85 kG. This is due mainly to susceptibility broadening and thus the resolution has a reduced dependence on magnetic field strength.

b. Conclusion

The results demonstrated in this chapter offer high resolution proton NMR of solids with resolution limited almost entirely by susceptibility broadening. While the effects of the latter may be reduced by the use of single crystal samples, the practical utility of such an approach is very limited in scope and it is simply not possible for a wide variety of heterogeneous or noncrystalline solids. From an overall viewpoint, therefore, the limit of isotropic high resolution NMR of hydrogen/deuterium in the solid state has been attained.

Appendix A: Average Hamiltonian and Quadrupole Effects for Spins S = 1

In this section the average Hamiltonian calculation for dipolar coupled spins I=1 under magic angle rotation is given. Since the chemical shift and J couplings are expected to be simply averaged to their isotropic values, they are excluded from the equations for simplicity. The relevant Hamiltonian for a pair of spins I=1 is

$$\mathcal{H} = \mathcal{H}_Z + \mathcal{H}_Q + \mathcal{H}^D_{SS} + \mathcal{H}^D_{IS}$$
$$= \mathcal{H}_Z + \mathcal{H}_{int} \qquad \text{A-1}$$

The zeroth order average due to the Zeeman interaction is

$$\bar{\mathcal{H}}^{(0)} = H_Q + H^D_{SS} + H^D_{IS} \qquad \text{A-2}$$

which contains only the "secular" terms

$$H_Q = \frac{1}{24}\frac{e^2qQ}{I(2I-1)}(3\cos^2\beta-1)(3S_0^2 - \underset{\sim}{S}\cdot\underset{\sim}{S})$$

$$H_{SS} = -\frac{1}{2}\hbar\gamma_S^2 r_{SS}^{-3}(3\cos^2\Theta_{SS}-1)(3S_0^iS_0^j - \underset{\sim}{S}^i\cdot\underset{\sim}{S}^j)$$

$$H_{IS} = -\hbar\gamma_I\gamma_S r_{IS}^{-3}(3\cos^2\Theta_{IS}-1)S_0I_0 \qquad \text{A-3}$$

Since H_Q is by far the largest term, it may be considered alone for its effect on spectral lineshape and frequency. The first order correction from the Zeeman averaging is in the form of Eq. I-28. The time dependent terms are

$$H_Q^2 = A_2\, e^{i2\omega_0 t}\, S_{+1}^2$$

$$H_Q^1 = A_1\, e^{i\omega_0 t}\,(S_{+1}S_0 + S_0S_{+1})$$

$$H_Q^0 = A_0(3S_0^2 - S^2)$$

$$H_Q^{-1} = A_{-1}\, e^{-i\omega_0 t}\,(S_{-1}S_0 + S_0S_{-1})$$

$$H_Q^{-2} = A_{-2}\, e^{-i2\omega_0 t}\, S_{-1}^2 \qquad \text{A-4}$$

where $e^{i\omega_0 I_0 t} S_{\pm 1}\, e^{-i\omega_0 I_0 t} = S_{\pm 1}\, e^{\pm i\omega_0 t}$

and

$$A_2 = \sin^2\beta\, e^{-2i\alpha}$$

$$A_1 = \sin 2\beta\, e^{-i\alpha}$$

$$A_0 = 3\cos^2\beta - 1$$

$$A_{-1} = \sin 2\beta\, e^{i\alpha}$$

$$A_{-2} = \sin^2\beta\, e^{2i\alpha} \qquad \text{A-5}$$

From Eq. I-28 there will be twenty terms to integrate. Using the expressions

$$\int_0^{2\pi/\omega_0} dt_2 \int_0^{t_2} e^{\pm in\omega_0 t_2}\, e^{\pm in\omega_0 t_1}\, dt_1 = 0$$

$$\frac{-i\omega_0}{4\pi} \int_0^{2\pi/\omega_0} dt_2 \int_0^{t_2} e^{\pm in\omega_0 t_2}\, dt_1 = \mp \frac{1}{2n\omega_0} \qquad \text{A-6}$$

the result is

$$\bar{\kappa}^{(1)} = -\frac{A_0}{\omega_0}\,[A_1[S_1,S_0] + A_{-1}[S_0,S_{-1}] + \tfrac{1}{2}A_2[S_2,S_0] + \tfrac{1}{2}A_{-2}[S_0,S_{-2}]\} \qquad \text{A-7}$$

where the S are the spin operator terms from Eq. A-4. The

completed result is given in Reference 12 by evaluation of the commutators in Eq. A-7 and diagonalizing the resulting $\bar{\mathcal{H}}^{(1)}$.

As mentioned in Ch. I, the small quadrupole coupling and relatively high ratio of $\mathcal{H}_Z/\mathcal{H}_Q$ allows use of the standard time independent perturbation theory. The second order term is (86)

$$\omega - \omega_0 = \frac{1}{8}\frac{\omega_Q^2}{\omega_0}(1 + 2\cos^2\Theta - 3\cos^4\Theta) \qquad \text{A-8}$$

for the non-spinning case where Θ is the angle between V_{ZZ} and Z(LAB). The analytic solution gives the lineshape function

$$I_{\pm}(x) = \{\pm[4/9 - x]^{1/2} + 1/3\}^{-1/2}\,[4/9 - x]^{-1/2} \qquad \text{A-9}$$

where the ± refers to the two deuterium single quantum transitions, $x = \frac{8}{3}\frac{\Delta\omega\,\omega_0}{\omega_Q^2}$, and the domain of x is given by

$$I_+(x) : 0 \le x \le 4/9$$

$$I_-(x) : 1/3 \le x \le 4/9 \qquad \text{A-10}$$

This lineshape is depicted in Fig. 7a. Under magic angle rotation the result is

$$\omega - \omega_0 = 4/3C \cdot (1/3C)(1/2 + 3\cos^2\beta' - 7/2\cos^4\beta')$$

$$x = 6/7\,\frac{1}{C}(\Delta\omega - 4/3C)$$

$$I_{\pm}(x) = \{\pm[x + 16/49]^{1/2} + 3/7\}^{-1/2}\,[x + 16/49]^{-1/2}$$

$$I_+(x) : 0 \ge x \ge -16/49$$

$$I_-(x) : -1/7 \ge x \ge -16/49 \qquad \text{A-11}$$

where $C = \frac{1}{8}\omega_Q^2/\omega_0$. This lineshape is depicted in Fig. 7b. The broadening and shift given in Ch. 1 are taken from the singular peaks of the lineshape in Fig. 7b.

For magic angle rotation slightly off the magic axis the first and second perturbation theory terms may be added together to calculate the lineshape. As demonstrated in Ch. III, these terms can be made negligible and good resolution obtained at the magic angle. A complete calculation of the combined first and second order terms has been performed, however, the cumbersome details will not be given. For instance, the lineshape function has the form

$$I(x) = \{\pm[x + D^2/4]^{1/2} - D/2\}^{-1/2}\,[x + D^2/4]^{-1/2}$$

$$x = \frac{1}{E}(\Delta\omega - C \pm \tfrac{1}{2}AB - C\sin^2\beta + \tfrac{9}{8}C\sin^4\beta)$$

$$A = 3\cos^2\beta - 1$$

$$B = \frac{1}{2}\omega_Q$$

$$C = \frac{1}{8}\omega_Q^2/\omega_0$$

$$D = \frac{1}{E}\left[A(\pm\tfrac{3}{2}B + C) - 9C\sin^2\beta + \tfrac{45}{4}C\sin^4\beta\right]$$

$$E = C(\tfrac{45}{4}\cos^2\beta - \tfrac{105}{8}\cos^4\beta - \tfrac{9}{8}) \qquad \text{A-12}$$

Experimental verification of such lineshapes has been found (87) and similar analytic calculations have been previously performed (88) and may have applications for nuclei with larger $\mathcal{H}_Q/\mathcal{H}_Z$ and in electron spin resonance spectroscopy.

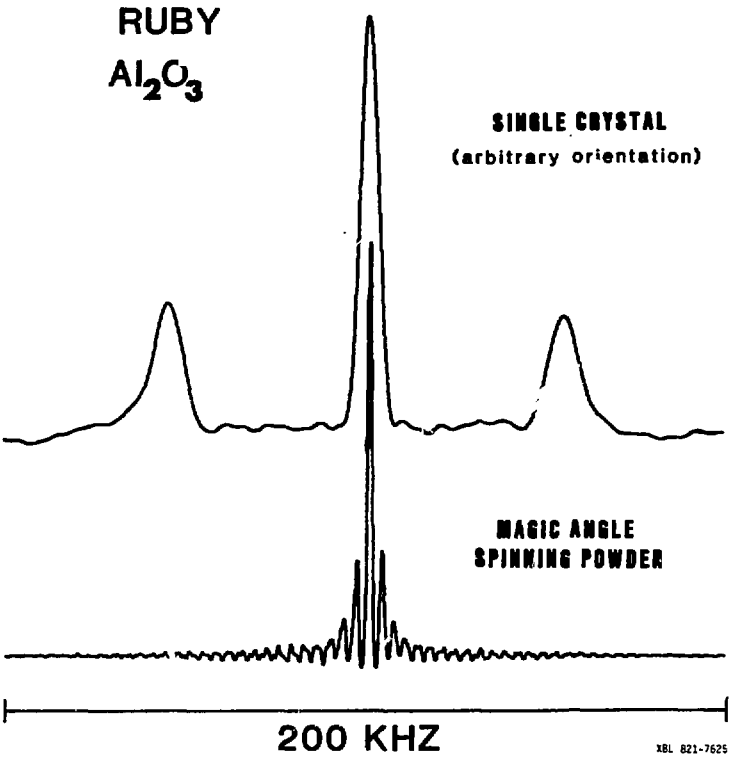

Figure 51

Single crystal spectrum and powder spectrum under magic angle rotation of ^{27}Al in ruby. Top: Central transition and first satellites of the spin 5/2 ^{27}Al spectrum of a ruby single crystal lie within spectrometer bandwidth. Bottom: Narrowed central transition and spinning sidebands for magic angle rotation of polycrystalline ruby.

For NMR nuclei with half integral spin greater than 1, the form of the calculation is the same in both the average Hamiltonian and perturbation theory cases. Again, the algebra is cumbersome, especially when the assymetry in non-zero, and will not be repeated here. Multiple pulse line narrowing (23) and magic angle rotation (87, 89) have been applied to this case. The basic principles are the same as outlined in Ch.'s I and III and are demonstrated in Figure 51, the spectra of ^{27}Al in ruby. The spin $I = 5/2$ ^{27}Al nucleus exhibits a quintet (see Fig. 4) in the single crystal of which only the inner satellites are seen in Fig. 51. The central transition and sidebands due to the quadrupole satellites are seen to be narrowed under magic angle rotation at 3.1 kHz. The central transition linewidth is reduced from 6.0 kHz to 1.3 kHz. The comments made in Ch. I with regard to ^{14}N and large ω_Q also apply to the present case since it is desirable to reduce second order quadrupole broadening further than that obtained by sample rotation alone.

A further problem encountered in Ch. I is the many higher order terms in Eq. I-37, 38 involving the dipolar coupling between spins $I = 1$. First, it is assumed that any heteronuclear dipolar coupling, H_{IS}^D in Eq. A-2, can be removed by r.f. decoupling. The larger quadrupole coupling induces a time-dependence in H_{SS}^D in the average Hamiltonian formalism and a zeroth order average of H_{SS}^D can be calculated. When the quadrupole splitting, Ω_Q, of the two spins i, j are equal or equal and opposite, then $t_c = 2\pi/\omega_Q$ and the zeroth order average of H_{SS}^D in the fictitious spin - $\frac{1}{2}$ basis is

$$\overline{H_{SS}^{D}(0,0)} = b_{ij}\,[8S_{zi}^{13}S_{zj}^{13} - (S_{+i}^{12}S_{-j}^{12} + S_{-i}^{12}S_{+j}^{12}) - (S_{+i}^{23}S_{-j}^{23} + S_{-i}^{23}S_{+j}^{23})]$$

or

$$\overline{H_{SS}^{D}(0,0)} = b_{ij}[8S_{zi}^{13}S_{zj}^{13} - (S_{+i}^{12}S_{-j}^{23} + S_{-i}^{12}S_{+j}^{23}) - (S_{+i}^{23}S_{-j}^{12} + S_{-i}^{23}S_{+j}^{12})] \qquad \text{A-13}$$

where the zeroth order average is taken first due to $\mathcal{H}_z$, then H_Q, and $b_{ij} = \frac{-1}{2}\hbar\gamma_S^2 r_{SS}^{-3}(3\cos^2\Theta_{SS}-1)$. The flip-flops terms represent mutual single quantum flips of the two deuterons. This is the first order resonant process mentioned in Ch. III and invoked in the crossing argument for the rotating sample. It is essentially the same as for spins $S = \frac{1}{2}$ and the usual spin temperature theory may be used to describe the cross relaxation.

When the quadrupole splittings of the two spins i, j are unequal, it is assumed that $\omega_{Q,i} = (m/n)\omega_{Qj}$ so that an unambiguous and cyclic propagator and cycle time may be defined in terms of $\omega_{Q,i}$. In that case $\overline{H_{SS}^{D}(0,0)}$ vanishes upon integration and $\overline{H_{SS}^{D}(0,1)}$ must be calculated. This is the higher order process mentioned in Ch. III. The relevant integral for $\overline{H_{SS}^{D}(0,1)}$ contains 80 non-trivial terms; 16 terms involve commutators such as $[S_{z,i}^{13}S_{z,j}^{13}(t_1),(S_{+,i}^{12}S_{-,j}^{12} + S_{-,i}^{12}S_{+,j}^{12})(t_2)]$ etc., and 64 terms involve commutators such as

$$[(S_{x,i}^{12}S_{x,j}^{12} + S_{y,i}^{12}S_{y,j}^{12})(t_1),(S_{x,i}^{23}S_{x,j}^{23} + S_{y,i}^{23}S_{y,j}^{23})(t_2)]$$

$$= -(S_{+,i}^{13}S_{-,j}^{13} + S_{-,i}^{13}S_{+,j}^{13}) \qquad . \qquad \text{A-14}$$

This latter term represents 1-3 or double quantum transitions and suggests a fundamentally new process; the diffusion of spin magnetization in solids by multiple quantum transitions (90). To calculate

$\overline{H_{SS}^{D}}(0,1)$, the form is

$$\omega_{Q,i} = (m/n)\omega_{Q,j}$$

$$p = mn$$

$$t_c = 4p\pi/3\omega_Q \qquad \text{A-15}$$

and a non-zero spatial integral for the term in Eq. A-14 becomes

$$\frac{i3\omega_{Q,i}}{8p\pi} \int_0^{4p\pi/3\omega_{Q,i}} dt_2 \int_0^{t_2} \sin[(3/2)\omega_{Q,i}(\tfrac{m}{n} \pm 1)t_2]$$

$$\times \cos[(3/2)\omega_{Q,i}(\tfrac{m}{n} \pm 1)t_1]\, dt_1$$

$$= (i/6)(\omega_{Q,i} \pm \omega_{Q,j})^{-1} \qquad . \qquad \text{A-16}$$

When $\omega_{Q,i}$ approaches $\omega_{Q,j}$, then the integral of Eq. A-16, for terms depending on $(\omega_{Q,i} - \omega_{Q,j})^{-1}$, tends to infinity. This corresponds to ever larger values of p and t_c and the first order process becomes resonant. The result is that

$$\overline{H_{SS}^{D}}(0,1) \propto \omega_{SS}^2/(\omega_{Q,i} \pm \omega_{Q,j}) \qquad \text{A-17}$$

where ω_{SS} is the magnitude of the dipolar coupling.

In conclusion, this result suggests that spin diffusion by double quantum flips can occur between dipolar coupled spins with

$S = 1$ even when $\omega_{Q,i} \neq \omega_{Q,j}$. Further work is necessary to measure the cross relaxation rate under that condition in a crystal. Also, the first order average Hamiltonian with respect to the Zeeman representation, $\bar{H}_{SS}^{D}(1,0)$, was neglected. This correction is of order $\omega_Q \omega_{SS} / \omega_0$ and may be important when ω_{SS} is relatively large. Finally, the reduced first order single quantum spin diffusion rate in the rotating sample could be calculated by numerical methods based on the model presented in Ch. III.

Appendix B: High Speed Turbine NMR Probe with Tachometer and Spectrometer Synchronization Interface.

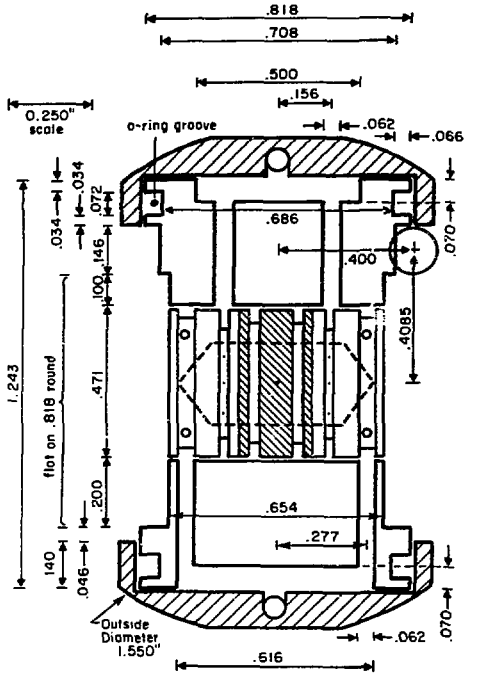

Notes: (1) Use Parker 2-17 VITON o-ring (1/16") for cradle.
(2) Cradle threads are 6-32.

XBL 821-7508

Figure 52

Cylindrical spinner probe cradle cross section.

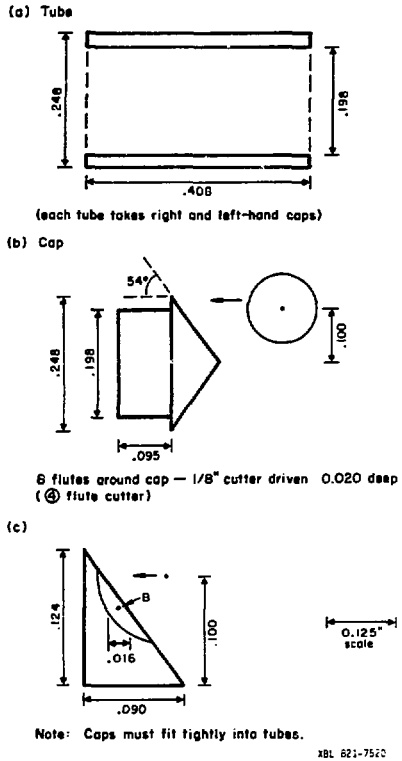

Figure 53

Sample spinner cylinder and caps.

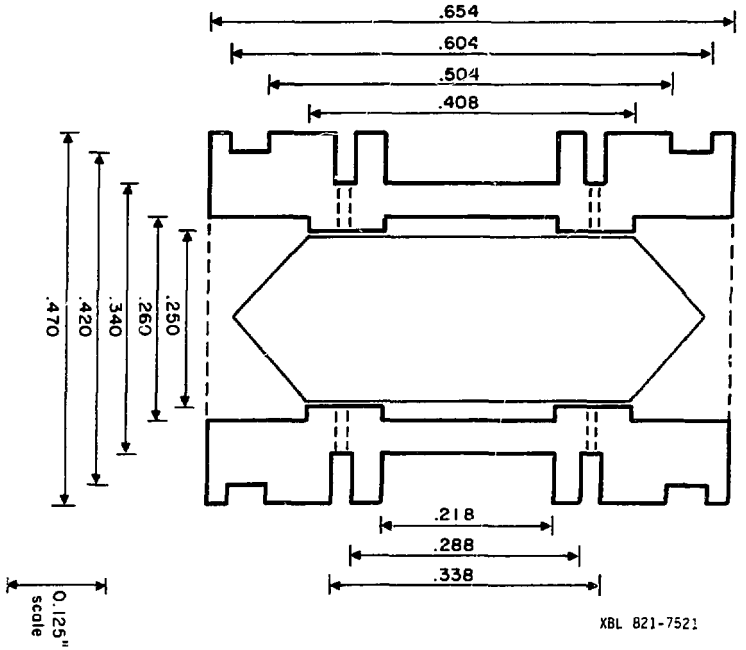

Figure 54

Stator.

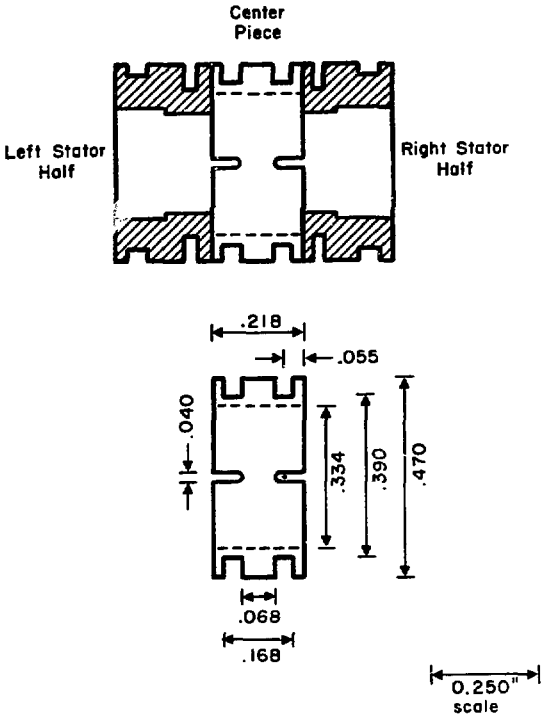

Figure 55

Stator.

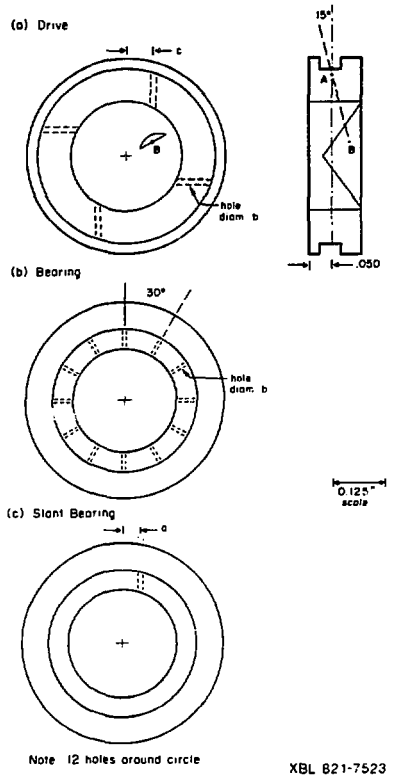

Figure 56

Stator gas bearing and drive jets.

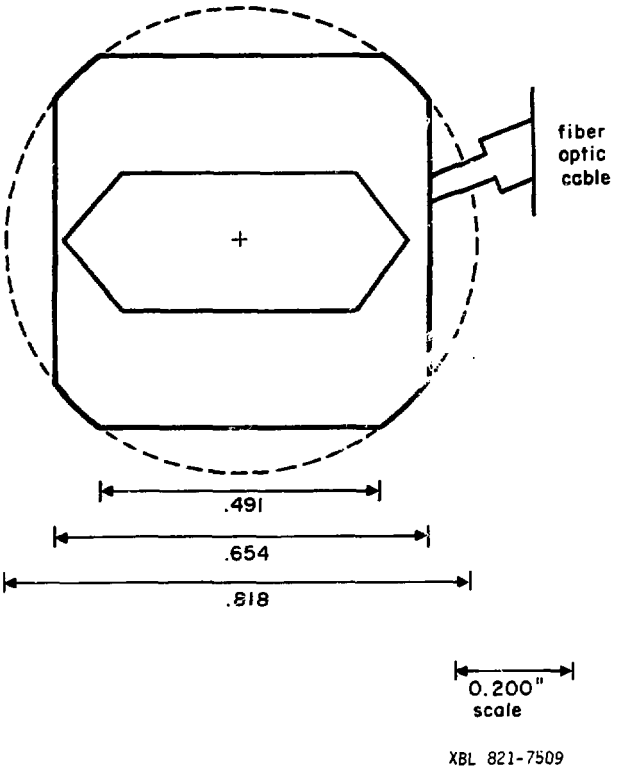

Figure 57

Dimensions for cradle faces.

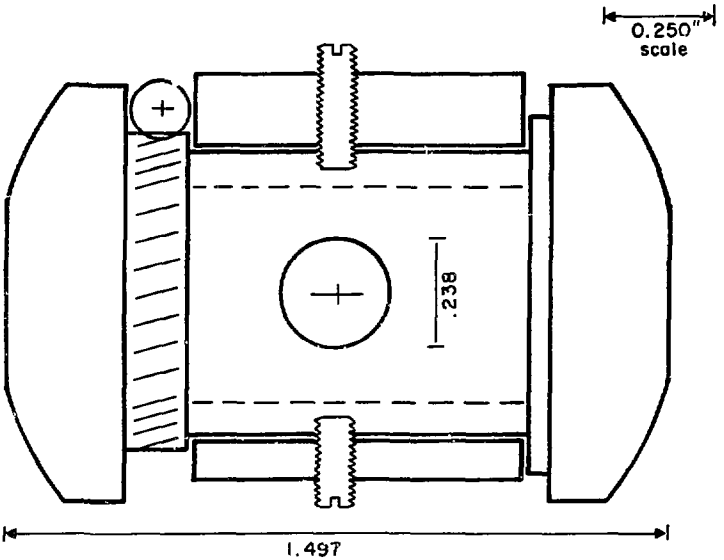

XBL 821-7511

Figure 58

Access hole.

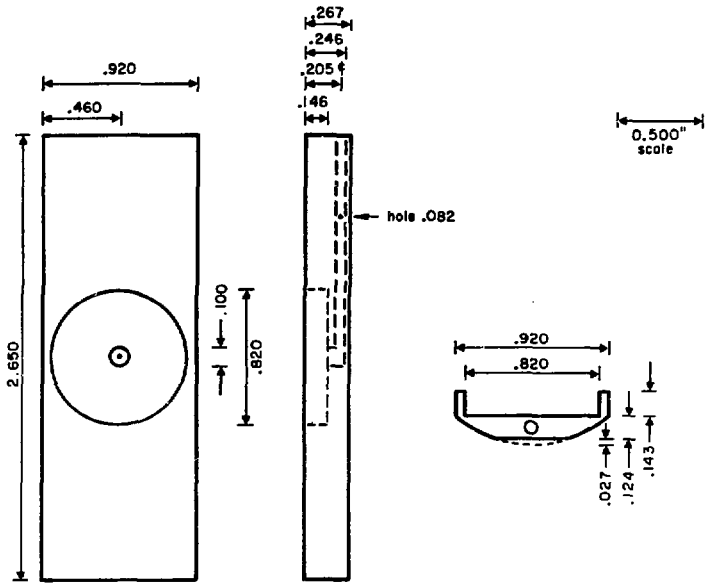

Note: Not shown are threaded holes for mount screws.

XBL 821-7511

Figure 59

Side plates.

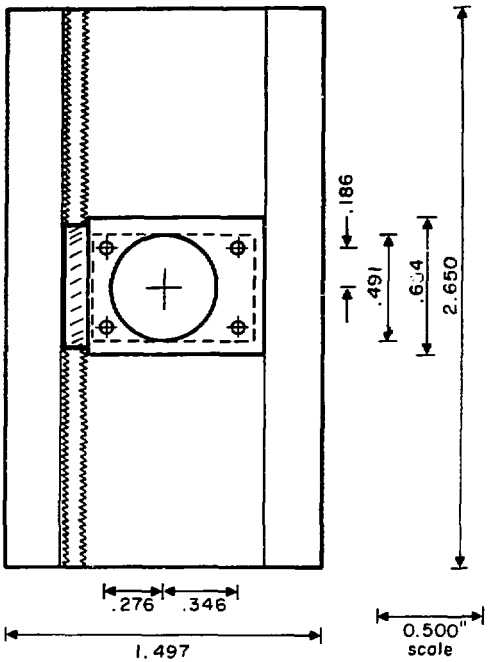

Note: 0-80 roundhead brass threaded in 1/4".

XBL 821-7512

Figure 60

Cover plate mount.

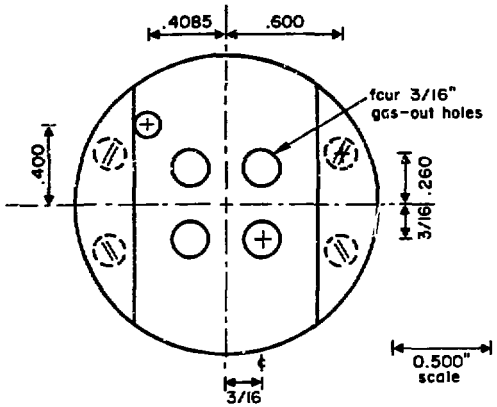

Top View

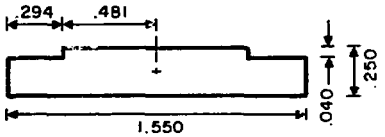

Side View

Note: 2-56 flathead brass, countersunk on bottom.

XBL 821-7514

Figure 61

Bottom plate.

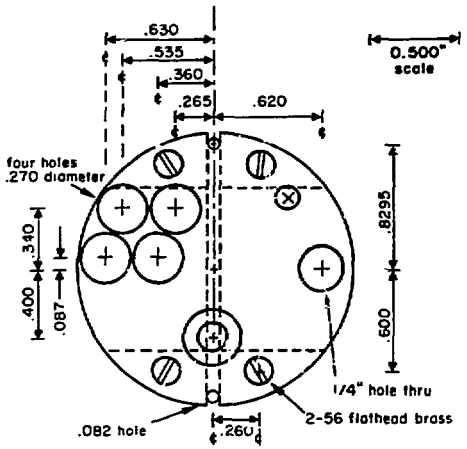

Note: Grind off flange on transfer line to minimum.

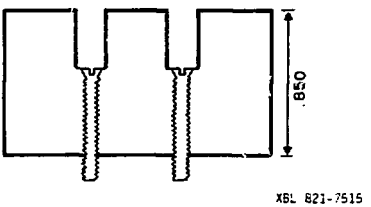

Figure 62

Top plate.

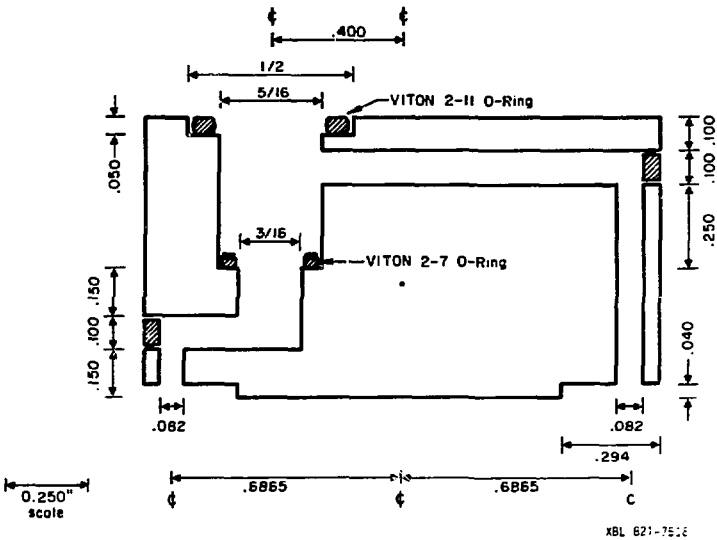

Figure 63

Top plate.

(a) Cover Plate (.100 thickness)

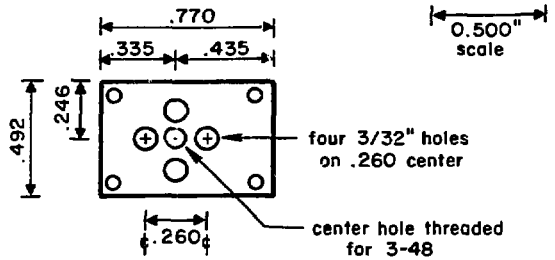

(b) Fiber Plate (.180 thickness)

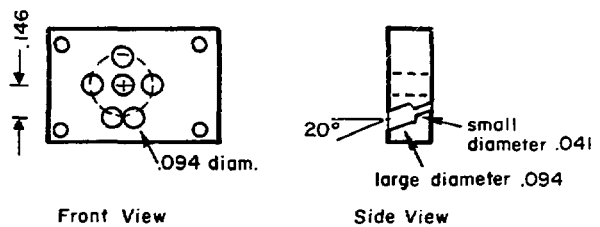

XBL 821-7513

Figure 64

Cover plates.

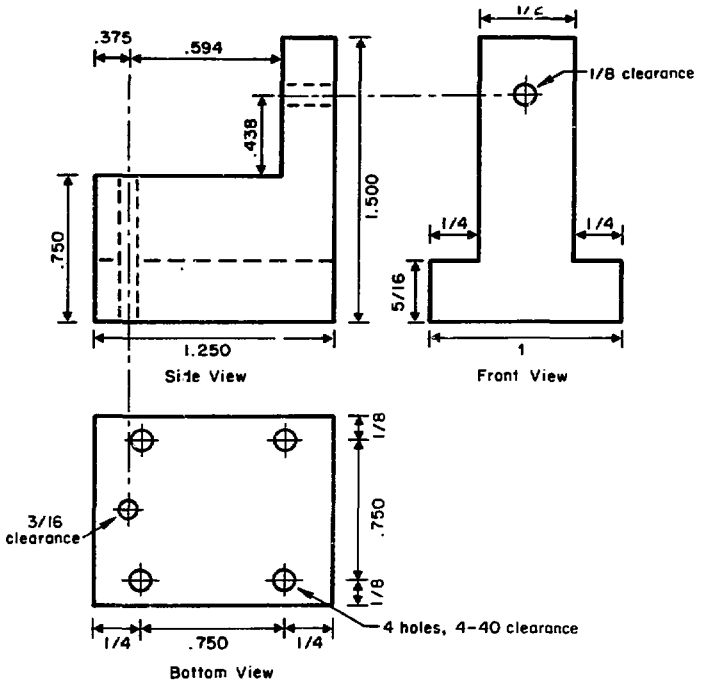

Note: Boston Gear G479Y-G, G479Y-P

XBL 821-7516

Figure 65

Cradle gear drive.

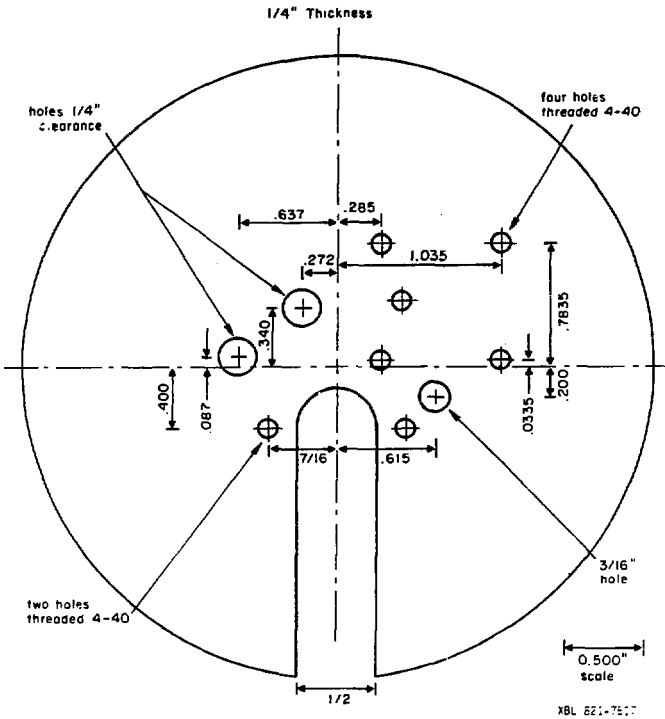

Figure 66

Probe body plate.

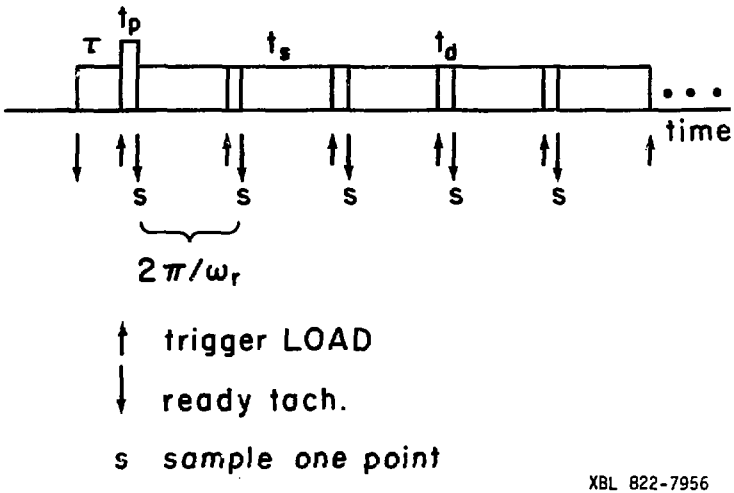

Figure 67

Timing diagram for pulse programmer synchronization with respect to sample rotation. The experiment may be initiated and synchronized with the sample rotation.

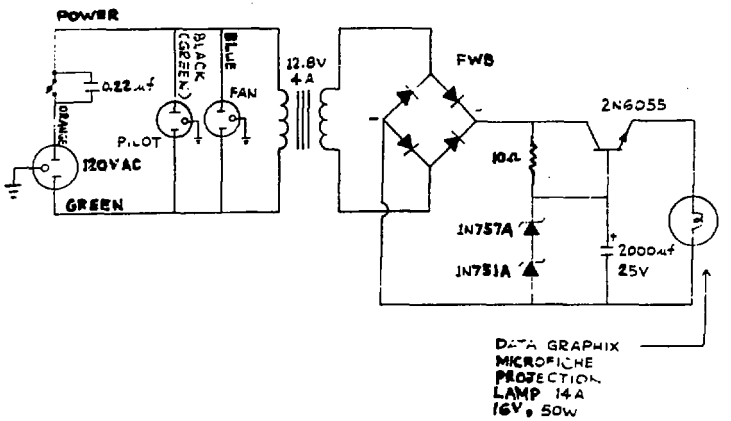

Figure 68

Tachometer power supply.

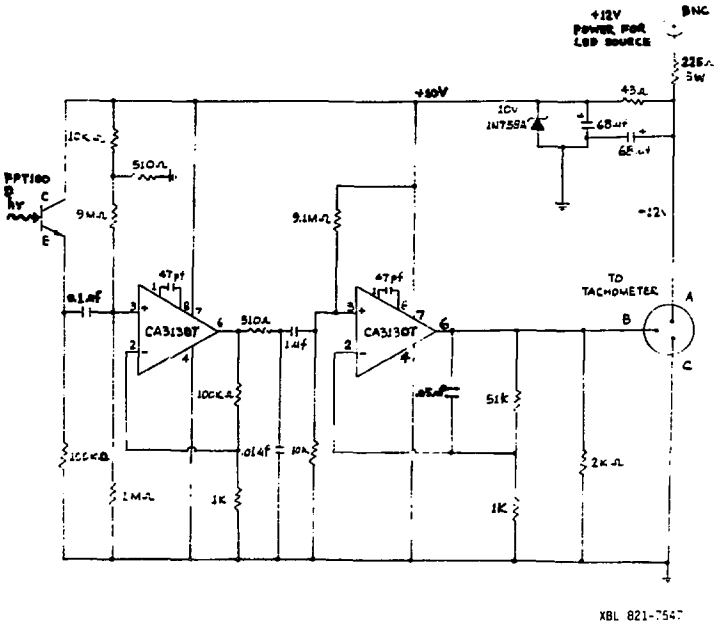

Figure 69

Tachometer preamplifier.

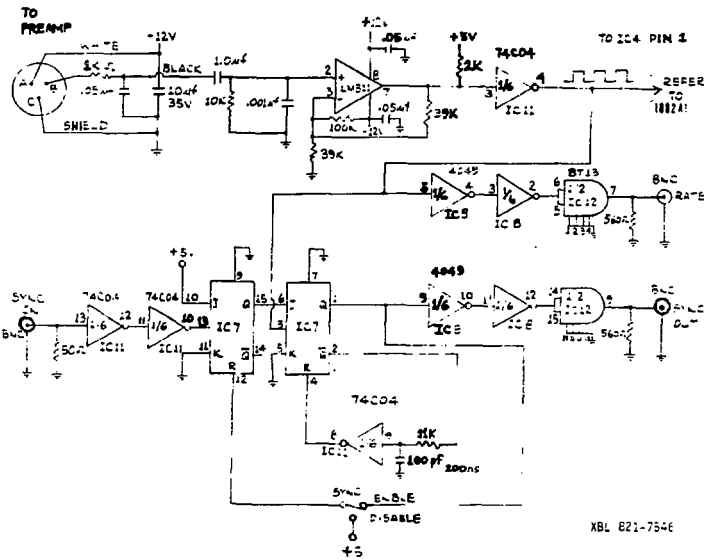

Figure 70

Tachometer synchronization logic.

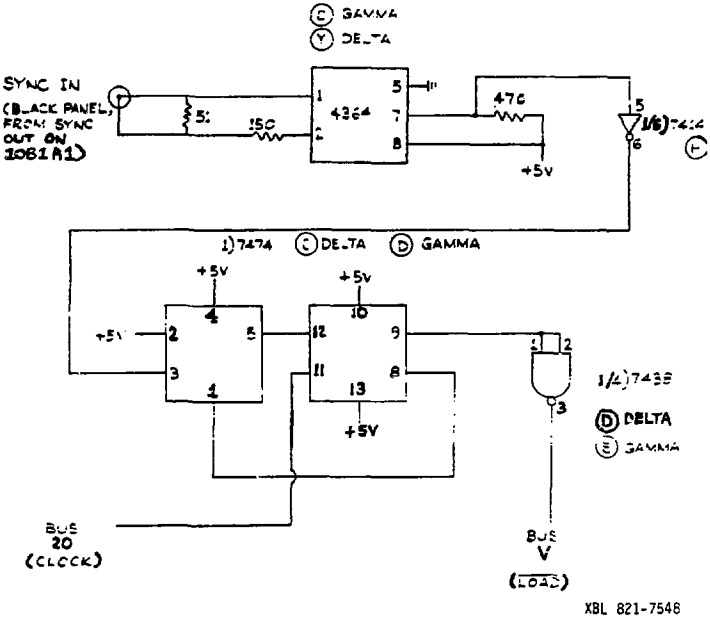

Figure 71

Pulse programmer tachometer interface.

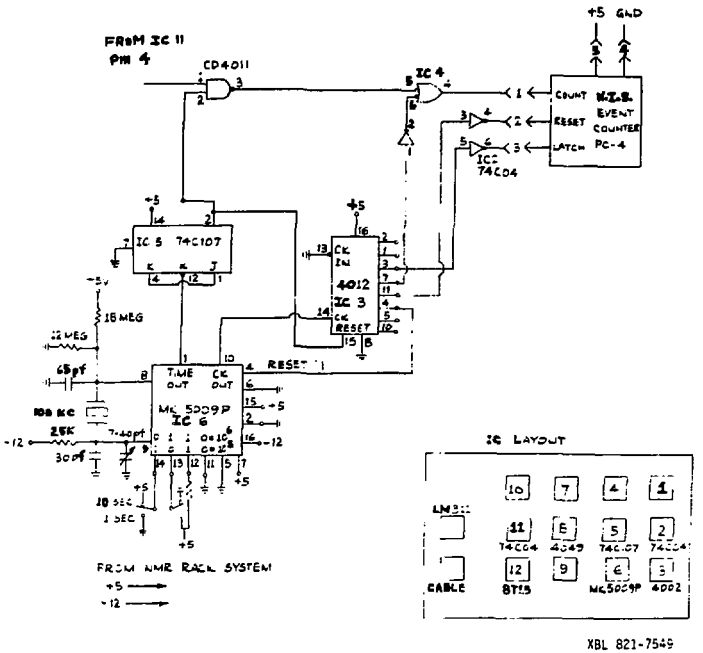

Figure 72

Tachometer display counter circuit.

Appendix C: Pulse Programs

MAS WITH SYNCHRONOUS SAMPLING

```
01 BR 06 07
02 BR 06 07
03 BR 06 07
04 BR 06 07
06 OF A0 A0
08 PA 00 00
10 SE 02 A2
12 CO 02 D8
14 BR 32 05
16 SE 02 A0
18 OF D4 E0
1A IN 02 A2
1C CO 02 DA
1E BR 18 02
20 SE 02 A0
22 SE 04 A0
24 OF C4 A0
26 IN 04 A2
28 CO 04 B0
2A BR 24 02
2C IN 02 A2
2E CO 02 B2
30 BR 22 02
32 OF A0 E4
34 PA 01 00
36 OF D0 E0

70 PA 00 00
72 SE 02 A0
74 OF C4 E8
76 IN 02 A2
78 CO 02 B6
7A BR 74 02
80 SE 02 A0
82 CO 02 BA
84 BR 94 05
86 IN 02 A2
88 SE 04 A0
8A OF C4 A0
8C IN 04 A2
8E CO 04 A6
90 BR 8A 02
92 BR 82 07
94 HA 00 00
A0 SE 02 A0
A2 PA 01 00
A4 R1 00 00
A6 01 D2 E2
A8 01 D6 E6
AA IN 02 A2
AC CO 02 B4
AE BR A6 02
B0 PA 00 00
B2 01 D2 E2
B4 HA 00 00
```

ROTATIONAL ECHOES

```
01 BR 10 07
02 BR 10 07
03 BR 10 07
04 BR 10 07
10 PA 00 00
12 OF A0 A0
14 OF A0 E4
16 OF D0 E0
18 OF D6 E6
60 SE 02 A2
62 PA 01 00
64 OF D2 E2
66 OF D2 E2
68 IN 02 A2
6A CO 02 B8
6C BR 64 03
6E PA 00 00
80 SE 02 A0
82 CO 02 B6
84 BR 94 05
86 IN 02 A2
88 SE 04 A0
8A OF C4 A0
8C IN 04 A2
8E CO 04 A6
90 BR 8A 02
92 BR 82 07
94 CO FE A0
96 BR 9C 01
98 RE 00 00
9A BR 12 07
9C HA 00 00
A0 SE 04 A0
A2 DE 04 A2
A4 SE 02 A2
A6 PA 01 00
A8 R1 00 00
AA 01 D2 E2
AC IN 02 A2
AE CO 02 04
B0 BR AA 03
B2 PA 00 00
B4 01 D2 E2
B6 HA 00 00
```

MULTIPLE CONTACT CP-MAS

```
01 BR 06 07
02 BR 06 07
03 BR 06 07
04 BR 06 07
06 OF A0 A0
08 PA 00 00
10 SE 06 A0
12 OF A0 E4
14 OF D0 E0
16 SE 02 A0
18 OF D8 E4
1A OF D4 E6
1C IN 02 A2
1E C0 02 B0
20 BR 18 02
30 PA 01 00
32 OF D0 EA
34 IN 06 A2
36 PA 00 00
38 C0 06 B2
3A BR 16 02
70 PA 00 00
72 SE 02 A0
74 OF C4 E8
76 IN 02 A2
78 C0 02 B6
7A BR 74 02
80 SE 02 A0
82 C0 02 BA
84 BR 94 05
86 IN 02 A2
88 SE 04 A0
8A OF C4 A0
8C IN 04 A2
8E C0 04 A6
90 BR 8A 02
92 BR 82 07
94 HA 00 00
A0 SE 02 A0
A2 PA 01 00
A4 R1 00 00
A6 01 D2 E2
A8 01 D6 E0
AA IN 02 A2
AC C0 02 B4
AE BR A6 02
B0 PA 00 00
B2 01 D2 EE
B4 HA 00 00
```

DOUBLE QUANTUM MAS

```
01 BR 06 07
02 BR 06 07
03 BR 06 07
04 BR 06 07
06 PA 00 00
08 DF A0 A0
10 DF D0 EC
12 DF A0 E4
14 DF D0 E0
16 DF D4 E8
18 DF D6 E0
1A SE 02 A0
1C DF D8 E8
1E DF A0 EA
20 IN 02 A2
22 CO 02 B0
24 BR 1C 02
30 DF D0 E0
32 DF A0 E6
34 PA 01 00
36 DF D2 E2
70 PA 00 00
72 SE 02 A0
74 DF C4 EE
76 IN 02 A2
78 CO 02 B6
7A BR 74 02
80 SE 02 A0
82 CO 02 BA
84 BR 94 05
86 IN 02 A2
88 SE 04 A0
8A DF C4 A0
8C IN 04 A2
8E CO 04 A6
90 BR 8A 02
92 BR 82 07
94 HA 00 00
A0 SE 02 A0
A2 PA 01 00
A4 R1 00 00
A6 01 D2 E2
AA IN 02 A2
AC CO 02 B4
AE BR A6 02
B0 PA 00 00
B2 01 D2 E2
B4 HA 00 00
```

DOUBLE QUANTUM CP-MAS

```
01 BR 06 07
02 BR 06 07
03 BR 06 07
04 BR 06 07
06 OF A0 A0
08 PA 00 00
10 OF A0 E4
12 OF D0 E0
14 SE 02 A0
16 OF A0 EC
18 IN 02 A2
1A CO 02 B0
1C BR 16 02
1E SE 02 A0
20 OF A0 E6
22 IN 02 A2
24 CO 02 B2
26 BR 20 02
28 OF D4 EA
2A OF A0 E6
2C PA 01 00
2E OF D6 EE
70 PA 00 00
72 SE 02 A0
74 OF C4 E8
76 IN 02 A2
78 CO 02 B6
7A BR 74 02
80 SE 02 A0
82 CO 02 BA
84 BR 94 05
86 IN 02 A2
88 SE 04 A0
8A OF C4 A0
8C IN 04 A2
8E CO 04 A6
90 BR 8A 02
92 BR 82 07
94 HA 00 00
A0 SE 02 A0
A2 PA 01 00
A4 R1 00 00
A6 01 D2 E2
AA IN 02 A2
AC CO 02 B4
AE BR A6 02
B0 PA 00 00
B2 01 D2 E2
B4 HA 00 00
```

References

1. Abragam, A., The Principles of Nuclear Magnetism (Clarendon Press, Oxford, 1961).
2. Slichter, C. P., Principles of Magnetic Resonance (Springer-Verlag, New York, 1978)
3. Haeberlen, U., High Resolution NMR in Solids, Selective Averaging, Supplement I in Advances in Magnetic Resonance, edited by J. S. Waugh (Academic Press, New York, 1976).
4. Silver, B. L., Irreducible Tensor Methods (Academic Press, New York, 1976).
5. Tinkham, M., Group Theory and Quantum Mechanics (McGraw-Hill, New York, 1964).
6. Goldman, M. Spin Temperature and Nuclear Magnetic Resonance in Solids (Clarendon Press, Oxford, 1970).
7. E. O. Stejskal, J. Schaefer, and R. A. McKay, J. Magn. Reson. 25, 569 (1977).
8. A. Pines, M. G. Gibby, and J. S. Waugh, J. Chem. Phys. 59, 569 (1973).
9. E. R. Andrew, A. Bradbury, and R. G. Eades, Nature 182, 1659 (1958).
10. I. J. Lowe, Phys. Rev. Lett. 2, 285 (1959).
11. E. Lippmaa, M. Alla, and T. Tuherm, in Magnetic Resonance and Related Phenomena, Proceedings of the 19th Congress Ampere, edited by H. Brunner, K. H. Hausser, and D. Schweitzer (North-Holland, Amsterdam, 1976), p. 113.
12. M. M. Maricq and J. S. Waugh, J. Chem. Phys. 70, 3300 (1979).

13. E. T. Lippmaa, M. A. Alla, T. J. Pehk, and G. Engelhardt, J. Amer. Chem. Soc. 100, 1929 (1978).

14. U. Haeberlen, and J. S. Waugh, Phys. Rev. 175, 453 (1968).

15. L. M. Ryan, R. E. taylor, A. J. Paff, and B. C. Gerstein, J. Chem. Phys. 72, 508 (1980).

16. See D. P. Burum and W. -K. Rhim, J. Chem. Phys. 71, 944 (1979) and references therein.

17. S. Vega and A. Pines, J. Chem. Phys. 66, 5624 (1977).

18. H. Hatanaka and T. Hashi, J. Phys. Soc. Japan 39, 1139 (1975).

19. H. Hatanaka, T. Terao, and T. Hashi, J. Phys. Soc. Japan, 39, 835 (1975).

20. W. P. Aue, E. Bartholdi, and R. R. Ernst, J. Chem. Phys. 64, 2229 (1976).

21. S. Vega, T. W. Shattuck, and A. Pines, Phys. Rev. Lett. 37, 43 (1976).

22. A. Pines, S. Vega, and M. Mehring, Phys. Rev. B 18, 112 (1978).

23. Mehring, M., High Resolution NMR Spectroscopy in Solids, Vol. 11 in NMR:Basic Principles and Progress, edited by P. Diehl, E. Fluck, and R. Kosfeld (Springer-Verlag, New York, 1976).

24. For a recent calculation and references see N. Zumbulyadis, P. M. Henrichs, and R. H. Young, J. Chem. Phys. 75, 1603 (1981).

25. S. Vega, T. W. Shattuck, and A. Pines, Phys. Rev. A 22, 638 (1980).

26. Drobny, G., Ph.D. Dissertation (University of California, Berkeley, 1982).

27. E. R. Andrew, L. F. Farnell, M. Firth, T. D. Gledhill and I. Roberts, J. Magn. Res. 1, 27 (1969).

28. See V. J. Bartuska and G. E. Maciel, J. Magn. Res. 42, 312 (1981), and references therein.

29. R. Eckman, M. Alla, and A. Pines. J. Magn. Res. 41, 440 (1980).

30. D. Doskocilova and B. Schnieder, Advan. Colloid Interface Sci. 9, 63 (1978).

B. Schneider, D. Doskocilova, J. Babka, and Z. Ruzicka, J. Magn. Res. 37, 41 (1980).

31. G. Balimann, M. J. S. Burgess, R. K. Harris, A. G. Oliver, K. J. Packer, R. J. Say, S. F. Tanner, R. W. Blackwell, L. W. Brown, A. Bunn, M. E. A. Cudby, and J. W. Eldridge, Chem. Phys. 46, 469 (1980).

32. P. A. S. van Dijk, W. Schut, J. W. M. van Os, E. M. Menger, and W. S. Veeman, J. Phys. E 13, 1309 (1980).

33. F. D. Doty and P. D. Ellis, Rev. Sci. Instrum. 52, 1868 (1981).

34. V. R. Cross, R. K. Hester, and J. S. Waugh, Rev. Sci. Instrum. 47, 1486 (1976).

35. Reference Data for Radio Engineers, edited by A. G. Kandoian and L. A. DeRosa (H. W. Sams, New York, 1968).

36. J. L. Ackerman, R. Eckman, and A. Pines, Chem. Phys. 42, 423 (1979).

37. B. Berglund and R. W. Vaughan, J. Chem. Phys. 73, 2037 (1980). Mantsch, H. H., Saito, H., and Smith, I. C. P., Vol. 11 in Progress in NMR Spectroscopy, edited by J. W. Emsley, J. Freeney, and L. H. Sutcliffe (Pergamon, New York, 1977), p. 211.

38. Wemmer, D. E., Ph. D. Dissertation (University of California, Berkeley, 1978). Tang, J. -H., Ph. D. Dissertation (University of California, Berkeley, 1981).

39. J. Tang, L. Sterna, and A. Pines, J. Magn. Res. 41, 389 (1980).

40. E. Hahn, Phys. Rev. 80, 580 (1950). I. Solomon, Phys. Rev. 110, 61 (1958). J. H. Davis, K. R. Jeffrey, M. Bloom, M. I. Valic, and T. P. Higgs, Chem. Phys. Lett. 42, 390 (1976).

41. Spiess, H. W., Vol. 15 in NMR: Basic Principles and Progress, edited by P. Diehl, E. Fluck, and R. Kosfeld (Springer-Verlag, New York, 1978).

42. M. Alla, R. Eckman, E. Kundla, and A. Pines, paper presented at the 20th Rocky Mountain Conference on Analytical Chemistry, Denver, 1978.

43. J. S. Waugh, M. M. Maricq, and R. Cantor, J. Magn. Res. 29, 183 (1978).

44. S. Vega, J. Chem. Phys. 68, 5518 (1978).

45. A. Wokaun and R. R. Ernst, J. Chem. Phys. 67, 1752 (1977).

46. M. H. Levitt and R. Freeman, J. Magn. Res. 33, 473 (1979).

47. D. E. Wemmer, E. K. Wolff, and M. Mehring, J. Magn. Res. 42, 460 (1981).

48. W. T. Dixon, J. Magn. Res. 44, 220 (1981).

49. R. Eckman, M. Alla, L. Muller, and A. Pines, paper presented at the 21st Rocky Mountain Conference on Analytical Chemistry, Denver, 1979.

50. Low Field spectrum obtained by colleagues in Tallin; M. Alla, I. Heinmaa, and M. Viires, Institute of Chemical Physics and Biophysics, Estonian Academy of Sciences, Tallinn, U.S.S.R.

51. D. L. VanderHart, W. L. Earl, and A. N. Garroway, J. Magn. Res. 44, 361 (1981).

52. Andrew, E. R., Magic Angle Spinning, Vol. 1 in International Reviews in Physical Chemistry (Butterworths, 1981), p. 195.

53. A. N. Garroway, D. L. VanderHart, and W. L. Earl, Phil. Trans. R. Lond. A 299, 609 (1981).

54. M. E. Stoll and T. J. Majors, Phys. Rev. B 24, 2859 (1981).

55. M. Alla and E. Lippmaa, Chem. Phys. Lett. 87, 30 (1982).

56. R. Eckman, unpublished result.

57. A. Hohener, Cehm. Phys. Lett. 53, 97 (1978).

58. E. O. Stejskal, J. Schaefer, and J. S. Waugh, J. Magn. Res. 28, 105 (1977).

59. W. de Boer, M. Borghini, R. Morimoto, T. O. Niinikosko, and F. Udo, Phys. Letters 46A, 143 (1973). W. de Boer, Phys. Rev. B12, 828 (1975).

60. L. Muller, R. Eckman, and A. Pines, Chem. Phys. Lett. 76, 149 (1980).

61. R. G. Brewer and E. L. Hahn, Phys. Rev. A11, 1641 (1975). D. G. Gold and E. L. Hahn, Lecture Notes, Ampere Summer School IV, Pula, 1976.

62. M. Alla, R. Eckman, and A. Pines, Chem. Phys. Lett. 71, 148 (1980).

63. K. Kumitomo, J. Phys. Soc. Japan 30, 1059 (1971). P. Mansfield and G. P. Cant, Phys. Letters 33A, 130 (1970).

64. J. F. J. M. Pourquie and R. A. Wind, Phys. Letters 55A, 347 (1976).

65. L. Muller, Chem. Phys. 61, 235 (1981).

66. R. Eckman, L. Muller, and A. Pines, Chem. Phys. Lett. 74, 376 (1980).

67. D. E. Woessner and H. S. Gutowsky, J. Chem. Phys. 29, 804 (1958). H. T. Stokes, T. A. Case, and D. C. Ailion, J. Chem. Phys. 70, 3563 (1979). H. T. Stokes and D. C. Ailion, J. Chem. Phys. 70, 3572 (1979). A. Kozak, Z. Pajak, and N. Pislewski, Chem. Phys. Lett. 74, 173 (1980). A. R. Sharp and M. M. Pintar, J. Chem. Phys. 75, 2652 (1981).

68. M. Alla, R. Eckman, and A. Pines, 71, 148 (1980).

69. E. R. Andrew, A. Bradbury, R. G. Eades, and V. T. Wynn, Phys. Letters 4, 99 (1963).

70. W. Schajor, N. Pislewski, H. Zimmermann, and U. Haeberlen, Chem. Phys. Lett. 76, 409 (1980).

71. D. Suter and R. R. Ernst, Phys. Rev. B 25, 6038 (1982).

72. J. Tang, L. Sterna, and A. Pines, J. Magn. Res. 41, 389 (1980).

73. Wyckoff, P. W. G., Crystal Structures (Wiley, New York, 1969). Vol. 6 (1).

74. For a review see Andrew, E. R., Vol. 8 in Progress in NMR Spectroscopy, edited by J. W. Emsley, J. Feeney, and L. H. Sutcliffe (Pergamon, New York, 1972). P. 1.

75. G. E. Pake, J. Chem. Phys. 16, 327 (1948).

76. L. M. Ryan, R. E. Taylor, A. J. Paff, and B. C. Gerstein, J. Chem. Phys. 72, 508 (1980).

77. G. Scheler, U. Haubenreisser, and H. Rosenberger, J. Magn. Res. 44, 134 (1981).

78. R. Eckman, J. Chem. Phys. 76, 2767 (1982).

79. T. Terao, H. Mivra, and A. Saika, J. Chem. Phys 75, 1573 (1981).

80. "N.M.R. Spectra" (Sadtler Research Laboratories, Philadelphia).

81. C. J. Pouchert and J. R. Campbell, in Aldrich Library of NMR Spectra (Aldrich Chemical Co., Milwaukee, 1974).

82. Wyckoff, R. W. G., Crystal Structures (Wiley, New York, 1966). Vol. 5.

83. For a review of ring current effects see Haigh, C. W., and Mallion, R. B., Vol. 13 in Progress in NMR Spectroscopy, edited by J. W. Emsley, J. Feeney, and L. H. Sutcliffe (Pergamon, New York, 1980). p. 303.

84. S. Sagnowski, S. Aravamudhan, and U. Haeberlen, J. Chem. Phys. 66, 4697 (1977).

85. Wyckoff, R. W. G., Crystal Structures (Wiley, New York, 1971). Vol. 6 (2).

86. M. Cohen and F. Reif, Solid State Physics 5, 321 (1957).

87. E. Kundla, A. Samoson, and E. Lippmaa, Chem. Phys. Lett. 83, 229 (1981).

88. P. Taylor, J. Baugher, and H. Kriz, Chem. Rev. 75, 203 (1975).

89. E. Oldfield, S. Schramm, M. Meadows, K. Smith, R. Kinsey, and J. Ackerman, J. Amer. Chem. Soc. 104, 919 (1982).

90. D. Weitekamp and A. Pines, MMRD Annual Report (Lawrence Berkeley Laboratory, Berkeley, 1980).